FACULDADE DE ENGENHARIA DA UNIVERSIDADE DO PORTO

Anatomy Segmentation of Breast Ultrasound images

António Mesquita dos Santos Marques Carreiro

Mestrado Integrado em Engenharia Eletrotécnica e de Computadores

Supervisor: Professor Doutor Hélder Filipe Pinto de Oliveira

Co-Supervisor: João Pedro Fonseca Teixeira

September 26, 2019

Resumo

O cancro da mama é a principal causa de cancro nas mulheres em todo o mundo. Há vários fatores associados a este cancro, como por exemplo primeira gravidez tardia, menopausa tardia, consumo moderado de álcool, e genética. No entanto, como resultado da deteção mais precoce e da melhoria dos tratamentos, a taxa de mortalidade tem vindo a decrescer, em certos países. A ultrasonografia é uma técnica mais barata, acessível, e mais segura para deteção de cancro da mama, quando comparado com a mamografia, já que a paciente não é exposta a radiação ionizante. Deste modo, o uso de imagens ultrassom para o estudo, avaliação e desenvolvimento de diferentes técnicas para segmentação de estruturas anatómicas e lesões da mama na mulher desempenha um papel significativo.

Tendo isto presente, o desenvolvimento de um algoritmo para segmentação automatizada de estruturas anatómicas, como a pele, a gordura subcutânea, a glândula mamária e a região torácica, assim como lesões, será de extrema importância para empoderar as pacientes e melhorar a comunicação entre estas e o médico especialista. Deste modo, esta dissertação investiga seis técnicas diferentes para segmentação de lesões - K-means clustering, Mean shift clustering, Watershed segmentation, Region growing, Active contour model (Snakes) e Polar minimum path; e três para segmentação de estruturas anatómicas - K-means clustering, Mean shift clustering e Watershed segmentation, todas as três seguidas de um algoritmo de caminho mínimo de modo a conectar uma margem da imagem à outra.

Para avaliar os resultados estes são comparados com anotações manualmente delineadas por uma radiologista usando métricas Pixel-Area e de contorno. Os resultados indicam que os métodos baseados em contornos e os métodos baseados em regiões tendem a ter um melhor desempenho que os métodos baseados em clustering e que os métodos baseados em watershed, no que toca à segmentação de lesões. Para mais, o método Active contour model (SD = 0.72, AD = 4.3) foi aquele que melhor cumpriu a tarefa de segmentação de lesões. Por outro lado, os resultados revelam que o K-means clustering (SD = 0.57, AD = 13.4) é o método testado que leva aos melhores, no que toca à segmentação de estruturas anatómicas. Além disso, os resultados sugerem que este método excede tanto o Watershed como o Mean shift para a segmentação da pele (SD = 0.61, AD = 3.1), da glândula mamária (SD = 0.49, AD = 23.2) e da região torácica (SD = 0.71, AD = 13.1). O Watershed, no entanto, supera os outros dois métodos supracitados para segmentação da gordura subcutânea (SD = 0.51, AD = 17.2).

Abstract

Breast cancer is the leading cause of cancer in women worldwide. There are many risk factors associated with breast cancer such as late first full-term pregnancy, late menopause, moderate alcohol intake, and genetics. However, as a result of earlier detection and improved treatment, the mortality rate has decreased in some countries. Ultrasound imaging is an affordable, easily accessible and safer technique to detect breast cancer, compared to mammograms, since it does not expose the patient to ionizing radiation. Therefore, the use ultrasound imaging for study, evaluation and development of different techniques for anatomical landmark segmentation of the different structures and lesions of the female breast can play a significant role.

Bearing this in mind, the development of an algorithm for automated segmentation of anatomical structures, such as skin, subcutaneous fat, mammary gland, and thoracic region, as well as lesions of the female breast using ultrasound imaging can be of great use to empower the patients and improve the communication between them and the physician. This dissertation investigates the use of six different methods for lesion segmentation - K-means clustering, Mean shift clustering, Watershed segmentation, Region growing, Active contour model (Snakes) and Polar minimum path; and three for anatomical structures segmentation - K-means clustering, Mean shift clustering and Watershed segmentation, all of them followed by a shortest path algorithm to connect one margin to the other.

To assess the results, these are compared with manually delineated annotations by a radiologist using Pixel-Area and Contour-wise metrics. The results indicate that contour-based and region-based methods have a better performance than clustering-based and watershed-based methods for lesion segmentation. Furthermore, Active contour model (SD = 0.72, AD = 4.3) was the most successful of the methods tested for the task at hands. On the other hand, the results revealed K-means clustering (SD = 0.57, AD = 13.4) to be the most fruitful of the methods tested for anatomical structures segmentation. Additionally, the results suggest that this method exceeds both Watershed and Mean shift at skin (SD = 0.61, AD = 3.1), mammary gland (SD = 0.49, AD = 23.2) and thoracic region (SD = 0.71, AD = 13.1) segmentation. Watershed segmentation, however, outperforms the other two at subcutaneous fat (SD = 0.51, AD = 17.2) segmentation.

Acknowledgements

Throughout the five years of this course I have received a great deal of support and assistance.

I would first like to thank my supervisor, Dr. Hélder Oliveira, for giving me the opportunity to work at INESC TEC two years ago as an intern. I would also like to thank my co-supervisor, João Teixeira, for developing my critical thinking throughout these two years and teaching me how to attack engineering problems.

On top of that, I would like to thank radiologist Rute Santos from Escola Superior de Tecnologia da Saúde de Coimbra for manually delineating the ultrasound images used in this dissertation.

Next, I would like to thank my closest friends from university: Sérgio, Daniel, Paulo, Jorge, Armando, André, Joaquim, Tiago, Diogo, Manel, Martins, Grilo, Nando, Jójó, Francisco and last, but certainly not least, Ramalho to which I am very grateful to have shared moments of pain, and feelings of joy and satisfaction during our battles as partners in class.

After that, I would like to express my gratitude to my hometown friends who have been with me for many years and helped me through the hardest moment of my life. Teodoro, Simão, Fábio, Miguel, Dinis, Tiago, Nuno, Janecas, Andrade, Francisco, Ânia, Catarina, Bea. Thank you.

Following, I would like to thank 5 special people with whom I was flatmates with. Camilo Gutiérrez and Juan David Camacho, my two biggest influences throughout university. I am forever thankful for every moment we shared and for everything I learned with the two of you. El que piensa pierde is one of my favourite quotes and truly embodies your life philosophy. I would also like to thank you for arousing in me the desire to learn to dance. I would also like to show my gratitude to Raul, more than a flatmate you were my big brother in Porto. We shared incredible moments together and I would never ask for a better flatmate. Bruno, thank you for mentoring and sharing knowledge with me. I learned the fundamentals of programming with you by my side, fundamentals that today serve me greatly. You are a unique person and along with Raul, you two were my favourite flatmates. I would also like to thank my incredible friend Tabata for being kind, understanding and showing me new perspectives. You are truthfully an amazing person.

Next, I wish to thank my godmother, Tuxa, for being my mother's best friend and making her laugh everyday. I want to extend my gratitude to Tio Carlos, to Marta and João for being my borrowed cousins.

I would also like to express my sincerest gratitude to my godfather, Emídio, for always being there for me and being my second father. Thank you for making Porto feel like home to me and for being someone I look up to. I wish to extend this appreciation to my "Padrinha" Luísa who always shows an incredible amount of energy and sense of humor and to the kids, Zé and Kiko, who make me feel like an older brother.

I would also like to convey a special thank you to my family, my grandfather, Avô Américo who represents bravery to me, my late grandmother avó Odette who represents who symbolizes delicacy to me, my late grandfather Avô António who I never had the opportunity to meet but with whom I share the name and, as my mother has told me many times, the personality, my grandmother Avó Zé who is a force of nature and has always shown me what is the meaning of

a powerful woman, my uncles Tio Zé and Tio Paulo, my aunts Tia Inês and Tia Sofia and Tia Fernanda, my cousins Francisca, Patrícia, Manel, and Pedro who was a great influence in my childhood and I am forever grateful for that. An enormous thank you.

To my loving girlfriend, Alexandra, I would like to address my gratitude for keeping my spirit high during this dissertation, through all the setbacks with love and comprehension. I would also like to express my appreciation for everything we have lived so far and for what I have learned from you.

To my best friend, the only person I would die for, the person who has always led the way for me, my brother, Duarte, I am very honored to have shared my life with you, to have learned from you and with you. To see you grow as a person and mature as a professional, I am immensely proud. I have always looked up to you. Thank you for always defending me and believing in me and cheering me up.

To my late father, my biggest role model, a unique person whose intellectual can not be matched. My goal has always been to be as good as you. You were gone too soon, I think this was your way to give me a chance to match you. O arranjador, my hero, a person with an indomitable force and willpower and a thirst for knowledge whilst being an incredibly kind person. You were a visionary, always ahead of time. A humongous thank you.

Finally, to the person I dedicate this dissertation, the most important person in my life, my mother. I have no words to describe my feelings for you. I love you with all my heart. You always took care of me to the best of your possibilities, you showed me that hard work prevails over talent and luck. And when our family needed it the most, you revealed a colossal strength inside you that was unknown. You are my favourite person. I say it again, I love you!

António Mesquita dos Santos Marques Carreiro

This work was funded by the ERDF - European Regional Development Fund through the Norte Portugal Regional Operational Programme (NORTE 2020), under the PORTUGAL 2020 Partnership Agreement and through the Portuguese National Innovation Agency (ANI) as a part of project BCCT.Plan–NORTE-01-0247-FEDER-01768 .

"Só se aprende a caminhar caminhando."

Pai

Contents

List of Figures

List of Tables

Abbreviations and Symbols

AD	Average Distance
AMED	Average MinimumEuclidean Distance
AOM	Area Overlap Measure
CHT	Circular Hough Transform
CM	Combined Measure
GT	Ground Truth
H-max	H-maxima Transform
H-min	H-minima Transform
HAUSD	Hausdorff distance
INESC TEC	Instituto de Engenharia de Sistemas e Computadores, Tecnologia e Ciência
SD	Sørensen–Dice coefficient
SHT	Standard Hough Transform
STD	Standard Deviation
VCMI	Visual Computing and Machine Intelligence

Chapter 1

Introduction

1.1 Context

Breast cancer is the leading cause of cancer in women worldwide. According to the World Health Organization, more than 600,000 women died from this type of cancer in 2018 alone and the frequency of detection is increasing globally [68]. This cancer is caused by the malignant proliferation of epithelial cells lining the ducts or lobules of the breasts. There are many risk factors associated with breast cancer such as late first full-term pregnancy, late menopause, moderate alcohol intake, and genetics. However, as a result of earlier detection and improved treatment, the mortality rate has decreased in some countries [40].

One metric for breast cancer diagnosis is the 5-year survival rate. This metric tells us the percentage of people that are still alive 5 years after being diagnosed with cancer. If the cancer is only in the breast then there is a 99% 5-year survival rate. 62% of the diagnostics show the cancer at this stage. However, if it has spread to the regional lymph nodes then this number decreases to 85%. Furthermore, if the cancer has spread to a more distant part of the body then the survival rate is 27% [10]. For this reason, early diagnosis increases the chance of survival and of a successful treatment.

Ultrasound, contrary to mammograms, can be very useful when trying to distinguish between fluid-filled cysts, which are benign, and solid masses, which can constitute cancer. This imaging technique is not only affordable but also more easily accessible and safer since it does not expose the patient to radiation [3].

Accordingly it is of utmost importance to use ultrasound imaging for study, evaluation and development of different techniques for anatomical landmark segmentation of the different structures of the female breast such as skin, fat, glandular tissue and thoracic region but also lesions in those tissues.

1.2 Motivation

Even though the detection of cancer has been largely studied, the decision of which strategy to take concerning oncoplastic surgery still relies almost exclusively on the surgeon's perception of post surgical aesthetic result, which sometimes leads to unsatisfactory outcomes.

In order to empower the patients on the joint decision process there needs to exist a better communication between the parts. This can be achieved by developing medical grade 3D models of the breast and better explaining the surgical options and their results.

So as to obtain such models, some effort has been made concerning multi-modality radiologic imaging combination. This line of research is yet to mature. In turn, the modality alignment requires accurate landmarks to be produced. 2D Ultrasound imaging has not been sufficiently studied for multimodal registration due to the image characteristics and thus, landmark segmentation is extremely important.

1.3 Goals

This dissertation aims at developing an algorithm for automated segmentation of the several anatomical structures as well as lesions of the female breast using ultrasound imaging.
The task can be subdivided in three major tasks:

1. Study and evaluation of the existing techniques for segmentation of anatomical structures such skin, fat and glandular tissue and of lesions

2. Development of ultrasound segmentation methods for acquiring landmarks

3. Evaluation of the developed methods with manual annotations and comparison of results with the current algorithm alternatives

1.4 Contributions

This dissertation presents the following contributions:

- An experimental methodology for lesion segmentation in ultrasound images;

- An experimental methodology for anatomical structures segmentation, more specifically skin, subcutaneous fat, mammary gland and thoracic region in ultrasound images;

- A model for lesion segmentation after previous detection, in ultrasound images;

- A model for skin, subcutaneous fat, mammary gland and thoracic region detection and segmentation, in ultrasound images;

1.5 Structure

Apart from Chapter 1 there are 3 other chapters in this dissertation:

- Chapter 2 shows the medical background of this dissertation as well as the technical state of the art and related work. This chapter gives the reader an overview of the current techniques for pre-processing and segmentation of breast ultrasound images;
- Chapter 3 details the different pipelines used for segmentation of both anatomical structures and lesions. This chapter also details the results and the reasoning behind them;
- Chapter 4 summarizes the dissertation and offers possible future additions to further develop the work presented

Chapter 2

Literature review

In this chapter the reader is enlightened about the structures that constitute the breast. After that a brief overview over the acquisition process is done showing how the ultrasound works and how each structure appears in a B-mode ultrasound image. A literature review over the recent past work on pre-processing and segmentation is also done.

2.1 Breast Anatomy

The breasts are organs located on the anterior chest wall. The female breast is more developed than the male breast since its development is stimulated by the estrogens production during the monthly female sexual cycle. The combination with the growth of the female's mammary glands and the deposition of fat gives the breasts mass [31].

This section makes a brief review of the anatomy of several breast structures [27].

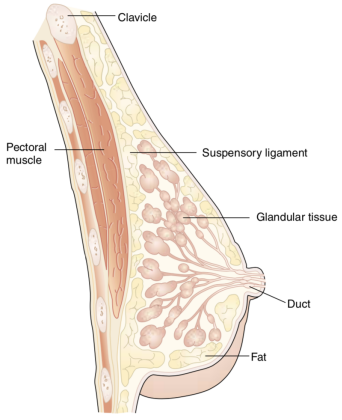

Figure 2.1: The anatomy of a breast

The constituting parts of the breast beneath the skin are the glandular tissue, fibrous tissue which connects its lobes and fat tissue in the intervals between the lobes. The fat tissue usually exists in considerable abundance, and determines the form and size of the gland. Beneath this

structures is the Pectoralis major which is a "thick, fan-shaped muscle, situated at the upper and forepart of the chest" [26]. Figure 2.1 shows a breast and its main structures.

2.2 Image Acquisition

As stated in [62], ultrasound imaging is an affordable, non-invasive technology that has been used in clinical practice for several decades. Moreover, it is obtained in real time making it the method of choice frequently. Ultrasonic waves are generated and detected by a piezoelectric crystal which deforms under the influence of an electric field and vice versa. This crystal is embedded in a transducer that serves both as a transmitter and as a detector. There are 3 ways of acquiring data: A-mode, M-mode and B-mode. This dissertation refers only to B-mode.

B-mode generates 2D images by translating acquisitions and B stands for brightness. This is illustrated in Figure 2.2a. This technique highlights strongly reflecting structures while suppressing the weakly reflecting ones. See Figure 2.2b.

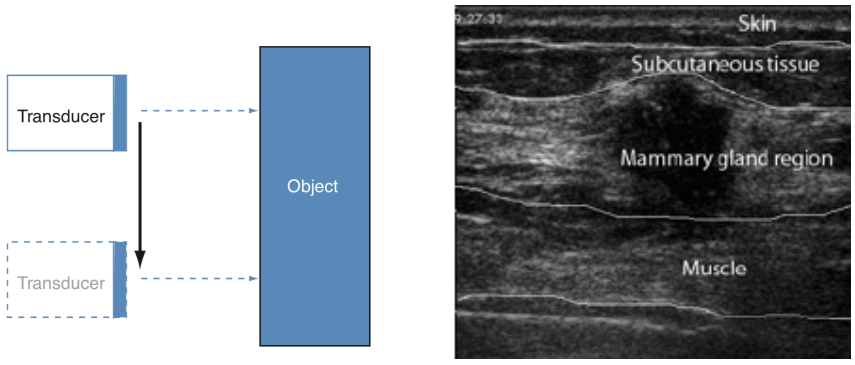

(a) B-mode image acquisition can be done by translating the transducer [62].

(b) B-mode Ultrasound image of a breast structure from [28].

Figure 2.2: B-mode Ultrasound acquisition and an example of such image

The echo pattern can be subdivided into 5 categories, according to [46]:

- **Anechoic** - Without internal echoes
- **Hyperechoic** - Increased echogenicity relative to fat or equal to fibroglandular tissue
- **Complex** - Complex mass contains both anechoic (cystic) and echogenic (solid) components
- **Hypoechoic** - Defined relative to fat; hypoechoic masses are characterized by low-level echoes throughout
- **Isoechoic** - Same echogenicity as fat.

Therefore, both skin and mammary gland will appear as **Hyperechoic** structures whilst subcutaneous tissue and pectoral muscle will be more **Hypoechoic**. Furthermore, fluid within cysts are

generally **Anechoic** and appear black and solid masses are more echogenic (or **Hyperechoic**) than fat. For this reason, ultrasonography is specially useful for distinguishing between benign (cysts) and malign (masses) lesions.

2.3 Pre-processing

A serious concern for processing medical images is the presence of speckle noise. Speckle is a random granular texture, that makes the anatomy in ultrasound images unclear and harder to see. This unwanted property of the images is caused by interference of the ultrasound echoes by reflectors spaced closer together than the machine's resolution limits as explained in [63]. This problem could be reduced using higher frequencies, although it would limit the depth of the ultrasound image. Random noise can not be predicted and for this reason it is the hardest type of noise to get rid of.

The speckle reduction in ultrasound images is a challenging task although much work has been done over the last years to overcome this obstacle.

A number of de-noising methods for medical ultrasound images have been proposed and can be divided into 5 categories: **Adaptive Filters**, **Anisotropic Diffusion Filters**, **Non-local means Filters**, **Multi-scale Filters** and **Hybrid Filters** which are combinations of the other 4 types of filters. Below is the description of each one of them along with some important papers about the subject.

Adaptive Filters have low complexity and are the simplest type of speckle noise removal filters. Median filters run through each image pixel and replace it with the median of the neighbouring pixels [35]. Bilateral filtering first proposed by [64] and more recently [6] smoothes images by combining the intensity level of nearby image values with a weighted average depending on both geometric closeness and photometric similarity in what is called speckle reducing bilateral filter (SRBF).

An efficient technique for speckle noise removal is **Anisotropic Diffusion** (SRAD). This method was originally proposed by [51] to simultaneously remove noise and preserve edges by choosing the conduction coefficient as a function. The maxim of this method is to smooth within the region instead of smoothing across the edges.

A general expression for Anisotropic Diffusion is detailed in [63]. The derivations and equations below are cited and summarized from there:

$$I(x,0) = I_0 \qquad \frac{\partial I}{\partial t} = div(F) + \beta(I_0 - I) \tag{2.1}$$

where I is the input image, I_0 the initial image, F the diffusion flux and β is a data attachment coefficient.
If $\beta = 0$, then the non linear probability density function with $F = c(|\Delta I|) \times I$ is given by:

$$C(x) = \frac{1}{1+\frac{x}{k}} \text{ and } C(x) = exp(\frac{1}{1+\frac{x}{k}}) \tag{2.2}$$

and the functions for the diffusion coefficient:

$$C(\| \nabla I \|) = e^{-}(\frac{\| \nabla I \|}{K})^2 \text{ and } C(\| \nabla I \|) = \frac{1}{1+(\frac{\|\nabla I\|}{K})^2} \tag{2.3}$$

Δ is the gradient operator, *div* is the divergence operator and $\|$ denotes the magnitude.

Below is Figure 2.3 depicting the Anisotropic Diffusion method.

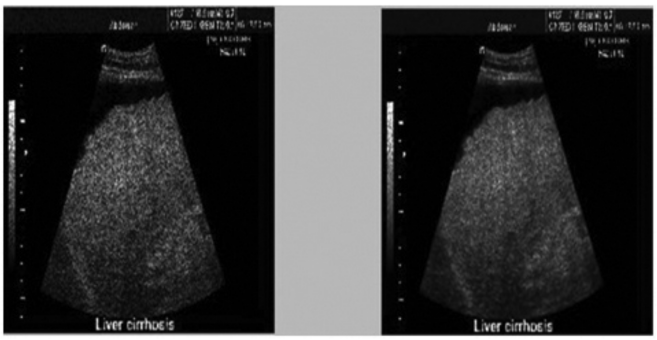

Figure 2.3: Anisotropic Diffusion Applied to Image - [51].

This method has been used by [9] in an attempt to segment the breast's mammary gland. However, several variants of this algorithm have been made since then with significant improvements.

In 2012, [11] proposed an edge-preserving speckle removal method based on interference speckle filtering followed by anisotropic diffusion.

The filter was named ISFAD and its goal is to minimize oscillations in the values of noise and preserve the local intensity information. The first part of proposed filter, *interference-based speckle filter (ISF)*, takes into account what causes the speckle noise and preserves the high intensity pixels which represent constructive interference while suppressing low intensity pixels which constitute destructive interference. This process can be divided into three steps:

First, a median filter is applied in order to smooth the image using a circular window to avoid "blocking" artifacts which could sprout from the use of a square window.

After this, the next step is to suppress the gray values caused by destructive interferences by selecting the maximum value between the median filtered image from the previous step and the speckled image.

Lastly, a small-windowed median filter is applied to eliminate the remaining extreme single pixels from the resulting image of step 2. In the end of this 3 steps, Anisotropic Diffusion is applied. Figure 2.4 represents the result of both ISF and ISFAD. The author presents an accuracy greater than 90% for structures with well-defined borders. This demonstrates the ability to segment structures and so reduce the depedence of the segmentation algorithms on their parameter set.

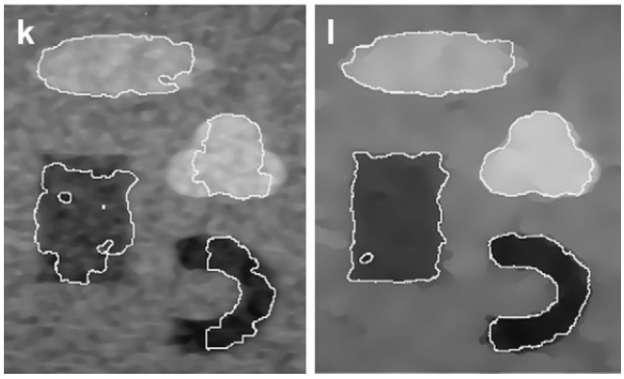

Figure 2.4: (k) interference based speckle filter and (l) interference based speckle filter followed by anisotropic diffusion - [11].

This method is cited by several other papers including [23] which takes into consideration the fact that different tissues, and more specifically breast tissues, have distinct textures. Hence, the authors propose an anisotropic diffusion guided by Log–Gabor filters (ADLG) where the conduction coefficient of the anisotropic diffusion filter is computed using texture responses instead of the intensity values. The paper claims that the selection of the K parameter is critical and should be chosen according to both noise and local contrast using Log-Gabor filters.

The results for this approach are compared with 4 other methods including ISFAD and SRAD using 2 validity metrics: Pratt's figure of merit and mean radial distance. The indices should tend toward 1 and 0, respectively, to indicate adequate edge preservation. ADLG shows the best performance indicating in the first metric a median value of 0.83 (ISFAD scores 0.59 and SRAD 0.39) and 4.19 in the second (ISFAD scores 5.88 and SRAD 6.39). The visual results for all the 5 approaches can be seen in Figure 2.5.

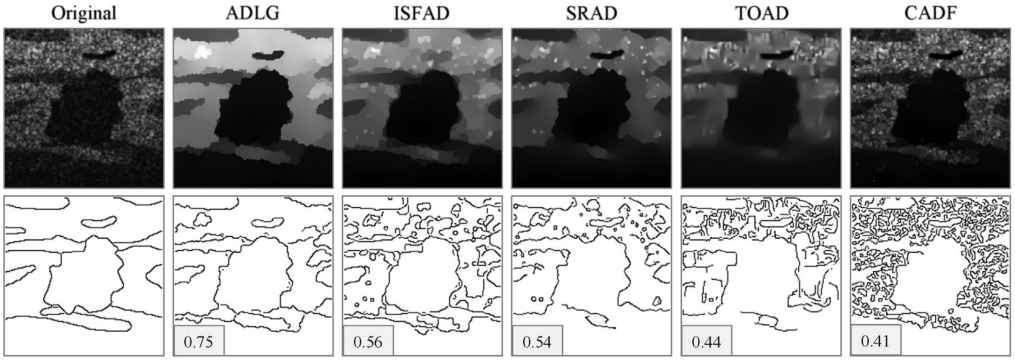

Figure 2.5: Simulated breast ultrasound image filtered by anisotropic diffusion-based approaches. Top row: Outputs of evaluated filters. Bottom row: Edge maps obtained with Canny's detector. The squares contain the corresponding figure of merit results. ADLG 5 anisotropic diffusion guided by Log–Gabor filters; CADF 5 conventional anisotropic diffusion filtering; SRAD 5 speckle-reducing anisotropic diffusion; TOAD 5 texture-oriented anisotropic diffusion; ISFAD 5 interference-based speckle filtering followed by anisotropic diffusion - [23].

Another approach to speckle noise reduction are the **Non-local Means Filters**. This type of filters are characterized by having a good performance in speckle reduction despite the fact that present high algorithm complexity.

One algorithm of this type is the Optimized Bayesian Non Local Means filter (OBNLM) [16]. This algorithm uses a Bayesian framework to adapt the Non Local (NL) Means filter for Ultrasound images by introducing the Pearson distance as a relevant measure for patch comparison. Results for approach can be seen in Figure 2.6a.

Another author [30] proposes a modified NL-means filter (MNL) using maximum likelihood estimation as the first step. This algorithm states that because NL-means algorithm is normalized for Gaussian noise reduction then it does not properly remove the Rayleigh distributed speckle present in the ultrasonic images.

The two steps of the MNL method are then the computation of the maximum likelihood estimation to obtain the initial noise-free intensity and then use a NL-means algorithm to restore the details. Figure 2.6b depicts this algorithm.

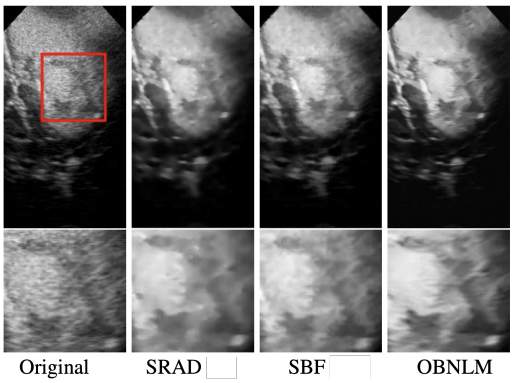

(a) Results obtained with OBNLM, SRAD and another filter SBF - [16]

(b) Comparison of MNL filter with original image and NL filter - [30].

Figure 2.6: Examples of Nonlocal Means Filters

The fourth category of de-noising methods for medical ultrasound images are the **Multi-scale Filters** which are obtained by applying a single scale method on sub-images obtained with the Laplacian pyramid [2] or wavelet decomposition [1]. [4] suggests a linear Gaussian filtering applied to sub-images obtained from a wavelet decomposition of the vertical and diagonal details.

More recently, [72] advances a speckle reduction of ultrasound images based on the wavelet shrinkage algorithm and guided filtering and can be divided into 3 steps.

The first step consists on an improved wavelet function based on the universal threshold value function in order to guarantee a balance between speckle suppresion and feature preservation.

The second step makes use of statistical models of speckle noise and noise-free signal in the wavelet domain in order to obtain a new shrinkage algorithm from a Bayesian maximum a posteriori estimation.

The third step uses a guided filter to suppress the speckle noise in the low frequency sub-band. Figure 2.7 exemplifies the result of this method.

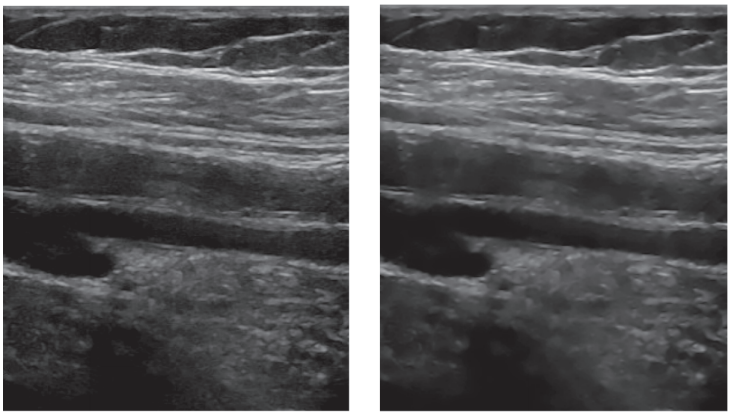

Figure 2.7: De-noised arterial image of the method proposed in [72] (the left is the original image and the right is the de-noised image).

As stated before methods from different categories can be combined to create what can be called **Hybrid Filters**.

One example of this is a recent paper [59] that suggests a hybrid algorithm consisting of three stages: in the first stage, local statistics in the form of guided filter is used. Then, in the second stage, the speckle noise is further reduce with an improved SRBF filter.

Finally, in the third stage, diffused edges are reconstructed using a joint post-processing technique that takes advantage of both bilateral and NLM filters for a more efficient attenuation of speckle noise. Figure 2.8 illustrates this algorithm.

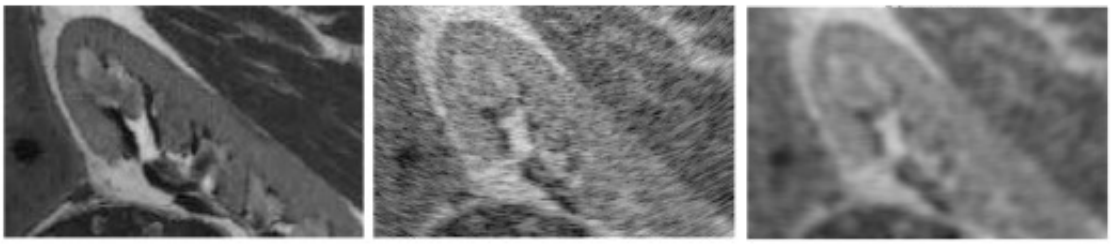

Figure 2.8: Hybrid algorithm combining guided filter with SRBF filter and a post-processing technique that takes advantage of both bilateral and NLM filters by [59]

Below is Table 2.1 summarizing the different speckle reduction filters described in this section.

Table 2.1: Summary of de-noising filtering techniques

Method	References	Advantages	Disadvantages
Adaptive Filters	[35] [64] [6]	Low complexity	Non-satisfatory de-noised results
Anisotropic Diffusion Filters	[51] [63] [9] [11] [23]	Good speckle noise suppression	Might result in an over-smooth image
Nonlocal means Filters	[16] [30]	Good speckle noise removing effect	Very high algorithm complexity
Multi-scale Filters	[2] [1] [4] [72]	time-frequency analysis and multi-scale analysis	Computationaly intensive
Hybrid Filters	[59]	Higher performance and accuracy	Depends on the combination of several techniques

2.4 Segmentation

Segmentation, in computer vision, is the process of separating an image into several segments. Over the past 20 years, numerous techniques have been proposed for ultrasound segmentation. These techniques can be essentially subdivided into 7 categories: **Histogram based** methods, **Region growing based** methods, **Model based** methods, **Watershed based** methods, **Neural network based** methods, **Clustering based** methods and **Hybrid** methods.

The first type of segmentation techniques are the **Histogram based** ones. One disadvantage of Histogram based segmentation is that it can not be directly used to segment multimodal images.

A famous algorithm that belongs to this category is the Otsu's method for image thresholding which separates the image into 2 classes (foreground and background) by calculating the optimum threshold value that minimizes the intra-class variance and maximizes the inter-class variance [50]. The use of this method along with an homomorphic filter has also been used by [18] to segment ultrasound images as seen in Figure 2.9.

There are other algorithms worth mentioning such as [34] in which a median filter is applied to the image and then this image is multiplied with a Gaussian constraint function. After that, the method uses gray level thresholding to obtain the probable margins of the lesion on which a utility function is be applied and maximized.

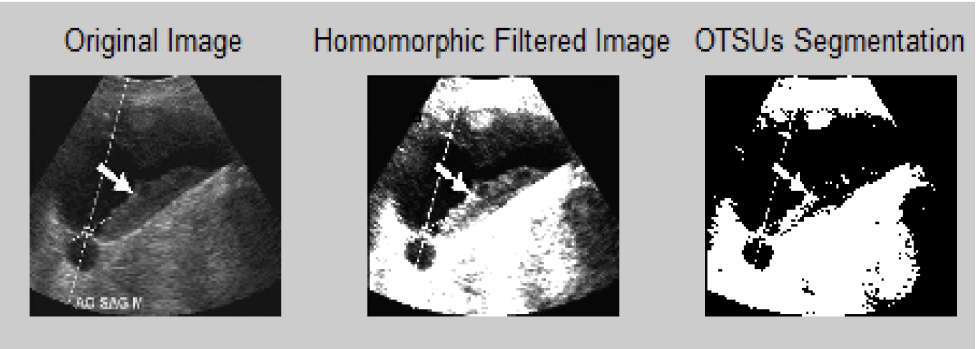

Figure 2.9: Homomorphic filtering and Otsu segmentation of ultrasound cardiac duplex screening samples [18].

Another category of methods used for ultrasound segmentation are the **Region Growing based** methods. The main goal of this type of technique is to partition an image into several regions based on the similarity of pixel intensity values. This approach has been used for segmentation by different authors but because of its sensivity to noise, it can not guarantee an accurate boundary.

One author [45] suggests filtering and enhancing the contrast of the ultrasound image to emphasize tumor regions. He then uses a mathematical formulation of a set of empirical rules used by radiologists that is often called the *Stavros Criteria* to automatically find a seed point which lies in the expected lesion region. This seed point is then expanded to find an initial boundary lesion region. This process stops as boundary points are found on the directional gradient of the image.

The process is presented in Figure 2.10a.

Authors of [52] take a different approach where the seed point is automatically selected from the abnormal region based on textural features such as co-occurrence features and run length features. This method controls the region growing process as well by similarly calculating a threshold value as depicted in Figure 2.10b.

A third author [55] suggests another alternative for segmenting ultrasound images in which the input image is initially pre-processed using a SRAD filter and then iteratively binarised to automatically find a seed point. A mathematical formulation formulation is used to select the containing region of the target seed if the number of dark regions present in the binary image is greater than one. Results for this method are illustrated in Figure 2.10c.

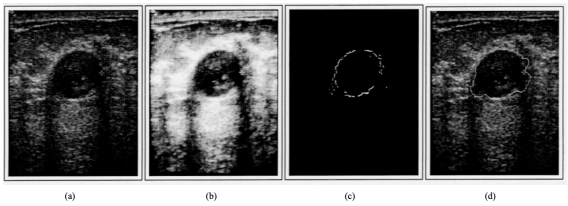

(a) [45] - (a) Original image. (b) Contrast-enhanced version. (c) Detected boundary points. (d) Output of deformable model.

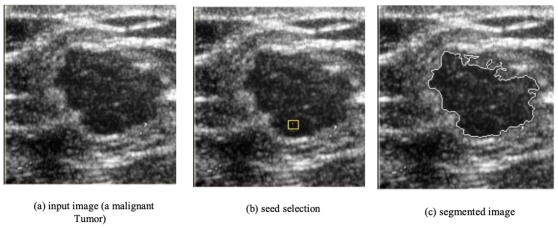

(b) Various stages of [52] algorithm for liver tumor image

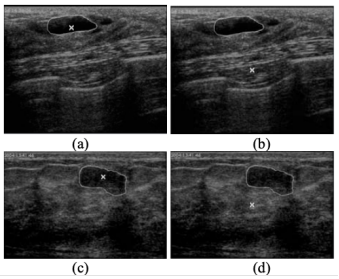

(c) Results of two cases: (a) and (c) are [56]'s method results and (b) and (d) are Madabhushi's method results

Figure 2.10: Examples of Region Growing segmentation methods

In **Model based segmentation**, a model is created and repeatedly applied to obtain a certain result. There are 3 commonly used methods for this type of segmentation: active contours, level sets and Markov random fields.

Active contour models were first proposed by [42] suggest a so called *snake* which is a deformable spline influenced by constraint and image push and pull forces to segment the desired regions whilst minimizing the energy of the contour. This method is particularly useful in noisy images.

A decade later, [71] proposed an improvement to the method presented above to solve the problems associated with initialization and poor convergence to boundary concavities by suggesting a new external force called gradient vector flow (GVF), and is computed as a diffusion of the gradient vectors of a gray-level or binary edge map derived from the image.

One example of usage is the case of researchers [41] which used the active contour model to segment tumors in Breast ultrasound images (BUS) as seen in Figure 2.11a and differentiated benign and malignant masses afterwards and [53] who applied active contours in integration with a direction score also to segment BUS images.

Level-set methods (LSM) are another framework that uses level sets for analysis of surfaces and shapes.

A group of researchers [54] designed a partial differential equation based geometric model (flow) that takes the classic Rayleigh probability distribution to model the gray levels present in ultrasound images and takes it into account to derive the flow while also taking into account the smoothness constraints. A level set formulation is then derived and the minimum value of the model is the point of minimum energy which is then used to segment the image as depicted in Figure 2.11b.

In [38] a level set based method is applied to find the final shape of the tumor after pre-processing the input image with an average and a low-pass filter. Level set methods have the downside of requiring correct initialisation and accurate tuning of the deformation parameter. These methods are also slow to achieve the local minima.

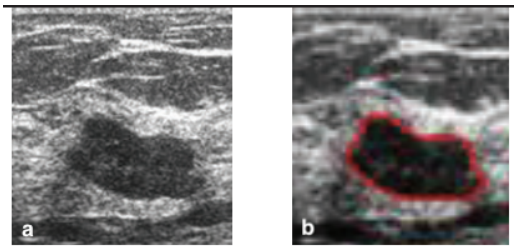

(a) (a) Original ROI and (b) Balloon Snake - [41]

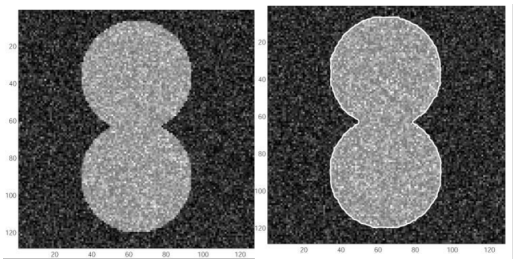

(b) Maximum likelihood algorithm applied to a synthetic image effected by Rayleigh noise - [54].

Figure 2.11: Examples of Level set segmentation methods

We also have the Markov Random Field (MRF). This technique uses a Bayesian labelling to segment images. The model takes the spatial relationship between labels to model the intensity inhomogeneity.

A famous scientific work about this was written by [43]. This paper presents a systematic way to MRF modelling summarized in 5 steps.

To start, the problem is reformulated as a labeling problem in which each label configuration represents a solution. The problem is then, again, reformulated as a Bayesian labeling problem in which the optimal solution is defined as the MAP (maximum *a posteriori*) label configurations. After that a Gibbs distribution is used to characterize the prior distribution. The fourth step is to calculate the likelihood density of the data and, as the last step, use the Bayesian rule to derive the posterior distribution of label configurations.

A paper [8] suggests the use of an adaptive region segmentation algorithm for noisy images within a Bayesian framework and uses a MRF to model the region process due to its restriction to

local interaction.

Furthermore, [69] uses a probability model-based method in breast ultrasound images. Using the combination of spatial knowledge with frequency domain constraints under a MAP with MRF (MAP-MRF) segmentation frameworks. This method is illustrated in Figure 2.12.

Figure 2.12: (a) the original image; (b) the tumor region (white area) manually segmented by the radiologist; (c) the tumor region produced by [69].

In **Watershed segmentation**, the image operates like a topographic map in which the intensity level of each pixel represents its height and where valleys or basins represent adjacent regions separated by dams. The biggest drawback of this technique is over-segmentation.

To solve this issue [37] proposed a marker controlled watershed segmentation in which markers are pre-defined and positioned within the most wanted areas to be segmented using image textures to select the markers.

Author [25] took another approach by multiplying the image by a constraint Gaussian function to calculate the markers.

An alternative way to handle over-segmenation is called *cell competition* in which basins generated by two passes of watershed transformation are merged and split into prominent segments. A cell based grouping process is then used to find the best closed subsets of edges using prominent component tessellation. Authors of [14] use this approach.

Examples of Watershed segmentation are illustrated in Figure 2.13.

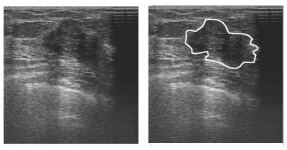

(a) [37] - On the left the original ROI and on the right the generated boundaries.

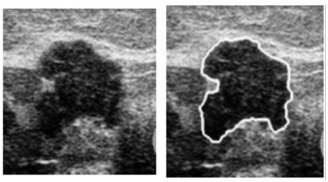

(b) [25] - On the left the original ROI and on the right the generated boundaries.

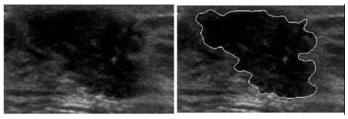

(c) [14] - On the left the original ROI and on the right the generated boundaries.

Figure 2.13: Examples of Watershed segmentation methods

Neural network based segmentation methods turn segmentation into a decision problem based on a set of features, resembling a human brain, and can be used in a supervised or unsupervised way.

A type of unsupervised neural network is called Hopfield in which the image segmentation problem is theoretically formulated as a clustering problem based on global distribution of gray level values as stated by [15].

Another type of neural network is called MultiLayer Perceptron (MLP) where one or more layers are hidden and have the fuction of artibtrating between the input and output of the neural network [36]. Figure 2.14 shows the structural graph of multilayer perceptron (MLP) neural network model.

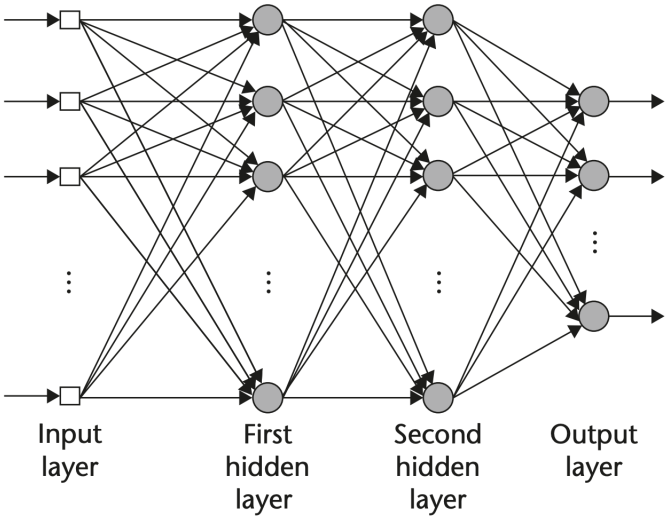

Figure 2.14: Structural graph of multilayer perceptron (MLP) neural network model [36].

One more type of unsupervised technique for neural networks are the Self Organizing Maps (SOM). According to [47] in a SOM network only the input is supplied. The solution output is the convergence of the algorithm adaptation to parameters for a given data set. This process is illustrated in the sequence of images of Figure 2.15.

Pulse Coupled Neural Network (PCNN) are yet another type of neural networks with fixed structure that are learning free and invariant to geometric transformations. They have one to one association between image pixels and network neurons. The image is analyzed by looking multiple times at different coupled pixels as stated by [33]. Performance of this type of neural networks are heavily dependent on the tuning of its parameters. One author, [17] suggests automatic parameters determination based on the analysis of neuron firing time.

By grouping a set of pixels in a way that objects in the same group are more similar to each other than those in other groups we perform a process called clustering. **Clustering based** approaches are known to achieve good results in images which contain well separable objects.

According to [61] clustering can be separated into 2 categories: hard clustering and soft clustering. The former means that a point either fully belongs to a cluster or not and the latter attributes

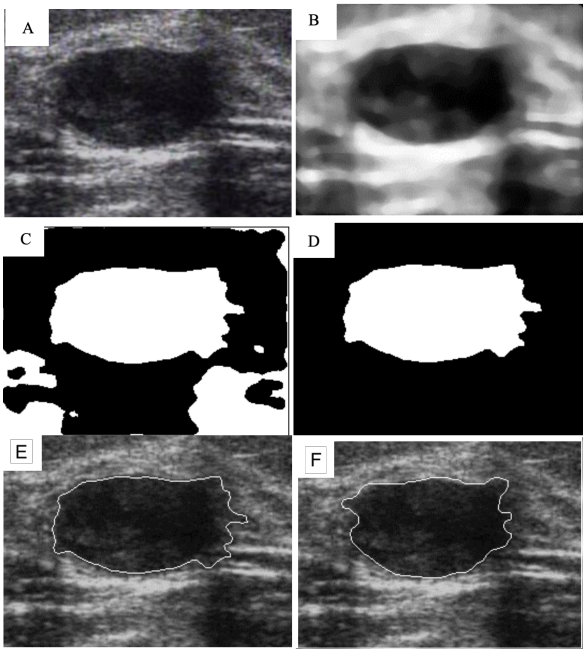

Figure 2.15: (A) Original BUS image (B) Pre-processed image (C) Segmented image (D) Removal the adjacent regions of the segmented image (E) Overlap of contour in the original image (F) Contour delimited by a radiologist - [47].

a probability for a point to be in one of the assigned clusters. Because of the presence of artifacts, hard clustering is not suitable for ultrasound images. Soft clustering can also be called fuzzy clustering.

A widely known algorithm of this type is Fuzzy C-means Clustering (FCM) which was first developed by [21] and later improved by [7] and has been used in different forms by different authors on breast ultrasound images. This algorithm can be subdivided into a few steps: first we start by selecting an initial fuzzy pseudo-partition and then repeat the process until the the algorithm converges and the centroid of each fuzzy partition does not change.

An extension of this method has proposed by [32] in which the concept of information gain has been added. To reduce FCM's sensitivity to noise fuzzy membership values and cluster centroids are updated based on information gain producing a more homogeneous clustering.

In recent years a new wave of thought called Neutrosophic Logic (NLP) has been introduced. Neutrosophic relates to a general form of logic where each proposition has separate values for truth, falsehood, and indeterminacy deals with how one affects another in decision making.

In [58] a method called neutrosophic L-mean (NLM) clustering is presented, which combines neutrosophy with FCM and can be seen in Figure 2.16a.

Another clustering method known as Neutrosophic C-means clustering (NCM) has been put forward by [29] and also integrates both NLP and FCM to better deal with uncertainty in image segmentation. This algorithm's results are illustrated in Figure 2.16b.

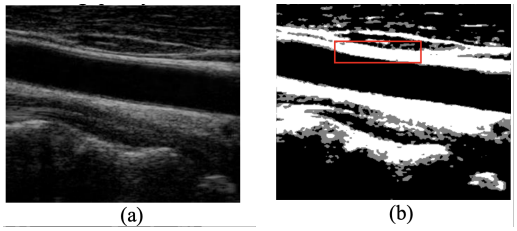

(a) [32] - On the left the original ROI and on the right the generated boundaries.

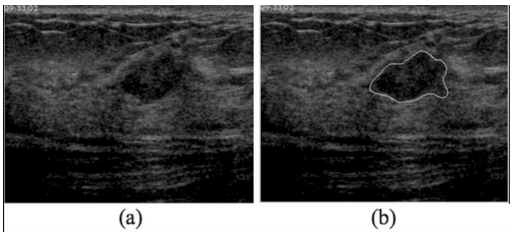

(b) [58] - On the left the original ROI and on the right the generated boundaries.

Figure 2.16: Examples of Clustering segmentation methods

Sometimes, individual approaches don't give the expected results. Therefore, some researchers opt for combining methods, with what are called **Hybrid methods**, to obtain a better way to segment the image.

One example of this is [57] in which the authors propose a technique that combines mulitple-domian features, more specifically, intensity and texture with an artificial neural network (ANN) to detect the lesion after automatically locating the region of interest (ROI). This algorithm's results can be seen in Figure 2.17a.

Another example is that of [70] who defines a cost function in terms of tumor's boundary and region information in both frequency and space domains. The authors suggest a new edge vector invariant to contrast and brightness to build the frequency constraint. The spatial domain is then constrained by modeling the tumor's pose position and intensity distribution. This method's results are illustrated in Figure 2.17b.

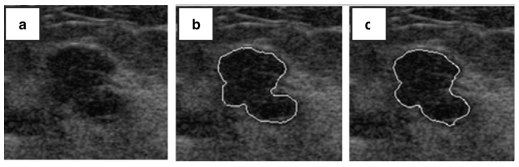

(a) [57] - (a)–(b) the original images with tumor regions manually delineated by the radiologist; (c)–(d) the tumor regions produced by the proposed method.

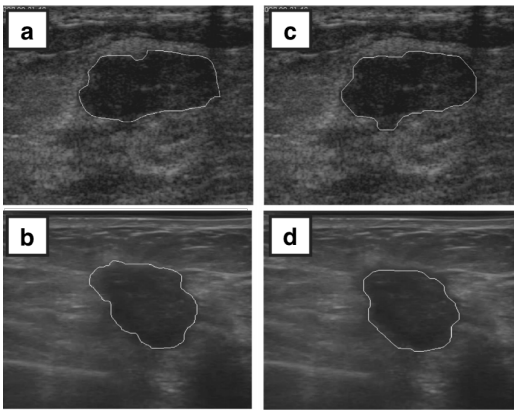

(b) [70] - (a) is the original ROI; (b) is the automatic segmentation result; (c) is the manually segmented result.

Figure 2.17: Examples of Hybrid segmentation methods

Finally, the **Shortest path algorithms** define a closed contour enclosing a previously detected seed.

Usually the closed contour computation is addressed by transforming the image into polar coordinates, where the closed contour is transformed in an open contour between two opposite margins [73].

However, some authors [12][49][13] have proposed a way to compute the closed contour in the original coordinates by addressing the main difficulty in operating in the original coordinates. After defining a directed acyclic graph, and since small paths collapsing in the seed point are naturally favored, these authors modulate the cost of the edges to counterbalance that bias.

Results from both approaches are illustrated below in Figure 2.18.

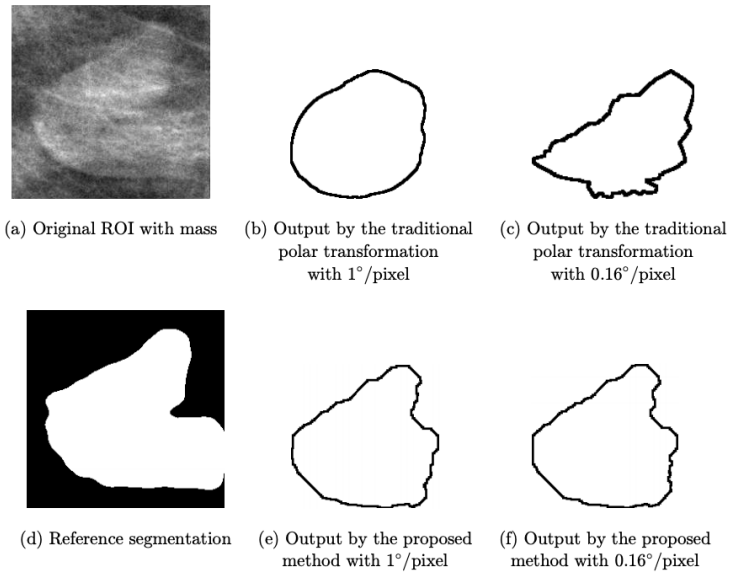

(a) Original ROI with mass

(b) Output by the traditional polar transformation with 1°/pixel

(c) Output by the traditional polar transformation with 0.16°/pixel

(d) Reference segmentation

(e) Output by the proposed method with 1°/pixel

(f) Output by the proposed method with 0.16°/pixel

Figure 2.18: Traditional vs proposed closed shortest path algorithm in [13] with different angular resolution

Below is Table 2.2 summarizing the different segmentation techniques laid out in this section.

Table 2.2: Summary of Breast ultrasound image segmentation techniques

Method	References	Advantages	Disadvantages
Histogram based	[50] [34] [18]	Easy to implement	Bad performance in multimodal histograms
Region Growing based	[45] [52] [56]	Easy to implement. Variety of stop criteria can be selected.	Susceptible to noise Starting point required
Model based	[42] [71] [41] [53] [54] [38] [43] [8] [69]	Self adapting approach.	Easy stalling in local minima states. Complex and time consuming.
Watershed based	[37] [25] [14]	Guarantees closed boundaries.	Over-segmentation.
Neural Network based	[15] [36] [47] [33] [17]	Different characteristics can be associated.	Outcome depends on training data set's features.
Clustering based	[21] [7] [32] [58] [29]	Relatively simple. Advisable for well separable clusters.	Outcome depends on initialisation. Susceptible to noise
Hybrid methods	[57] [70]	More robust due to use of spatial and frequency domain features.	Integration of multiple features.
Closed Shortest Path methods	[73] [12] [49] [13]	Reliable results.	Computational cost.

2.5 Feature extraction

The **Standard Hough Transform** as it is universally used today was invented by [20] and uses the parametric representation of a line:

$$rho = x * cos(theta) + y * sin(theta)$$

In this formulation *rho* is the distance from the origin to the line along a vector perpendicular to the line and *theta* the angle, in degrees clockwise with range $-90° \leqslant \theta \leqslant 90°$, of the perpendicular projection from the origin to the line, as illustrated in Figure 2.19. Peak values in the SHT represent potential lines in the input image.

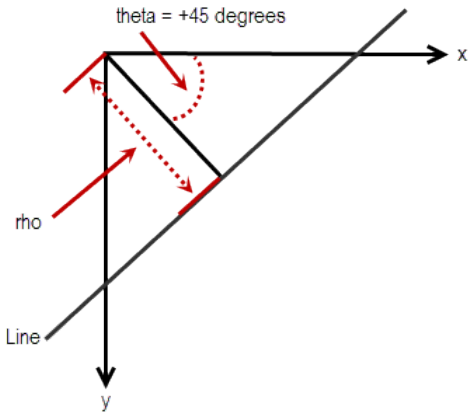

Figure 2.19: Standard Hough Transform (SHT) parametric representation

The **Circular Hough Transform** has three essencial steps:

1. **Accumulator Array Computation** - Candidate foreground pixels of high gradient vote in pattern around them to form a full circle with fixed radius and cast those votes in the accumulator array. Figure 2.20a shows an example of a candidate pixel lying on an actual circle (solid circle) and the classical CHT voting pattern (dashed circles) for the candidate pixel.

2. **Center Estimation** - The circle centers are estimated by detect5ing the peaks in the accumulator array corresponding to the circles' centers. Figure 2.20b shows an example of the candidate pixels (solid dots) lying on an actual circle (solid circle), and their voting patterns (dashed circles) which coincide at the center of the actual circle.

3. **Radius Estimation** - If more than one radius uses the same accumulator array, then the radii of the detected circles has to be estimated.

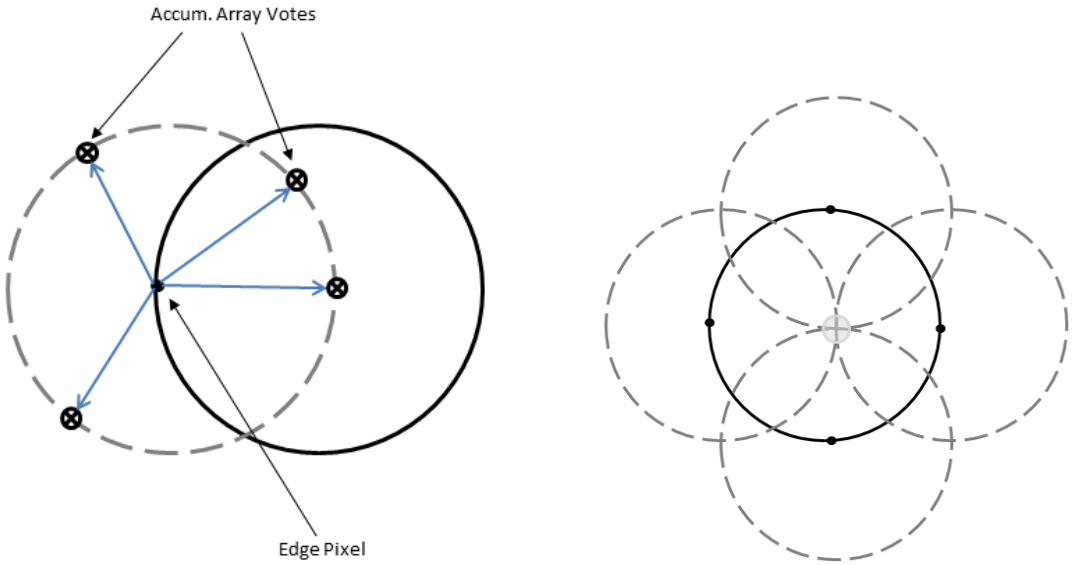

(a) (b)

Figure 2.20: Circular Hough Transform (CHT)

2.6 Summary

This chapter informs the reader about the anatomy of the breast more specifically its constituting structures. This chapter also makes a brief overview of the acquisition process and how each structure appears in a B-mode ultrasound image. Furthermore, shows a review of the preprocessing and segmentation techniques used in the past and in the present.

It is worth noting that many of the papers have as goal to do classification of the tumor as malignant or benign after preprocessing and its segmentation. However, that step is out of the scope of this dissertation and, thus, is not addressed.

In the next chapter some of these methods are implemented and tested namely the Median filter and the Anisotropic Diffusion Guided by Log–Gabor filters (ADLG) in the case of pre-processing and for segmentation, K-means clustering, Mean shift clustering, Watershed segmentation, Active contour model (Snakes), Region Growing and Minimum Path. The first three for both lesions and anatomical structures and the rest just for lesions.

Chapter 3

Breast ultrasound segmentation

2D Ultrasound Imaging has not yet been sufficiently studied for multi-modal registration. This is due to the low resolution of this type of images and the amount of speckle noise that is inherent to them.

However, landmark segmentation of anatomical breast structures in ultrasound imaging is still of the utmost importance in order to complete the multi-modality radiologic imaging combination and further empower the patients on the decision process.

This chapter details the experimental approach to the problem and the alternatives studied for segmentation of the breast images assuming the previous detection of the tumor's centroid. The chapter starts by introducing the dataset used. Then follows the idea behind the acquisition image cropping phase and the reasoning behind the chosen pre-processing method and lastly the different approaches to segmentation attempted throughout the development of the project.

3.1 Dataset description

During the development of this dissertation, 2 datasets were used for testing and comparison. One of the datasets is comprised of 443 ultrasound B-mode breast images from 18 different patients and contains the manual delineation of lesions by the assigned radiologist for the project, Rute Santos. In this dataset, images are in the format **DICOM** which is the standard for the communication and management of medical imaging information and related data. The annotations are in **Text file** format.

The other dataset consists of 75 images from 10 different patients and is composed of manual delineations of the several anatomical structures, again, ultrasound B-mode breast images by the same physician. In this dataset, the images are also in DICOM format. However, the annotations are not in Text file format as in the other dataset but in DICOM format as well.

Because of the computation time it takes to generate results and the delay in receiving the annotations, two validation datasets were used. The first one, for lesions, consisting of 54 images, 3 for each patient and the second one, for anatomical structures, consisting of 25 images from 3 patients.

After obtaining the optimal parameters for each method for the two validation sets, those parameters were replicated and used in the complete datasets.

3.2 Models

Although several methods were tested during the development of this dissertation, they can be grouped into 3 different pipeline models: two for lesion segmentation and one for anatomical structures segmentation. The first lesion segmentation pipeline (#1) is composed of 4 modules. In the first module, the image is preprocessed using one of several filters mentioned in the next section, ADLG or Median filter. The resulting image is segmented using one of the following techniques: K-means clustering, Mean shift clustering or Watershed. The following module expects prior detection of the lesion centroid and uses it to select the desired object.

Finally, several metrics are calculated to evaluate the quality of the segmentation, more specifically using Pixel- Area and Contour-wise metrics. A visual representation of this pipeline is illustrated below in Figure 3.1.

Figure 3.1: Pipeline #1

The second lesion segmentation pipeline (#2) is composed of 4 modules as well. However, in this case the lesion selection must be done prior to the segmentation since its centroid and/or bounding box (depending on the method) are used to segment the designated object.

In this model, the pre-processing methods used are the same as above. For segmentation three techniques were used: Active contour model (Snakes), Region Growing and Polar Minimum Path. The evaluation metrics too remain the same. A descriptive diagram of this pipeline is depicted below in Figure 3.2.

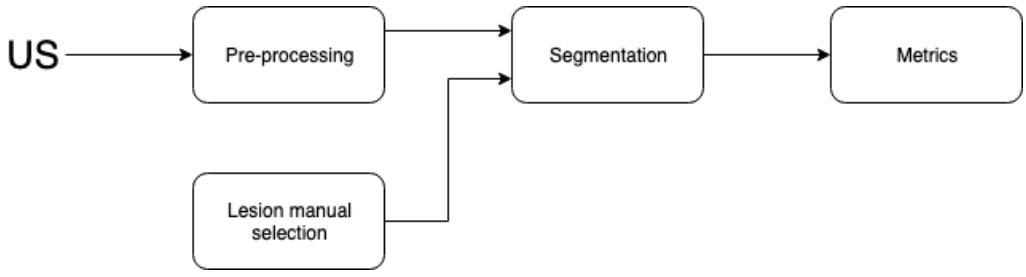

Figure 3.2: Pipeline #2

The third pipeline (#3) is that of anatomical structures segmentation and is composed of 4 modules.

This pipeline is very similar to the first pipeline presented above with the additional module of a Minimum Path algorithm instead of the lesion selection module, after the segmentation techniques are used. In this case, the segmentation methods used are K-means clustering, Mean shift clustering and Watershed.

After performing these segmentation methods, a minimum path algorithm [49] finds the shortest paths connecting the two margins of the image. Figure 3.3 portrays this pipeline.

To evaluate the results, each margin-to-margin line was considered, in order from the top of the image to the bottom, to correspond to skin, subcutaneous fat and mammary gland. Other structures were collectively considered as thoracic region due to the discrepancies in the ground truth annotations.

Still in this matter, due to time constraints, the metrics for the validation set were calculated to evaluate the average performance of the methods for all three structures combined instead of separately. In the complete dataset, however, results are detailed for each structure, including the thoracic region, as well as the average.

Figure 3.3: Pipeline #3

3.3 Metrics

In order to assess the results from each of the methods tested, 6 Pixel-Area and Contour-wise metrics were computed, namely the Hausdorff distance (HAUSD), the Sørensen–Dice coefficient (SD), the Area Overlap Measure (AOM), the Combined Measure (CM) of AOM, the Average Minimum Euclidean Distance (AMED), and the Average Distance (AD). Below follows a comprehensive explanation of these metrics.

The Hausdorff distance [39] measures how far two subsets of a metric space are from each other, in other words, it is the longest distance possible between a point in one of the two sets (supremum) to the closest point in the other set (infimum). If X and Y are two non-empty subsets of a metric space (M,d) where M is a set and d d is a metric on M, then their Hausdorff distance, $d_H(X,Y)$, can be defined as:

$$d_{\mathrm{H}}(X,Y) = \max\{\sup_{x\in X}\inf_{y\in Y} d(x,y), \sup_{y\in Y}\inf_{x\in X} d(x,y)\},$$

where *sup* represents the supremum and *inf* the infimum.

The Sørensen–Dice coefficient [60][19] gauges the similarity between two sets. Given two sets X, Y:

$$SD = \frac{2|X \cap Y|}{|X|+|Y|}$$

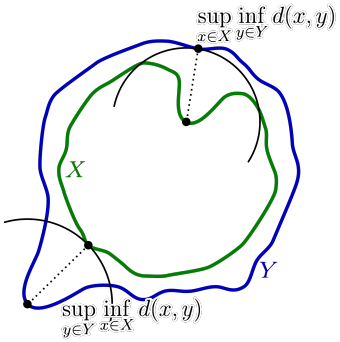

Figure 3.4: Components of the calculation of the Hausdorff distance between the green line X and the blue line Y [67]

where $|X|$ and $|Y|$ are the number of elements in each set.

This statistic equals twice the number of elements common to both sets divided by the sum of the number of elements in each set.

The Area Overlap Measure [22] can be defined as the ratio of the intersection area of S and T and the joint area of S and T, where S represents the segmented region and T represents the ground-truth region of the same region:

$$P_1 = \frac{|S \cap T|}{|S \cup T|}$$

From here, two measures can be deduced:

Measure of undersegmentation - This measure is defined as the ratio of the unsegmented area and the ground-truth area T:

$$P_2 = \frac{|T \setminus (|S \cap T|)|}{|T|}$$

Measure of oversegmentation - This measure is defined as the ratio of segmented unwanted area and the segmented area S:

$$P_2 = \frac{|S \setminus (|S \cap T|)|}{|S|}$$

The Combined Measure of AOM is used when none of the three criteria mentioned above (overlap, under and oversegmentation are preferred during the evaluation, and thus equal weights are assigned to each of the three criteria and the combined metric is defined as:

$$P = \frac{P_1 + (1 - P_2) + (1 - P_3)}{3}$$

The Average Minimum Euclidean Distance is, as the very name indicates, the average value of the Euclidean Distance between a point in a set S and the closest point in the other set T. Let $p = (p1, p2)$ and $q = (q1, q2)$ be two points in the Euclidean plane (two-dimensional space), then

the Euclidean distance between points p and q is the length of the line segment connecting them $\overline{\mathbf{pq}}$ and is given by:

$$d(\mathbf{p},\mathbf{q}) = \sqrt{(q_1 - p_1)^2 + (q_2 - p_2)^2}$$

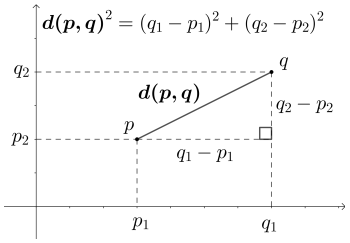

Figure 3.5: Euclidean distance in R^2 [66]

The Average Distance, or the Average Hausdorff Distance, between two sets, S and T, is the Hausdorff Distance averaged over all points. The former is known to be stable and less sensitive to outliers than the latter and it can be defined by:

$$AD(S,T) = max(d(S,T), d(S,T))$$

where $d(S,T)$ is the directed Average Hausdorff distance that is given by

$$d(S,T) = \frac{1}{N} \times \sum_{s \in S} \min_{t \in T} \| s - t \|$$

Although all of the metrics above were computed for each image, this dissertation only shows, and compares, two of them: Sørensen–Dice coefficient (SD) and Average Distance (AD). The first is used to estimate the area similarity between the ground truth and the segmentation result and the second is used to evaluate the similarity between the contours of the structures, again, between the ground truth and the segmentation result.

3.4 Pre-processing

Ultrasound image modality are characterized by suffering from an intrinsic artifact called speckle noise, which degrades spatial and contrast resolution and obscures the screened anatomy. Hence, it is important to reduce speckle artifacts before performing image segmentation. In addition, the trade-off between smoothing level and preservation of the structure's contour details should be addressed by speckle reduction schemes.

In this scenario, two despeckling methods were tested. One of them based on anisotropic diffusion guided by Log–Gabor filters (ADLG) [23] and a 2-D median filter [44] with a 9×9 kernel. The former method allows to set the maximum number of iterations for diffusion. The values tested for this parameter were 50, 100, 200, 500 and 1000 iterations as exemplified in Figure 3.6.

Additionally, for K-means clustering the H-Maxima Transform was used to suppress all maxima in the intensity image whose height were less than 0%, 20% and 40% of the image's intensity range. This was used to reduce the noise inherent to ultrasound images and prevent oversegmentation. Watershed uses the H-minima Transform for the same purpose with values 0%, 5%, 10% and 20%.

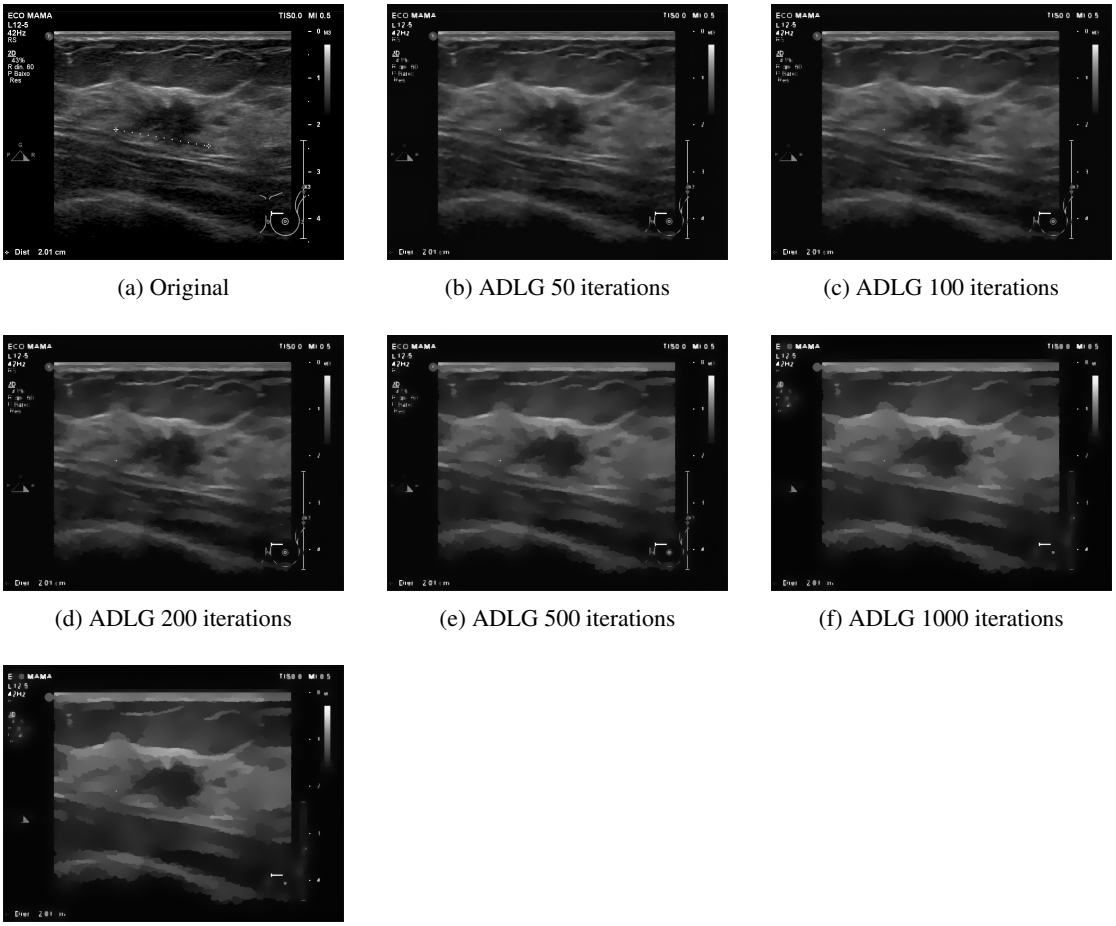

(a) Original (b) ADLG 50 iterations (c) ADLG 100 iterations

(d) ADLG 200 iterations (e) ADLG 500 iterations (f) ADLG 1000 iterations

(g) Median 9x9

Figure 3.6: Pre-processing methods used

3.5 Acquisition window

Ultrasound images usually have information to aid the physician's comprehension such as scales and brightness. As seen below in Figure 3.7a, this information is most prevalent outside the acquisition window. Therefore, in order to decrease the potential errors of segmentation and also to reduce the processing time only the acquisition window of the ultrasound images was kept for further processing.

To start, a simple morphological opening of the pre-processed image was performed with a disk shaped structuring element of 15 pixels in radius. With this small bright objects from the

foreground are removed. An example result is depicted in Figure 3.7.

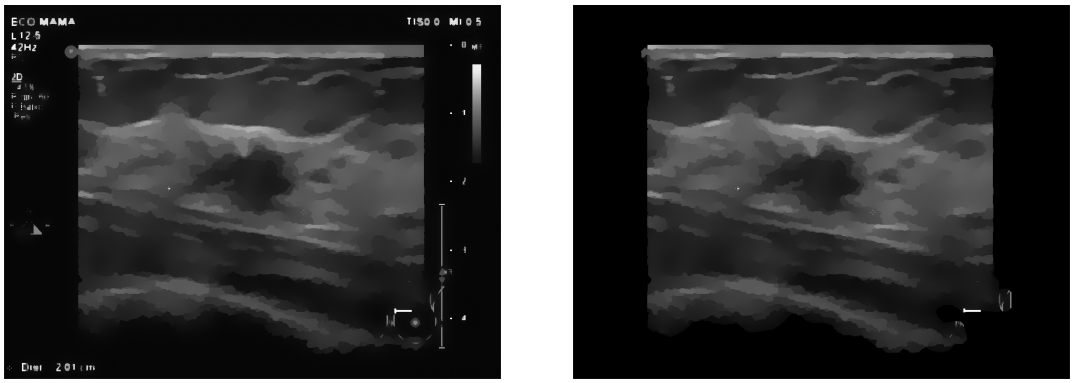

(a) Original ADLG (b) Original ADLG after Opening operation

Figure 3.7: Original ADLG and the result after performing an Opening operation

The next step is to find within the result of the last step the Area and corresponding linear indices of the pixels in each of the 8-connected components left so to sort them and find the component with the largest area. This component will most likely represent the desired acquisition window and the intensity of each of its pixels is copied to a matrix of zeros of the same size of the original image. This is done because there is no way of knowing the dimensions of the acquisition window for proper reconstruction.

The solution to this problem was to compute the Standard Hough Transform (SHT) which is designed to detect lines. The resulting Hough matrix is illustrated in Figure 3.8.

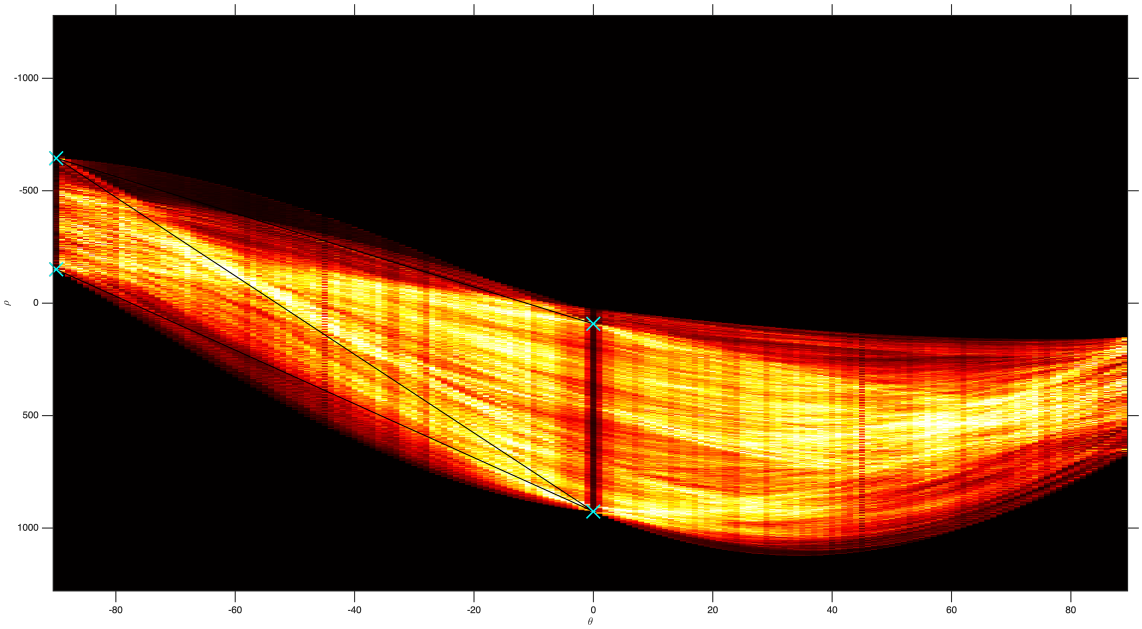

Figure 3.8: Hough Matrix with the 4 lines detected (blue crosses)

After computing the SHT, the following procedure was to find the peaks in the parameter

space which might correspond to the boundary lines of the acquisition window in the image. The value of 0.3 $\times$ maximum value of the Hough transform matrix and a maximum of 4 peaks successfully detected the lines. The first value was purely experimental whereas the reasoning behind maximum number of peaks was to find the four corresponding to the boundaries. Each line has a starting point and an ending point as well as a theta and a rho already detailed in Subsection 2.5.

In order to find the first row of the designated window theta must have an absolute value of 90º because it is a horizontal line. The last row is based on the fact that the last non zero pixel of the image will belong to this row. Therefore, the said pixel is found and its corresponding row is chosen as the last row. The first and last columns are found by selecting, correspondingly, the minimum and maximum of column values of the two element vector specifying the coordinates of the end-point of the line segments stated above.

The acquisition window is then cropped according to the specified values of the boundaries. After that, the median and the standard deviation of each of the rows starting from all four directions (top, bottom, left and right) are computed and the image is cropped until two criteria are met both in rows and columns.

$$30 \leqslant \textit{median value} \leqslant 240 \wedge \textit{std value} \geqslant 20$$

This is used for two reasons. One, in the original images there was always a white row above the acquisition window already present in the original ultrasound and inherent to the physical factors of the acquisition process, and two the reduced size of the resulting cropped image increases the speed of processing. Therefore the stated criteria was experimentally defined and kept due to the satisfactory results and increase in performance.

The ending result is demonstrated in Figure 3.9.

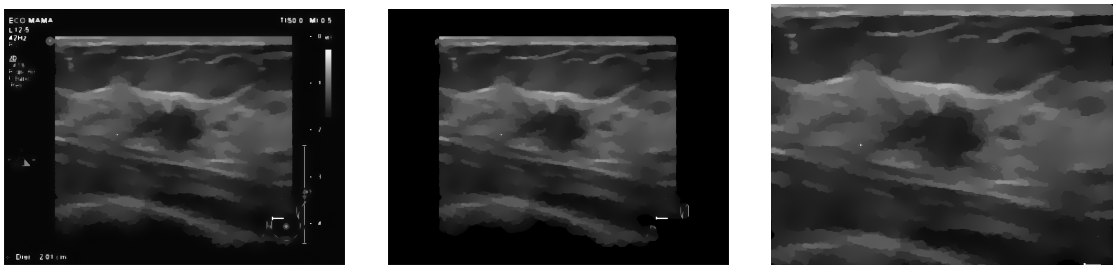

(a) Original ADLG (b) Original ADLG + Opening (c) Original ADLG + Crop

Figure 3.9: ADLG pre-processing experiments

3.6 Segmentation

Having the image pre-processed and the acquisition window cropped out of the ultrasound image, the next step is to perform segmentation.

As stated in Section 3.2, three pipelines were adopted during the development of this project. Below follows the segmentation methods used in each pipeline model. Each method includes the resulting metrics and a brief discussion on the best parameters to be used. In the end is shown a comparison between each method for the type of structure to be segmented (lesions or anatomical structures) and a final analysis with visual comparison of example images.

Furthermore, the visual results displayed in this section are representations of the region detection measurements towards the ground truth of the exemplifying image, Figure 3.10a. The ground truths for lesions and anatomical structures are illustrated below in Figure 3.10b and Figure 3.10c, respectively.

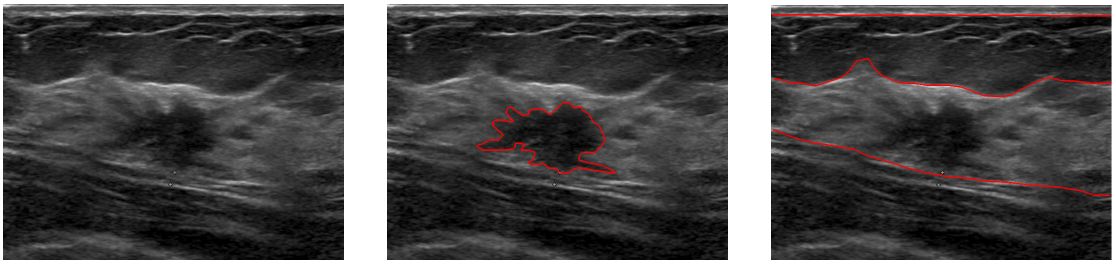

(a) Original image (b) Lesion ground truth (c) Anatomical structures ground truth

Figure 3.10: Original image and lesion's and anatomical structures' ground truths

3.6.1 Pipeline #1

3.6.1.1 K-means clustering

This method performs K-means clustering to partition the observations of the image into K clusters and uses the squared Euclidean distance metric and the K-means++ algorithm [5] for cluster center initialization. Contrarily to K-means, which starts with allocating cluster centers randomly and then looks for "better" solutions, K-means++ starts with the allocation of one cluster center randomly and then searches for other centers given the first one.

A grid search was used to test several parameters:

- **Input image:** Original, ADLG filtered (50, 100, 200, 500, 1000 iterations), Median filtered with 9×9 kernel
- **H-max suppression:** 0%, 20%, 40% of image's intensity range
- **Number of clusters:** K = 2, 3, 4, 5, 6

The results for the validation set are displayed below in Tables 3.1 and 3.2 and show the best results for Median filtered with 9×9 kernel with 20% H-max suppression and for K = 4 clusters (both for SD and AD). Visual results are also displayed in Figures 3.11, 3.12 and 3.13.

	H-max	$K = 2$	$K = 3$	$K = 4$	$K = 5$	$K = 6$
Original	0%	0.14 (0.31)	0.32 (0.41)	0.37 (0.40)	0.31 (0.37)	0.30 (0.34)
	20%	0.26 (0.38)	0.37 (0.41)	0.51 (0.36)	0.46 (0.34)	0.37 (0.33)
	40%	0.31 (0.41)	0.46 (0.39)	0.48 (0.36)	0.45 (0.34)	0.40 (0.30)
ADLG 50 iter	0%	0.18 (0.33)	0.38 (0.41)	0.49 (0.39)	0.43 (0.37)	0.42 (0.34)
	20%	0.26 (0.38)	0.46 (0.40)	0.58 (0.32)	0.46 (0.33)	0.43 (0.33)
	40%	0.31 (0.40)	0.56 (0.36)	0.51 (0.34)	0.46 (0.32)	0.45 (0.29)
ADLG 100 iter	0%	0.17 (0.32)	0.41 (0.40)	0.47 (0.40)	0.43 (0.38)	0.41 (0.36)
	20%	0.27 (0.39)	0.50 (0.39)	0.58 (0.34)	0.49 (0.34)	0.43 (0.33)
	40%	0.34 (0.41)	**0.59** (0.34)	0.52 (0.35)	0.41 (0.35)	0.43 (0.29)
ADLG 200 iter	0%	0.16 (0.32)	0.42 (0.41)	0.46 (0.40)	0.45 (0.37)	0.42 (0.35)
	20%	0.27 (0.39)	0.50 (0.39)	0.52 (0.36)	0.47 (0.35)	0.46 (0.31)
	40%	0.34 (0.40)	0.56 (0.36)	0.53 (0.35)	0.48 (0.33)	0.39 (0.32)
ADLG 500 iter	0%	0.19 (0.34)	0.39 (0.41)	0.51 (0.38)	0.48 (0.36)	0.40 (0.37)
	20%	0.26 (0.38)	0.46 (0.39)	0.55 (0.35)	0.48 (0.35)	0.45 (0.34)
	40%	0.37 (0.41)	0.52 (0.40)	0.49 (0.34)	0.45 (0.34)	0.40 (0.33)
ADLG 1000 iter	0%	0.24 (0.38)	0.41 (0.42)	0.53 (0.38)	0.48 (0.37)	0.37 (0.37)
	20%	0.26 (0.37)	0.46 (0.41)	0.56 (0.34)	0.45 (0.36)	0.47 (0.36)
	40%	0.36 (0.41)	0.55 (0.37)	0.44 (0.37)	0.46 (0.36)	0.43 (0.34)
Median 9x9	0%	0.25 (0.36)	0.40 (0.41)	0.51 (0.38)	0.45 (0.35)	0.43 (0.33)
	20%	0.32 (0.38)	0.49 (0.38)	**0.60** (0.29)	**0.52** (0.29)	0.47 (0.28)
	40%	**0.44** (0.39)	0.58 (0.33)	0.57 (0.29)	0.51 (0.26)	0.45 (0.27)

Column $K = 6$ has several maxima. However, none of them is the maximum value of the table.

Therefore, no value in that column is shown in bold formatting

Table 3.1: K-means clustering (lesions) - Validation metrics (average and standard deviation) for parameters choice using Sørensen–Dice coefficient (SD)

	H-max	$K = 2$	$K = 3$	$K = 4$	$K = 5$	$K = 6$
Original	0%	33.8 (24.4)	27.2 (27.8)	24.7 (28.8)	24.6 (26.0)	25.2 (28.6)
	20%	30.1 (26.8)	25.2 (29.3)	15.0 (24.1)	15.4 (25.7)	17.6 (24.3)
	40%	29.8 (31.8)	21.2 (29.6)	16.0 (24.5)	16.3 (24.2)	14.7 (23.5)
ADLG 50 iter	0%	34.2 (22.2)	21.7 (26.1)	18.7 (26.4)	17.5 (24.1)	16.7 (23.0)
	20%	30.6 (24.7)	19.2 (25.1)	10.8 (21.4)	14.0 (22.7)	14.8 (22.7)
	40%	28.2 (26.7)	**12.0** (18.4)	14.6 (24.5)	14.1 (24.0)	11.6 (20.9)
ADLG 100 iter	0%	34.2 (21.8)	19.8 (24.1)	19.1 (26.7)	17.5 (23.2)	17.4 (23.7)
	20%	28.8 (23.8)	17.2 (22.9)	11.5 (21.3)	13.2 (22.1)	15.1 (22.8)
	40%	29.6 (30.7)	12.1 (20.9)	13.3 (22.8)	17.4 (24.5)	12.7 (22.6)
ADLG 200 iter	0%	37.0 (23.7)	20.3 (24.7)	20.7 (27.9)	15.7 (22.0)	16.9 (23.3)
	20%	28.4 (24.0)	15.6 (20.8)	13.7 (21.2)	14.3 (22.6)	11.7 (20.7)
	40%	29.6 (30.8)	13.4 (23.2)	12.8 (22.2)	13.8 (22.7)	16.4 (23.8)
ADLG 500 iter	0%	34.5 (24.7)	23.0 (25.3)	16.3 (24.8)	14.9 (22.6)	19.4 (24.9)
	20%	31.7 (28.2)	18.7 (24.6)	11.6 (19.9)	15.9 (24.7)	15.5 (22.6)
	40%	28.9 (32.7)	17.5 (25.8)	14.5 (24.9)	17.8 (26.2)	17.2 (24.2)
ADLG 1000 iter	0%	36.0 (28.7)	20.8 (24.2)	14.9 (23.0)	16.3 (24.0)	19.9 (24.7)
	20%	33.5 (27.4)	20.2 (25.6)	12.5 (22.9)	16.8 (25.0)	16.7 (24.8)
	40%	29.7 (31.2)	16.6 (28.4)	17.2 (23.6)	16.5 (24.7)	15.7 (22.2)
Median 9x9	0%	27.9 (21.7)	18.6 (23.1)	16.1 (25.1)	16.3 (24.2)	15.5 (24.0)
	20%	**24.7** (24.5)	17.5 (26.3)	**7.7** (15.1)	10.3 (20.5)	**9.3** (17.3)
	40%	25.2 (32.4)	12.5 (22.2)	9.4 (20.3)	**8.4** (16.8)	11.7 (21.4)

Table 3.2: K-means clustering (lesions) - Validation metrics (average and standard deviation) for parameters choice using Average Distance (AD)

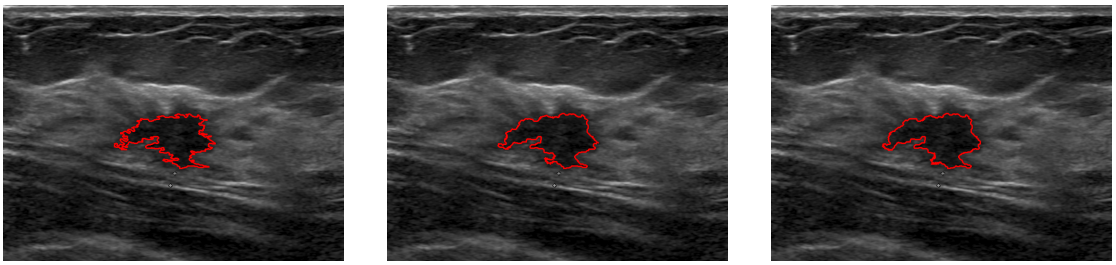

(a) Original (b) ADLG 50 iterations (c) ADLG 100 iterations

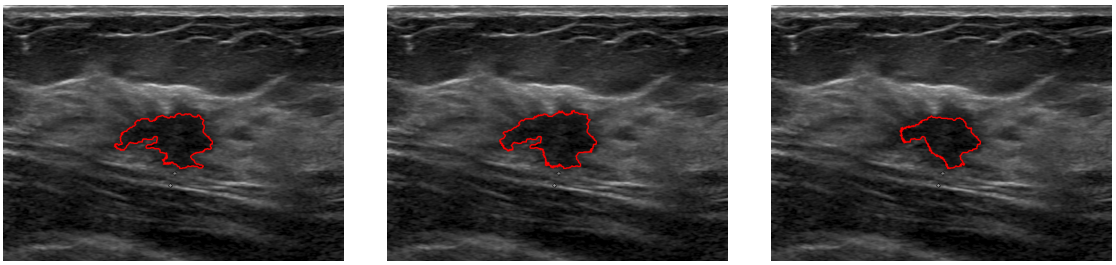

(d) ADLG 200 iterations (e) ADLG 500 iterations (f) ADLG 1000 iterations

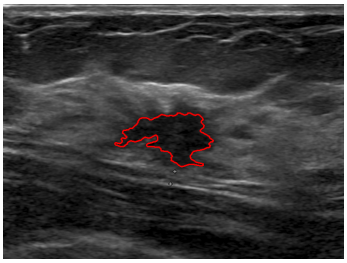

(g) Median 9x9 filter

Figure 3.11: K-means variation with pre-processing ($K = 4$ and H-max = 20%)

Figure 3.11 shows that K-means does not vary too much with the pre-processing method. Although some differences are visible, these can be attributed to ADLG's reduction of speckle artifacts which homogenizes pixels close to each other with similar intensity values.

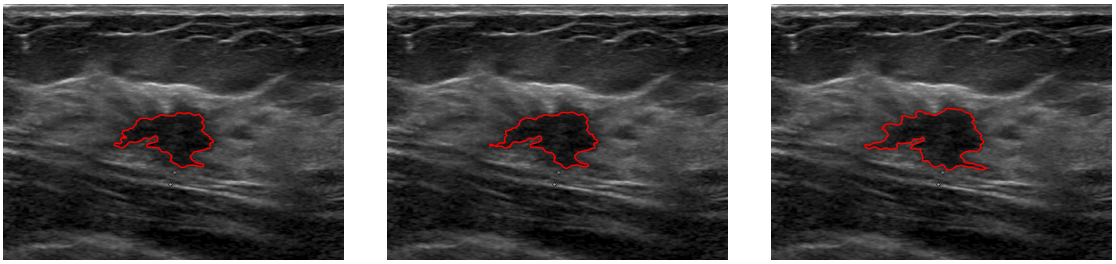

(a) H-max = 0% (b) H-max = 20% (c) H-max = 40%

Figure 3.12: K-means variation with H-max (Median 9x9 filter and $K = 4$)

Figure 3.12 suggests that the detected area increases with H-max suppression. This is explained by the fact that pixels that are connected will belong to the same object if their difference

in height is smaller than that specified by H-max. Therefore, with an increase in H-max the segmented area increases as well.

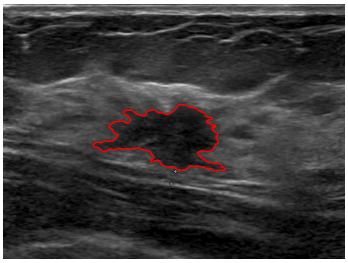

(a) $K = 2$

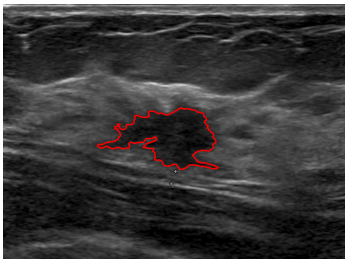

(b) $K = 3$

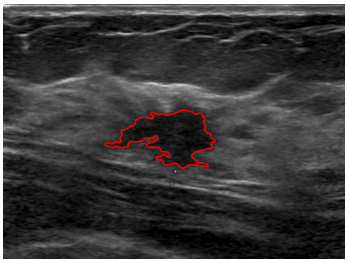

(c) $K = 4$

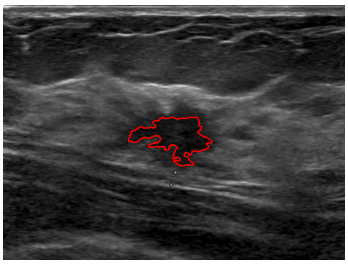

(d) $K = 5$

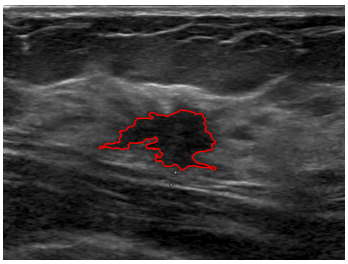

(e) $K = 6$

Figure 3.13: K-means variation with number of clusters (Median 9x9 filter and H-max=20%)

Figure 3.13 shows that, except for $K = 6$, as the number of clusters increases, the detected area decreases which is expected since each observation will belong to the cluster with the nearest mean and the difference between clusters means is smaller. The best results, as stated above, were for Median filtered with 9×9 kernel with 20% H-max suppression and for K = 4 clusters.

3.6.1.2 Mean shift clustering

This method performs Mean shift clustering using the cluster centroid locations from K-means as initial seeds to segment lesions in the ultrasound image. The parameters used for K-means result from Section 3.6.1.1 experiments and they are $K = 4$ clusters, $H - max = 20\%$ and on the median filtered by a 9x9 kernel image. The implementation uses a Mean shift clustering algorithm adaptation of [24] by Co-supervisor João Pedro Fonseca Teixeira which has several parameters apart from the initial seeds such as bandwidth and X,Y position weights relative to image.

A grid search was used to test the several parameters:

- **Input image:** Original, ADLG filtered (50, 100, 200, 500, 1000 iterations), Median filtered with 9×9 kernel
- **Bandwidth:** 0.02, 0.05, 0.1
- **Position weights:** 0.0625, 0.125, 0.25 and 1

The complete results for the validation set are present in Appendix A.1. Because of the high number of results for this experiment, only the 8 best combinations for SD (and their corresponding AD results) and the 2 worst are shown below in Tables 3.3 and 3.4.

Best parameters				
	ADLG 1000 iter Bandwidth = 0.1 Weight = 1	ADLG 500 iter Bandwidth = 0.1 Weight = 1	ADLG 200 iter Bandwidth = 0.1 Weight = 1	ADLG 50 iter Bandwidth = 0.1 Weight = 1
SD	**0.57** (0.22)	0.55 (0.21)	0.52 (0.22)	0.51 (0.24)
	ADLG 100 iter Bandwidth = 0.1 Weight = 1	Median 9x9 Bandwidth = 0.1 Weight = 1	Original Bandwidth = 0.1 Weight = 1	ADLG 1000 iter Bandwidth = 0.05 Weight = 0.25
SD	0.51 (0.22)	0.50 (0.23)	0.47 (0.25)	0.42 (0.23)
Best parameters				
	Original Bandwidth = 0.02 Weight = 0.25	ADLG 1000 iter Bandwidth = 0.1 Weight = 1	ADLG 500 iter Bandwidth = 0.1 Weight = 1	Original Bandwidth = 0.1 Weight = 1
AD	**5.79** (7.17)	6.61 (8.22)	6.69 (8.51)	7.09 (10.66)
	Median 9x9 Bandwidth = 0.1 Weight = 1	ADLG 200 iter Bandwidth = 0.1 Weight = 1	ADLG 50 iter Bandwidth = 0.02 Weight = 0.25	Original Bandwidth = 0.05 Weight = 1
AD	7.12 (8.32)	7.30 (9.21)	7.41 (10.13)	7.71 (9.62)

Table 3.3: Mean shift clustering (lesions) - Best validation metrics combination (average and standard deviation) for parameters choice using Sørensen–Dice coefficient (SD) and Average Distance (AD)

Worst parameters		
	Original Bandwidth = 0.02 Weight = 1	Median 9x9 Bandwidth = 0.02 Weight = 1
SD	**0.055** (0.078)	0.070 (0.090)
Worst parameters		
	ADLG 200 iter Bandwidth = 0.1 Weight = 0.0625	ADLG 50 iter Bandwidth = 0.1 Weight = 0.0625
AD	**111.72** (62.45)	111.11 (57.67)

Table 3.4: Mean shift clustering (lesions) - Worst validation metrics combination (average and standard deviation) for parameters choice using Sørensen–Dice coefficient (SD) and Average Distance (AD)

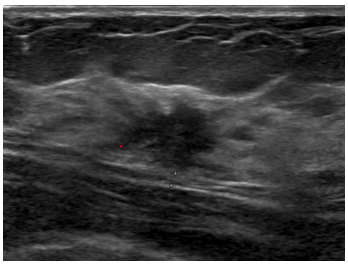

(a) Original

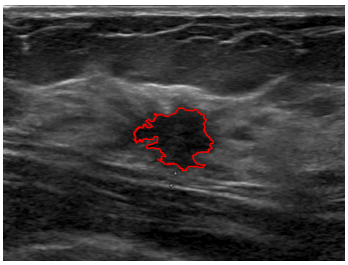

(b) ADLG 50 iterations

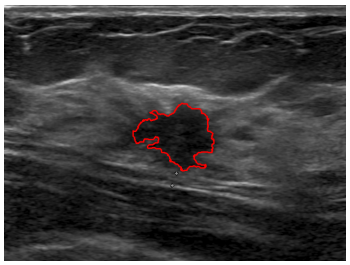

(c) ADLG 100 iterations

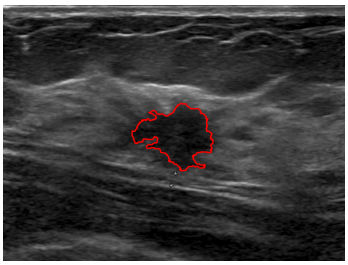

(d) ADLG 200 iterations

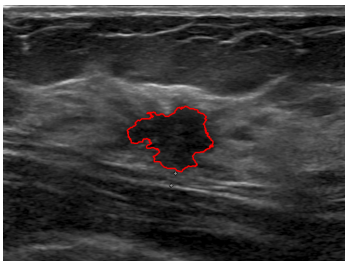

(e) ADLG 500 iterations

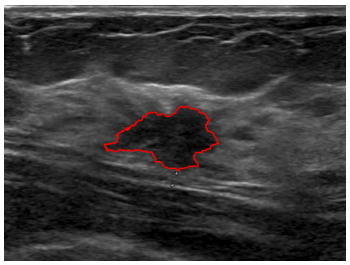

(f) ADLG 1000 iterations

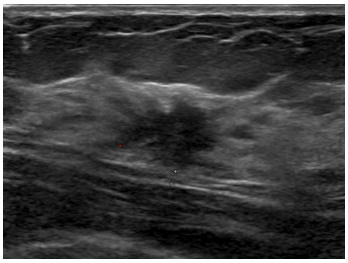

(g) Median 9x9 filter

Figure 3.14: Mean shift variation with pre-processing ($Bandwidth = 0.1$ and $X, Yweights = 1$)

Figure 3.14 demonstrates that Mean shift has difficulty dealing with speckle noise since both 3.14a and 3.14g detect a small artifact and not the lesion itself. Other than that, the size of the segmented region is approximately the same with smoother edges as the number of iterations in ADLG increases. It is worth noting that with 1000 iterations the detected area increases considerably.

(a) $Bandwidth = 0.02$

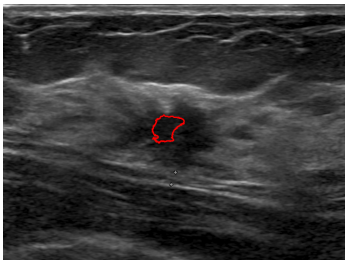

(b) $Bandwidth = 0.05$

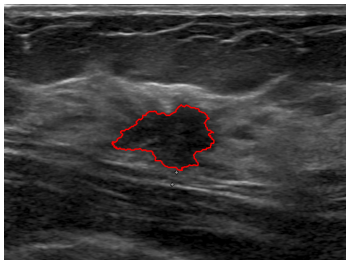

(c) $Bandwidth = 0.1$

Figure 3.15: Mean shift variation with bandwidth (ADLG with 1000 iterations and $X, Yweights = 1$)

Figure 3.15 indicates an increase in area detected with an increase in the value of bandwidth. This is expected since this parameter dictates the size of the region to search through.

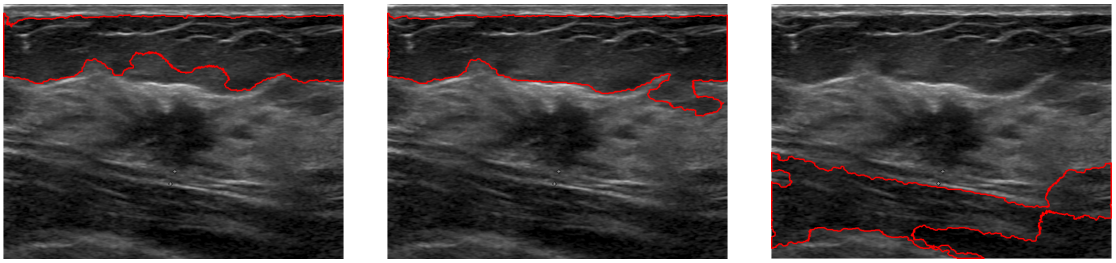

(a) $X,Yweights = 0.0625$ (b) $X,Yweights = 0.125$ (c) $X,Yweights = 0.25$

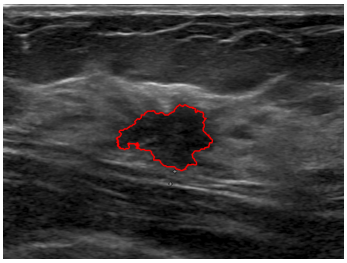

(d) $X,Yweights = 1$

Figure 3.16: Mean shift variation with $X,Yweights$ (ADLG with 1000 iterations and $Bandwidth = 0.1$)

Figure 3.16 shows that the spacial weights have a big influence in the segmented region. Interestingly, with smaller weights this method segments other structures, subcutaneous fat in Figures 3.16a and 3.16b and pectoral muscle in Figure 3.16c. With a spacial weight equal to the weight of the image, the method segments the lesion as expected. The best results, as shown above in Table 3.3, were for ADLG with 1000 iterations, Bandwidth = 0.1, and X,Y Weight = 1.

3.6.1.3 Watershed

The watershed transform finds "catchment basins" or "watershed ridge lines" in an image by treating it as a surface where light pixels represent high elevations and dark pixels represent low elevations. The watershed transform can be used to segment contiguous regions of interest into distinct objects. This watershed implementation uses the Fernand Meyer algorithm [48].

A grid search was used to test several parameters:

- **Input image:** Original, ADLG filtered (50, 100, 200, 500, 1000 iterations), Median filtered with 9×9 kernel
- **H-min suppression:** 0%, 5%, 10%, 20% of image's intensity range

The results for the validation set are displayed below in Tables 3.5 and 3.6 and show the best results for H-min = 5% and median filtered with 9×9 kernel image (both for SD and AD).

	H-min			
	0%	5%	10%	20%
Original	0.21 (0.26)	0.06 (0.09)	0.06 (0.07)	0.04 (0.06)
ADLG 50 iter	0.04 (0.07)	0.04 (0.05)	0.33 (0.27)	0.43 (0.29)
ADLG 100 iter	0.56 (0.20)	0.39 (0.22)	**0.57** (0.16)	0.52 (0.17)
ADLG 200 iter	0.30 (0.22)	0.56 (0.16)	0.51 (0.17)	0.29 (0.22)
ADLG 500 iter	0.56 (0.15)	0.47 (0.18)	0.29 (0.22)	**0.53** (0.17)
ADLG 1000 iter	0.47 (0.19)	0.26 (0.20)	0.52 (0.18)	0.44 (0.21)
Median 9x9	0.28 (0.21)	**0.58** (0.15)	0.55 (0.16)	0.33 (0.23)

Column $H-min = 0\%$ has several maxima.

However, none of them is the maximum value of the table.

Therefore, no value in that column is shown in bold formatting

Table 3.5: Watershed segmentation (lesions) - Validation metrics (average and standard deviation) for parameters choice using Sørensen–Dice coefficient (SD)

	H-min			
	0%	5%	10%	20%
Original	37.3 (44.4)	46.8 (36.7)	51.7 (40.3)	44.8 (33.0)
ADLG 50 iter	57.8 (44.3)	54.8 (43.6)	17.3 (22.0)	12.2 (20.8)
ADLG 100 iter	7.4 (17.2)	27.4 (39.7)	**5.8** (8.8)	**8.4** (11.8)
ADLG 200 iter	50.5 (55.3)	6.8 (9.8)	9.2 (12.8)	53.8 (55.8)
ADLG 500 iter	**6.6** (9.9)	11.7 (13.6)	53.6 (53.3)	8.8 (12.8)
ADLG 1000 iter	14.6 (18.8)	57.2 (50.0)	9.9 (13.9)	19.6 (24.9)
Median 9x9	54.1 (50.1)	**5.4** (8.9)	7.2 (12.2)	41.8 (49.2)

Table 3.6: Watershed segmentation (lesions) - Validation metrics (average and standard deviation) for parameters choice using Average Distance (AD)

As Figure 3.17 below shows, the original image, Figure 3.17a, suffers from oversegmentation which is a characteristic of the watershed method. After pre-processing for noise reduction, this method increases its performance. However, this method has difficulty detecting the contour of the object and detects neighouring areas around the object of interest.

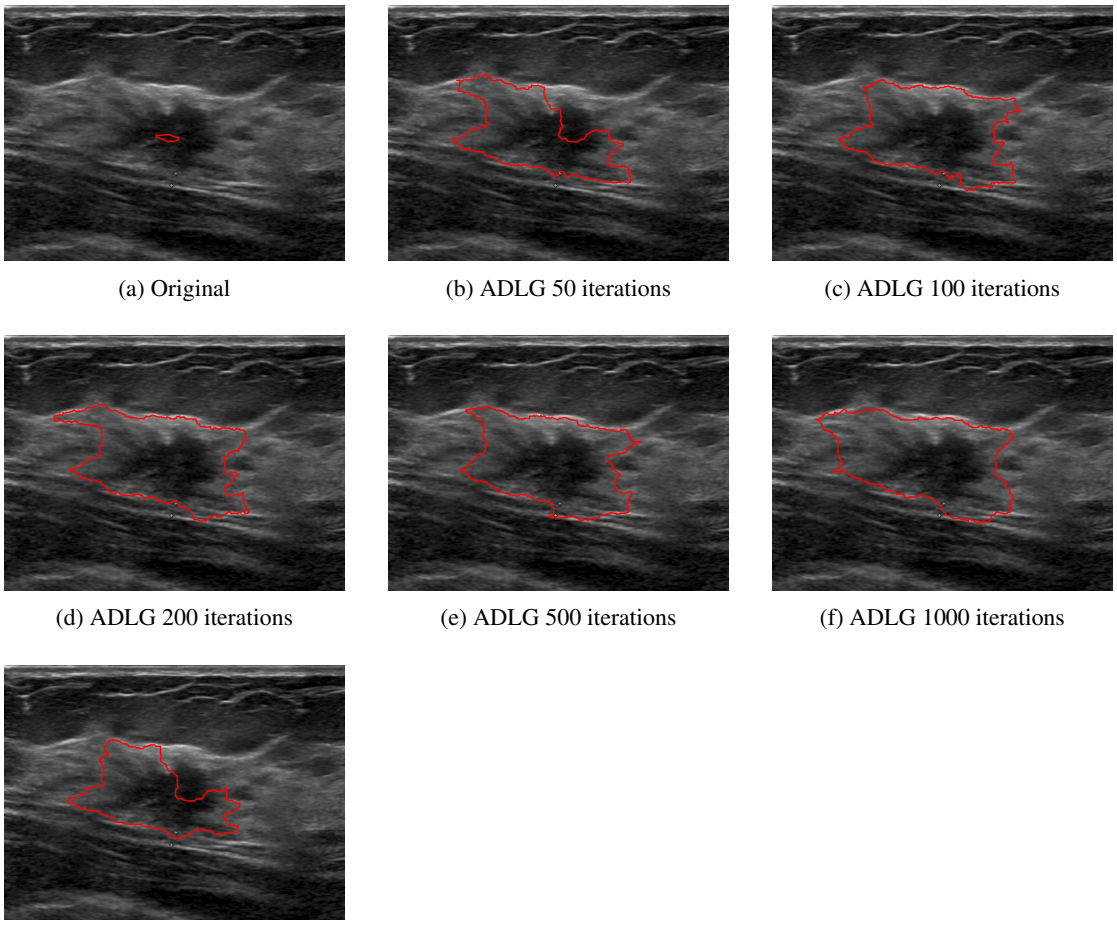

(a) Original (b) ADLG 50 iterations (c) ADLG 100 iterations

(d) ADLG 200 iterations (e) ADLG 500 iterations (f) ADLG 1000 iterations

(g) Median 9*x*9 filter

Figure 3.17: Watershed variation with pre-processing (H-min=5%)

Figure 3.18, in the next page, indicates an increase in segmented area with an increase in H-minima suppression. This is explained by the fact that H-minima Transform suppresses all minima in the image whose depth is less than that specified by H-min. Therefore, with an increase in H-min the segmented area increases as well. The best results, as stated above, were for Median filtered with 9×9 kernel with t% H-min suppression.

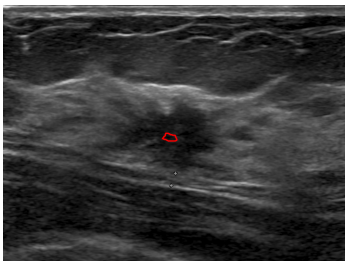

(a) H-min = 0%

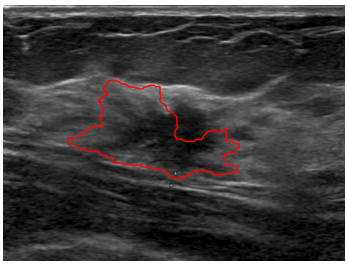

(b) H-min = 5%

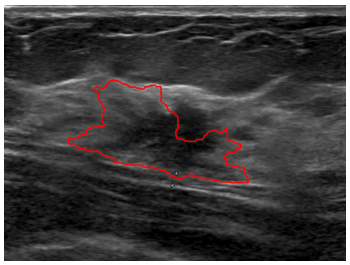

(c) H-min = 10%

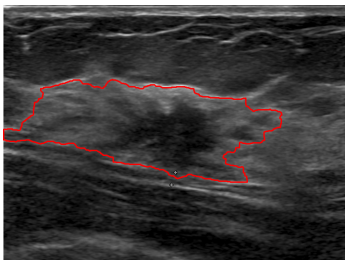

(d) H-min = 20%

Figure 3.18: Watershed variation with number of clusters (Median 9x9 filter)

3.6.2 Pipeline #2

3.6.2.1 Active contour model (Snakes)

Active contour model (snakes) makes use of energy constraints and forces the separation of region of interest in the image. The contour depends on various constraints based on which they are classified into different types such as gradient vector flow, balloon and geometric models.

This active contour implementation uses the Sparse-Field level-set method [65] for implementing active contour evolution and uses the boundaries of the regions in a mask as the initial state of the contour from where the evolution starts. Therefore, the mask given was the smallest possible, a 2x2 square that includes the centroid of the ground truth.

This implementation has several other parameters, namely the active contour method used for segmentation, the maximum number of iterations (N) to perform in evolution of the segmentation, the SmoothFactor (SF) which states the degree of smoothness or regularity of the boundaries of the segmented regions and the ContractionBias (CB) which is the tendency of the contour to grow outwards or shrink inwards.

For the first parameter, we had two choices, either **Edge** which is naturally biased towards shrinking inwards (collapsing) or **Chan-Vese** where the contour is unbiased, which means the contour is free to either shrink or expand based on the image features. The decision was to use Chan-Vese since the initial mask for growth was inside the contour.

For the rest of the parameters, a grid search was used:

- **Input image:** Original, ADLG filtered (50, 100, 200, 500, 1000 iterations), Median filtered with 9×9 kernel

- **Iterations:** 50, 100, 200, 500, 1000 iterations
- **SmoothFactor:** 0, 0.01, 0.04, 0.1, 0.2, 0.5
- **ContractionBias:** 0, -0.01, -0.04, -0.1, -0.2, -0.5 (Negative values bias the contour to grow outwards)

The complete results for the validation set are present in Appendix A.2. Because of the high number of results for this experiment, only the 8 best combinations for SD (and their corresponding AD results) and the 2 worst are shown below in Tables 3.7 and 3.8.

Best parameters				
	ADLG 500 iter N = 200 SF = 0.2 CB = -0.2	ADLG 200 iter N = 200 SF = 0.2 CB = -0.2	ADLG 1000 iter N = 200 SF = 0 CB = -0.1	ADLG 1000 iter N = 200 SF = 0.01 CB = -0.1
SD	**0.733** (0.20)	0.731 (0.20)	0.730 (0.21)	0.729 (0.21)
	ADLG 1000 iter N = 200 SF = 0.2 CB = -0.2	ADLG 50 iter N = 200 SF = 0.2 CB = -0.2	ADLG 500 iter N = 200 SF = 0 CB = -0.1	ADLG 500 iter N = 200 SF = 0.01 CB = -0.1
SD	0.729 (0.21)	0.728 (0.20)	0.727 (0.21)	0.727 (0.21)
Best parameters				
	Original N = 100 SF = 0 CB = -0.2	ADLG 50 iter N = 100 SF = 0 CB = -0.2	ADLG 50 iter N = 100 SF = 0.01 CB = -0.2	ADLG 200 iter N = 100 SF = 0 CB = -0.2
AD	**2.946** (4.41)	2.948 (4.21)	2.949 (4.27)	2.958 (4.01)
	ADLG 100 iter N = 100 SF = 0 CB = -0.2	Original N = 100 SF = 0.01 CB = -0.2	ADLG 200 iter N = 100 SF = 0.01 CB = -0.2	Median 9x9 N = 100 SF = 0.01 CB = -0.2
AD	2.961 (4.13)	2.961 (4.46)	2.962 (4.08)	2.973 (4.21)

N = Number of iterations

SF = SmoothFactor

CB = ContractionBias

Table 3.7: Active contour model segmentation (lesions) - Best validation metrics combination (average and standard deviation) for parameters choice using Sørensen–Dice coefficient (SD) and Average Distance (AD)

	Worst parameters	
	ADLG 1000 iter N = 50 SF = 0.5 CB = 0	ADLG 1000 iter N = 100 SF = 0.5 CB = 0
SD	**0.00171** (0.0025)	0.00171 (0.0025))
	Worst parameters	
	Original N = 1000 SF = 0.01 CB = -0.5	Original N = 1000 SF = 0 CB = -0.5
AD	**122.60** (52.96)	122.28 (53.32)

N = Number of iterations

SF = SmoothFactor

CB = ContractionBias

Table 3.8: Active contour model segmentation (lesions) - Worst validation metrics combination (average and standard deviation) for parameters choice using Sørensen–Dice coefficient (SD) and Average Distance (AD)

Figure 3.19 shows that pre-processing has no considerable effect on the active contour experiments. Little differences, such as contour smoothness and object area, are noticed which can be explained by difference in size and shape of the lesion in the pre-processed image.

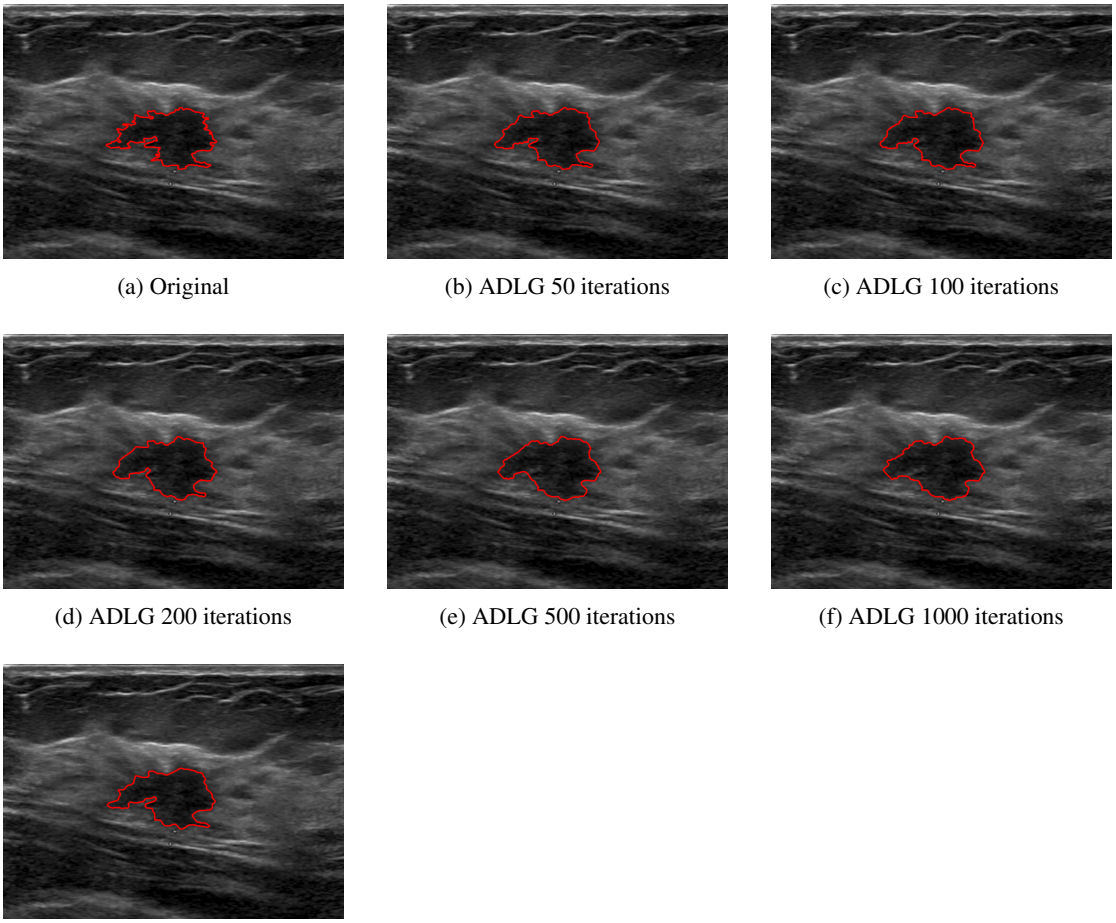

(a) Original (b) ADLG 50 iterations (c) ADLG 100 iterations

(d) ADLG 200 iterations (e) ADLG 500 iterations (f) ADLG 1000 iterations

(g) Median 9x9 filter

Figure 3.19: Active contour variation with pre-processing ($N = 200$, $SF = 0.2$, $CB = -0.2$)

In Figure 3.20, however, the similarity between the lesion and the segmented region grows with an increase in the number of iterations performed. This can be justified by the very nature of active contour which evolves until the maximum number of iterations has been reached. Nonetheless, there are no considerable differences visually between 3.20d and 3.20e which indicates that the growth rate has decreased and since the former has a faster computation speed than the latter it might be a good option to use it.

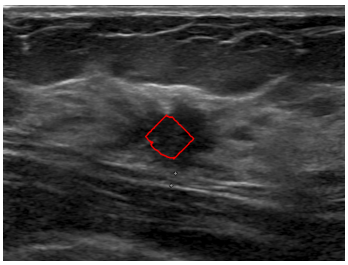

(a) N = 50 iterations

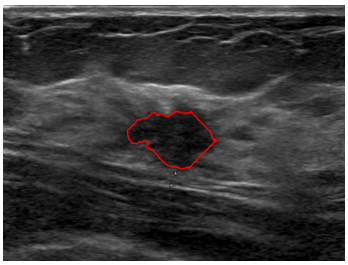

(b) N = 100 iterations

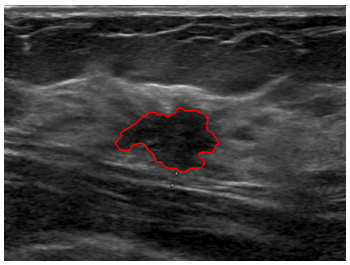

(c) N = 200 iterations

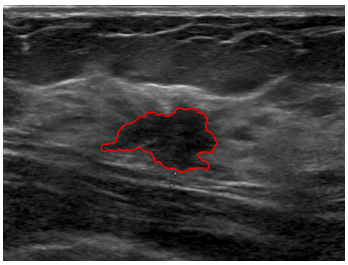

(d) N = 500 iterations

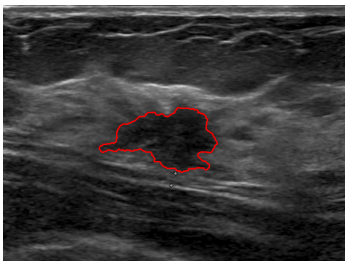

(e) N = 1000 iterations

Figure 3.20: Active contour variation with number of iterations N (ADLG with 500 iterations, $SF = 0.2$, $CB = -0.2$)

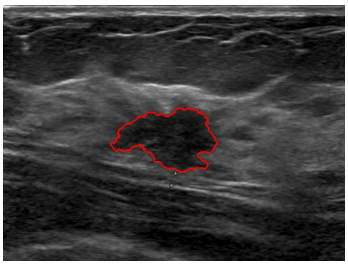

(a) $SF = 0$

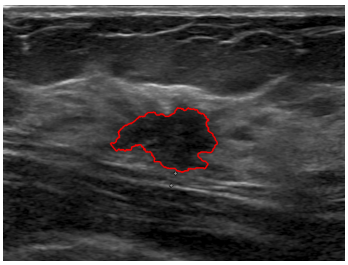

(b) $SF = 0.01$

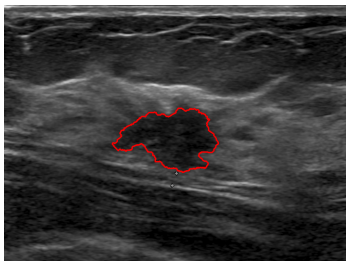

(c) $SF = 0.04$

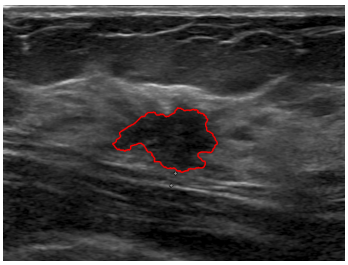

(d) $SF = 0.1$

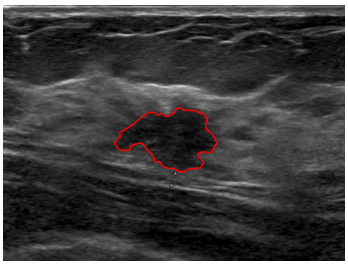

(e) $SF = 0.2$

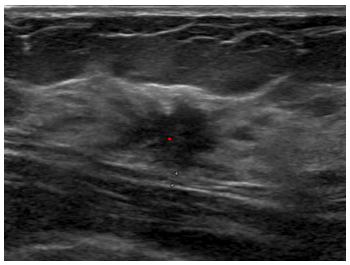

(f) $SF = 0.5$

Figure 3.21: Active contour variation with SmoothFactor (ADLG with 500 iterations, $N = 200$, $CB = -0.2$)

Figure 3.21 illustrates the effect of the SmoothFactor which specifies the degree of smoothness or regularity of the boundaries of the segmented regions. This parameter has a small effect on the outcome since all images, except the last one, are very similar apart from subtle differences in the

contour. In the last image, 3.21f, the contour seems to halt its growth. This gives us a warning that perhaps it is too big of a value for our type of image, in particular.

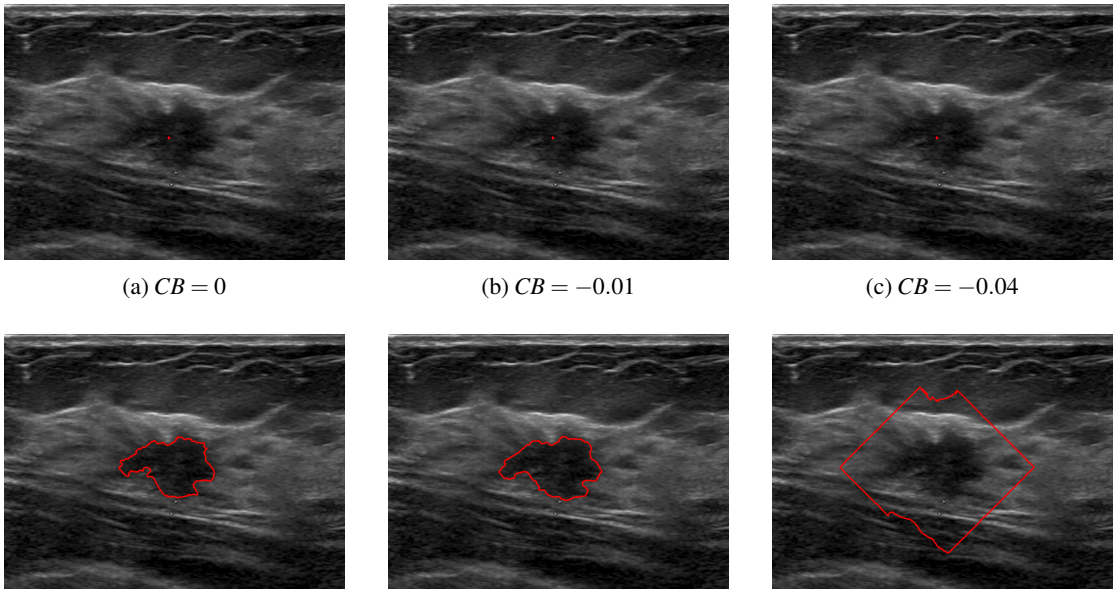

(a) $CB = 0$ (b) $CB = -0.01$ (c) $CB = -0.04$

(d) $CB = -0.1$ (e) $CB = -0.2$ (f) $CB = -0.5$

Figure 3.22: Active contour variation with ContractionBias (ADLG with 500 iterations, $N = 200$, $SF = 0.2$)

Finally, Figure 3.22 shows that perhaps values of ContractionBias, which is the tendency of the contour to grow outwards (negative) or shrink inwards (positive), close to 0 will allow the contour to grow with less difficulty. However, it is noticeable that from a certain value the contour will grow beyond the region of interest 3.22f.

The best results, as shown in Table 3.7 are for ADLG with 500 iterations, N = 200 iterations, SF = 0.2 and CB = -0.2.

3.6.2.2 Region growing

Region growing is a region-based image segmentation method that examines neighboring pixels of initial seed points and determines whether the pixel neighbors should be added to the region based on the threshold value used for aggregation criterion. This implementation is a MATLAB-optimized version of Daniel Kellner's code by the co-supervisor of this dissertation, João Pedro Fonseca Teixeira, and is a recursive region growing algorithm for 2D and 3D grayscale image sets with polygon and binary mask output.

A grid search was used to test several parameters:

- **Input image:** Original, ADLG filtered (50, 100, 200, 500, 1000 iterations), Median filtered with 9×9 kernel
- **Threshold value:** 2%, 5%, 10%, 15%, 20% of image's intensity range

The results for the validation set are displayed below in Tables 3.9 and 3.10 and show that SD is the highest for ADLG with 200 iterations and threshold value of 10% for aggregation criterion, and AD is the lowest for ADLG with 1000 iterations and threshold value of 5% for aggregation criterion.

	Threshold				
	2%	5%	10%	15%	20%
Original	0.21 (0.22)	0.45 (0.27)	0.55 (0.29)	0.52 (0.33)	0.37 (0.33)
ADLG 50 iter	0.24 (0.21)	0.47 (0.23)	0.58 (0.29)	0.53 (0.35)	0.33 (0.32)
ADLG 100 iter	0.27 (0.22)	0.49 (0.23)	0.58 (0.29)	0.52 (0.35)	0.38 (0.33)
ADLG 200 iter	0.29 (0.21)	0.49 (0.22)	**0.59** (0.28)	0.50 (0.35)	0.41 (0.34)
ADLG 500 iter	0.34 (0.20)	0.50 (0.21)	**0.59** (0.29)	0.55 (0.34)	0.42 (0.35)
ADLG 1000 iter	**0.40** (0.21)	**0.55** (0.21)	0.58 (0.28)	**0.57** (0.33)	**0.44** (0.35)
Median 9x9	0.26 (0.20)	0.49 (0.24)	0.57 (0.29)	0.53 (0.34)	0.41 (0.35)

Table 3.9: Region growing segmentation (lesions) - Validation metrics (average and standard deviation) for parameters choice using Sørensen–Dice coefficient (SD)

	Threshold				
	2%	5%	10%	15%	20%
Original	16.3 (17.9)	13.2 (22.1)	**19.7** (37.7)	**30.9** (44.1)	54.3 (55.5)
ADLG 50 iter	13.0 (15.2)	12.6 (21.8)	23.4 (44.2)	34.5 (48.0)	61.1 (53.9)
ADLG 100 iter	13.9 (16.4)	9.6 (18.7)	23.6 (44.6)	36.2 (49.8)	54.1 (54.2)
ADLG 200 iter	11.7 (12.8)	9.4 (16.1)	22.0 (43.1)	39.9 (51.8)	53.6 (58.0)
ADLG 500 iter	11.0 (13.6)	10.1 (16.4)	26.1 (47.1)	36.0 (55.0)	53.3 (57.8)
ADLG 1000 iter	**8.9** (10.3)	**6.4** (10.2)	23.2 (44.8)	35.8 (59.4)	**50.8** (59.7)
Median 9x9	13.6 (16.5)	12.7 (23.0)	22.9 (44.8)	33.2 (48.8)	54.3 (57.9)

Table 3.10: Region growing segmentation (lesions) - Validation metrics (average and standard deviation) for parameters choice using Average Distance (AD)

Figure 3.23, below, indicates small differences between pre-processing variations. This method seems to grow as expected so segment the region of interest that varies with the pre-processing method. It is noticeable that Figure 3.23a reveals a more detailed contour and with an increase in the pre-processing iterations of ADLG these details diminish.

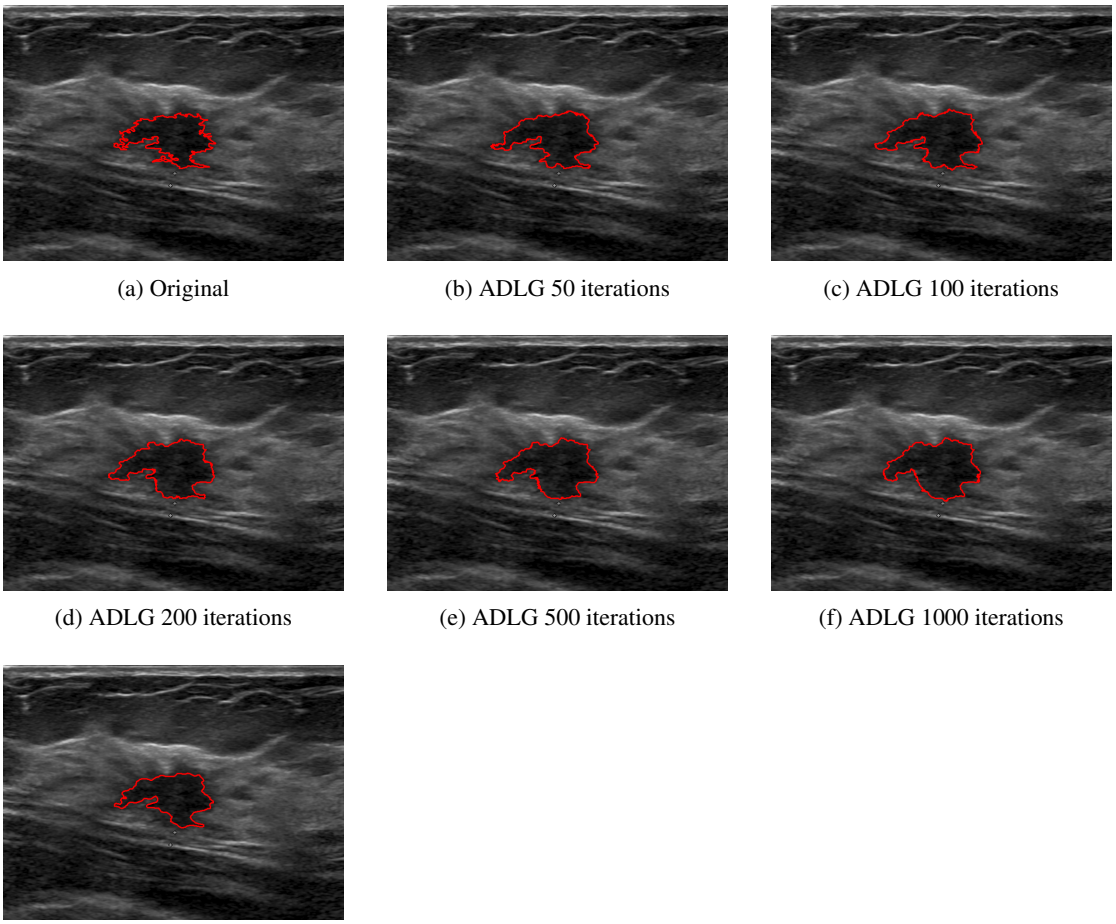

(a) Original (b) ADLG 50 iterations (c) ADLG 100 iterations

(d) ADLG 200 iterations (e) ADLG 500 iterations (f) ADLG 1000 iterations

(g) Median 9x9 filter

Figure 3.23: Region growing variation with pre-processing ($Threshold = 10\%$)

On the other hand, Figure 3.24 suggests substantial differences with different aggregation criterion threshold values. Figure 3.24a reveals under-segmentation which can be explained by the echogenicity of the lesion and since the threshold only allows the aggregation of values 2% (of the image's range) under or above the intensity of the seeds, values even slightly under or above this threshold will not be aggregated and, thus, this visual result.

For higher values of threshold this method grows more easily to shapes closer to those desired. Still, for values from a certain value for threshold, the segmented region outgrows the desired result, as seen in Figure 3.24d, and in a more extreme case segments other structures, as depicted in Figure 3.24e.

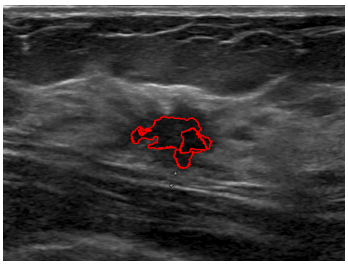

(a) $Threshold = 2\%$

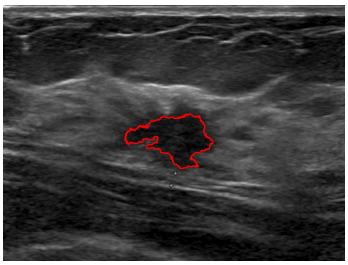

(b) $Threshold = 5\%$

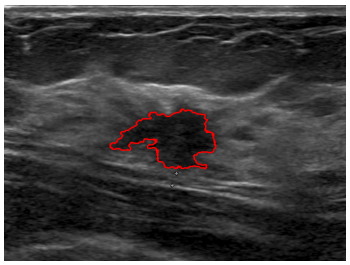

(c) $Threshold = 10\%$

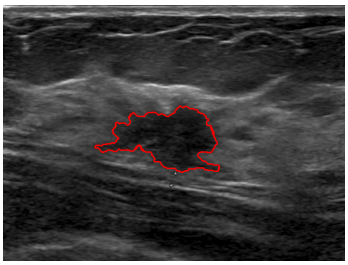

(d) $Threshold = 15\%$

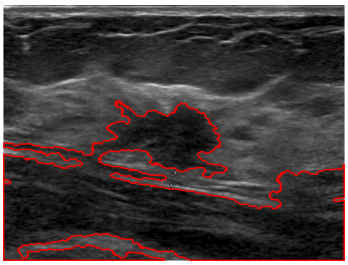

(e) $Threshold = 20\%$

Figure 3.24: Region growing variation with aggregation criterion threshold (ADLG with 200 iterations)

As illustrated in Table 3.9, the best results come from images pre-processed with ADLG filter with 200 iterations. It is worth noting that ADLG filter with 500 iterations produces comparable results to the ones with 200 iterations. Nonetheless, the first has a slower computation speed compared to the second which further suggests the use of the latter in the complete dataset.

3.6.2.3 Polar Minimum Path

This method uses an algorithm created by the supervisor of this dissertation, Professor Doctor Hélder Filipe Pinto de Oliveira [49] which consists in obtaining the accurate contour of an object using a closed shortest path algorithm.

This version has the particularity of being retricted considering it only moves forward or in the forward diagonal (8-connected), from margin to margin, turning the image into a graph. The way it works is that the lesion boundary can be seen as a change in the grey-level values of the pixels, originating an edge in the resulting image. Since the lesion contour is approximately circular the computation is more naturally carried out by adopting polar coordinates, with the origin of the coordinates in the ground truth's centroid.

Because this algorithm has been extensively used in the Visual Computing and Machine Intelligence (VCMI) group of INESC TEC, the parameters are already optimized and, therefore, this algorithm was used with the standard parameters only.

The results for the validation set are displayed below in Tables 3.11 and 3.12 and show that SD is the highest for ADLG with 1000 iterations, and AD is the lowest for ADLG with 500 iterations.

Original	ADLG 50 iter	ADLG 100 iter	ADLG 200 iter	ADLG 500 iter	ADLG 1000 iter	Median 9x9 kernel
0.43 (0.27)	0.48 (0.28)	0.53 (0.29)	0.59 (0.27)	0.70 (0.23)	**0.71** (0.24)	0.47 (0.26)

Table 3.11: Polar Minimum Path (lesions) - Validation metrics (average and standard deviation) for parameters choice using Sørensen–Dice coefficient (SD)

Original	ADLG 50 iter	ADLG 100 iter	ADLG 200 iter	ADLG 500 iter	ADLG 1000 iter	Median 9x9 kernel
15.2 (18.8)	12.9 (19.4)	11.5 (18.1)	8.0 (13.9)	**4.0** (7.1)	4.1 (7.0)	14.2 (20.4)

Table 3.12: Polar Minimum Path (lesions) - Validation metrics (average and standard deviation) for parameters choice using Average Distance (AD)

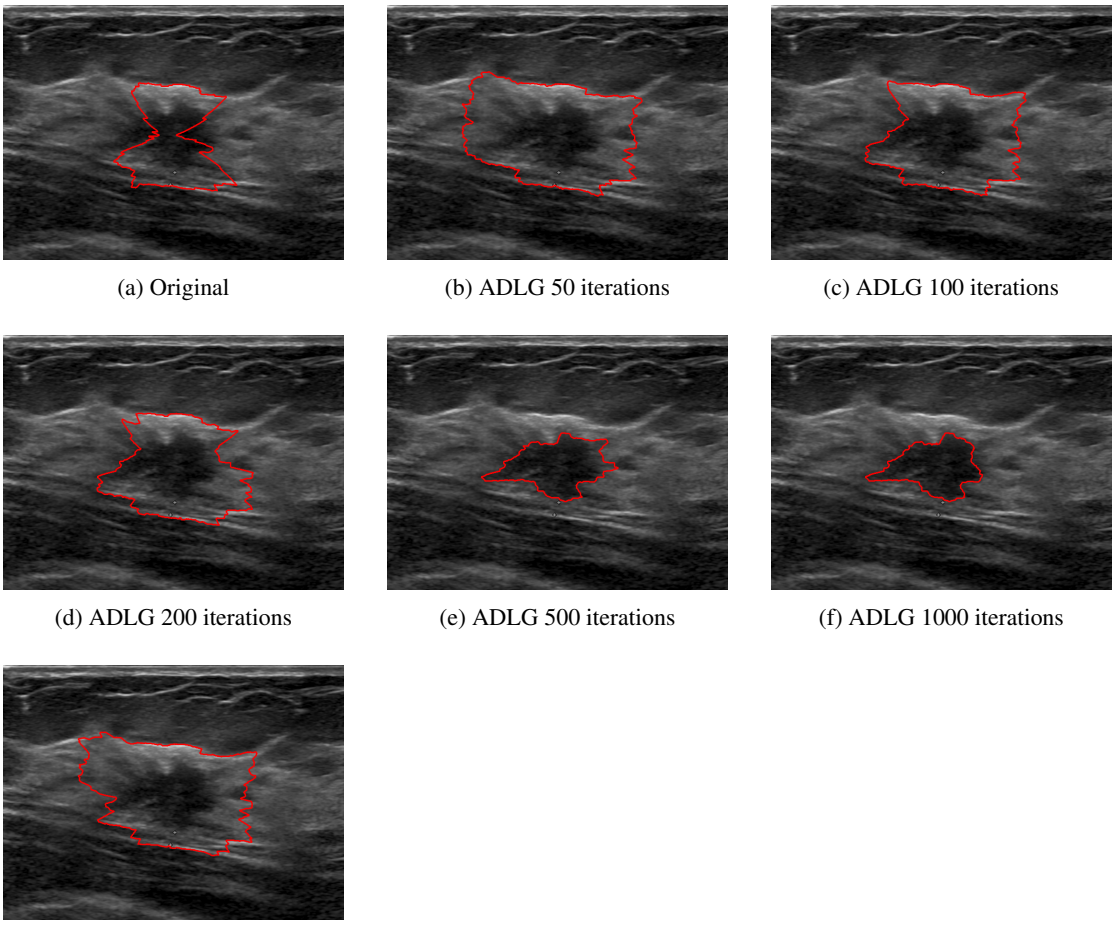

(a) Original (b) ADLG 50 iterations (c) ADLG 100 iterations

(d) ADLG 200 iterations (e) ADLG 500 iterations (f) ADLG 1000 iterations

(g) Median 9x9 filter

Figure 3.25: Polar minimum path variation with pre-processing

Figure 3.25 suggests an increase in performance of this method as the speckle noise reduction increases. As seen in Figure 3.25a, the lesion is poorly segmented which is related to the small variations of intensity present in the image. But, as this variations are smoothed out, by the pre-processing filters, the quality of the segmentation increases.

The best results, as shown in Table 3.11 result from the image pre-processed with ADLG filter with 1000 iterations.

3.6.3 Pipeline #3

3.6.3.1 K-means clustering

This method is essentially the same as the one in Section 3.6.1. However this time the goal is, not to segment a lesion, but to perform segmentation over the anatomical structures present in the image. Therefore, after performing K-means clustering, a Minimum Path algorithm created by Supervisor Hélder Filipe Pinto de Oliveira [49] is used to find the shortest paths from one margin to the other of the image.

In order to assess the best parameters to use, a grid search approach was adopted. Below are the parameters tested:

- **Input image:** Original, ADLG filtered (50, 100, 200, 500, 1000 iterations), Median filtered with 9×9 kernel
- **H-max suppression:** 0%, 20%, 40% of image's intensity range
- **Number of clusters:** K = 2, 3, 4, 5, 6

The results for the validation set are displayed below in Tables 3.13 and 3.14 and show that SD is the highest for ADLG with 50 iterations, $K = 6$ and H-max = 20%, and AD is the lowest for the original image, $K = 2$ and H-max = 0%.

	H-max	$K = 2$	$K = 3$	$K = 4$	$K = 5$	$K = 6$
Original	0%	**0.62** (0.20)	0.52 (0.24)	0.45 (0.20)	**0.59** (0.18)	0.47 (0.16)
	20%	0.56 (0.19)	0.54 (0.26)	0.53 (0.18)	0.50 (0.20)	0.59 (0.22)
	40%	0.56 (0.20)	0.53 (0.24)	**0.56** (0.17)	0.54 (0.23)	0.54 (0.20)
ADLG 50 iter	0%	0.57 (0.16)	0.54 (0.22)	0.51 (0.19)	0.55 (0.15)	0.57 (0.18)
	20%	0.58 (0.16)	0.58 (0.22)	0.54 (0.18)	0.57 (0.21)	**0.63** (0.18)
	40%	0.54 (0.21)	0.58 (0.23)	0.54 (0.21)	0.55 (0.19)	0.56 (0.22)
ADLG 100 iter	0%	0.60 (0.18)	0.51 (0.24)	0.51 (0.18)	0.52 (0.21)	0.51 (0.19)
	20%	0.54 (0.20)	0.52 (0.24)	0.55 (0.17)	0.49 (0.19)	0.53 (0.15)
	40%	0.59 (0.20)	0.56 (0.22)	0.47 (0.19)	0.55 (0.21)	0.54 (0.18)
ADLG 200 iter	0%	0.59 (0.17)	0.47 (0.24)	0.45 (0.21)	0.54 (0.22)	0.58 (0.17)
	20%	0.42 (0.25)	0.46 (0.24)	0.50 (0.23)	0.44 (0.19)	0.46 (0.22)
	40%	0.55 (0.20)	0.51 (0.23)	0.51 (0.19)	0.58 (0.18)	0.54 (0.17)
ADLG 500 iter	0%	0.42 (0.26)	0.39 (0.23)	0.44 (0.25)	0.43 (0.21)	0.37 (0.21)
	20%	0.56 (0.19)	0.56 (0.19)	0.53 (0.19)	0.50 (0.20)	0.56 (0.18)
	40%	0.37 (0.27)	0.38 (0.23)	0.45 (0.22)	0.51 (0.20)	0.43 (0.24)
ADLG 1000 iter	0%	0.54 (0.21)	**0.62** (0.19)	0.53 (0.20)	0.54 (0.22)	0.56 (0.22)
	20%	0.32 (0.24)	0.37 (0.27)	0.37 (0.25)	0.43 (0.24)	0.36 (0.22)
	40%	0.51 (0.24)	0.55 (0.24)	0.46 (0.23)	0.52 (0.20)	0.49 (0.21)
Median 9x9	0%	0.29 (0.24)	0.38 (0.23)	0.42 (0.27)	0.35 (0.21)	0.39 (0.23)
	20%	0.60 (0.18)	0.56 (0.23)	0.52 (0.19)	0.50 (0.19)	0.57 (0.20)
	40%	0.42 (0.25)	0.48 (0.22)	0.47 (0.19)	0.44 (0.18)	0.45 (0.21)

Table 3.13: K-means clustering (anatomical structures) - Validation metrics (average and standard deviation) for parameters choice using Sørensen–Dice coefficient (SD)

	H-max	$K = 2$	$K = 3$	$K = 4$	$K = 5$	$K = 6$
Original	0%	**10.2** (12.5)	19.2 (15.5)	24.0 (22.3)	14.4 (13.2)	20.0 (18.4)
	20%	16.3 (14.4)	17.8 (20.6)	16.0 (14.3)	18.5 (13.7)	11.1 (12.2)
	40%	15.5 (14.6)	19.0 (19.8)	15.5 (15.0)	16.3 (18.4)	19.5 (20.5)
ADLG 50 iter	0%	16.6 (13.1)	15.1 (17.1)	18.5 (14.1)	14.5 (14.6)	**10.7** (10.3)
	20%	14.1 (11.0)	14.9 (15.6)	19.9 (18.4)	14.5 (18.0)	14.4 (19.5)
	40%	17.2 (14.7)	13.7 (16.2)	17.0 (17.0)	15.8 (14.0)	15.8 (18.2)
ADLG 100 iter	0%	12.7 (14.0)	17.4 (15.7)	19.7 (16.0)	18.2 (15.0)	20.7 (19.5)
	20%	16.0 (14.3)	18.3 (20.2)	**13.4** (10.5)	20.8 (20.9)	16.7 (12.7)
	40%	10.7 (12.1)	16.1 (19.5)	21.7 (16.3)	13.5 (13.6)	14.0 (16.6)
ADLG 200 iter	0%	14.4 (13.2)	20.6 (21.1)	25.3 (17.7)	17.2 (17.7)	11.2 (12.7)
	20%	24.8 (16.0)	24.3 (21.1)	19.0 (19.4)	24.8 (19.6)	23.7 (19.7)
	40%	16.6 (13.9)	20.1 (18.7)	17.4 (15.1)	14.7 (18.7)	14.9 (14.3)
ADLG 500 iter	0%	27.1 (24.3)	26.8 (15.7)	24.8 (20.0)	22.8 (17.3)	28.4 (20.4)
	20%	16.8 (14.5)	14.9 (15.3)	18.7 (15.1)	20.0 (18.8)	14.5 (14.6)
	40%	29.3 (25.1)	29.3 (19.5)	28.1 (27.5)	20.9 (18.8)	29.1 (25.9)
ADLG 1000 iter	0%	17.1 (17.3)	**11.8** (13.8)	18.5 (16.5)	13.5 (15.0)	15.4 (17.1)
	20%	37.9 (25.9)	31.6 (24.4)	34.6 (30.4)	25.3 (24.7)	35.7 (26.5)
	40%	17.9 (17.1)	17.7 (20.1)	21.9 (17.7)	18.2 (20.4)	23.1 (18.1)
Median 9x9	0%	39.3 (24.6)	31.8 (23.8)	24.9 (22.3)	34.3 (23.9)	29.9 (20.7)
	20%	14.6 (15.2)	14.7 (16.0)	17.5 (13.1)	21.9 (20.6)	13.3 (14.2)
	40%	30.1 (20.7)	21.2 (20.0)	21.0 (17.2)	23.2 (20.4)	25.5 (21.2)

Column $K = 5$ has several minima. However, none of them is the minimum value of the table.

Therefore, no value in that column is shown in bold formatting

Table 3.14: K-means clustering (anatomical structures) - Validation metrics (average and standard deviation) for parameters choice using Average Distance (AD)

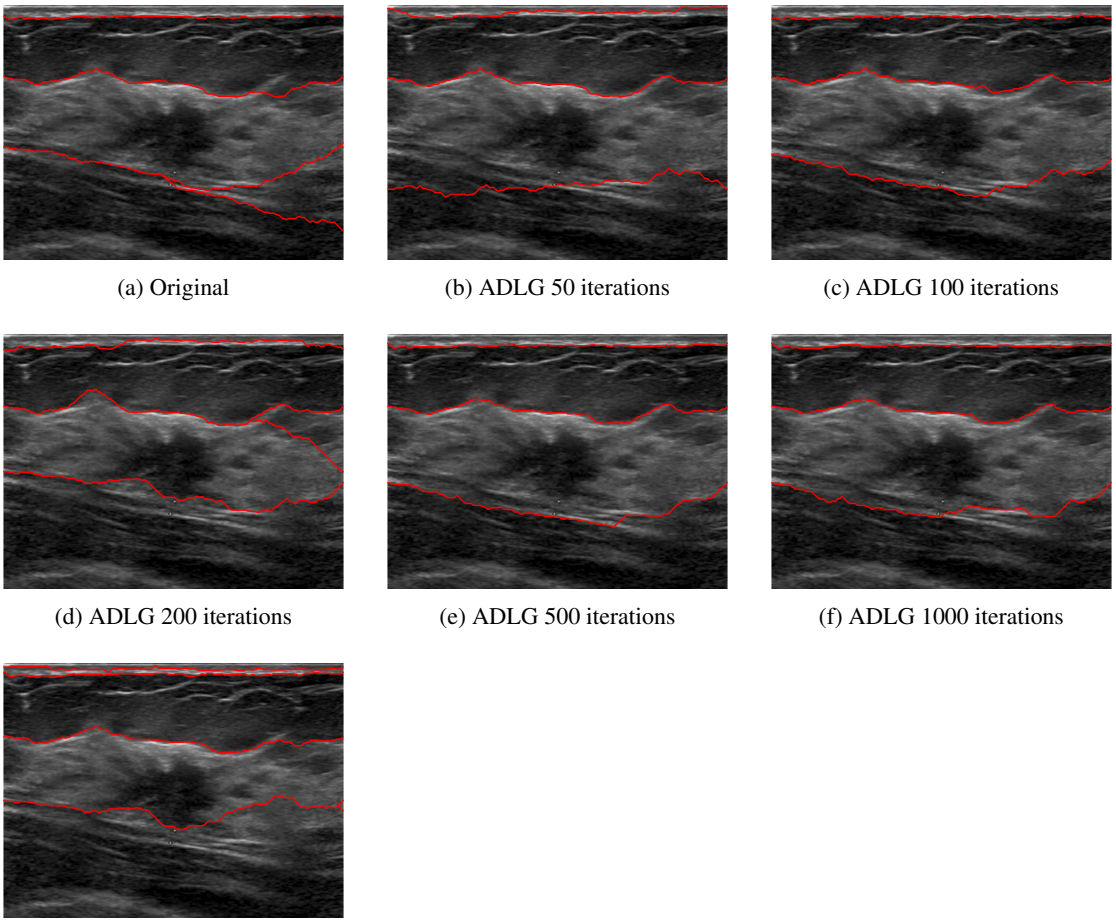

(a) Original (b) ADLG 50 iterations (c) ADLG 100 iterations

(d) ADLG 200 iterations (e) ADLG 500 iterations (f) ADLG 1000 iterations

(g) Median 9x9 filter

Figure 3.26: K-means variation with pre-processing ($K = 6$ and H-max = 20%)

As seen in Figure 3.26 the resulting margin-to-margin segmentation slightly varies with the pre-processing method used, although some differences can be attributed to the speckle noise reduction. For example in Figure 3.26a the method does not detect the heterogeneous area in the upper right corner of the mammary gland which is detected using pre-processing methods.

On the other hand, this smoothing can also affect large contiguous areas with similar echogenicity in the original image that end up undetected. This can be seen in ADLG pre-processed versions in the right lower bound of the segmentation where the method misses out an area of the mammary gland with less intensity which is detected in the original image.

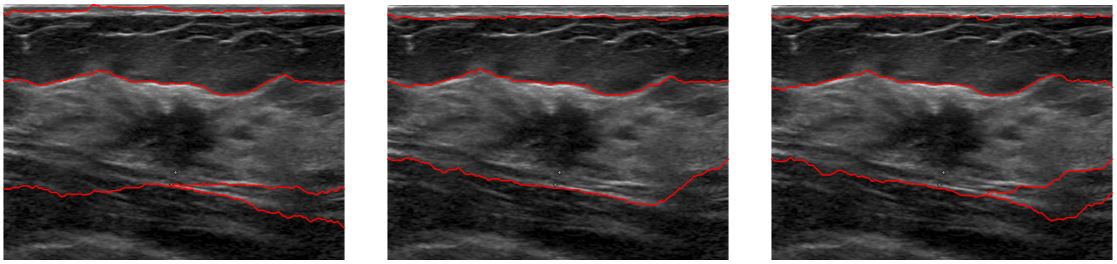

(a) H-max = 0% (b) H-max = 20% (c) H-max = 40%

Figure 3.27: K-means variation with H-max (ADLG with 50 iterations and $K = 6$)

Figure 3.27 indicates that the variation in the value of H-maxima Transform induces somewhat different results. The absence of this suppression not only leads the path to pass through small maxima along the way that may not be part of the region of interest, as depicted in the lower left bound of the mammary gland in Figure 3.27a but also to go through regions of high gradient within the region of interest that are not boundaries, as seen in the path along the skin of the same figure.

The use of higher values for H-max might also under-segment areas that have lower gradient transitions to other structures, although that is not the case in any of the figures displayed.

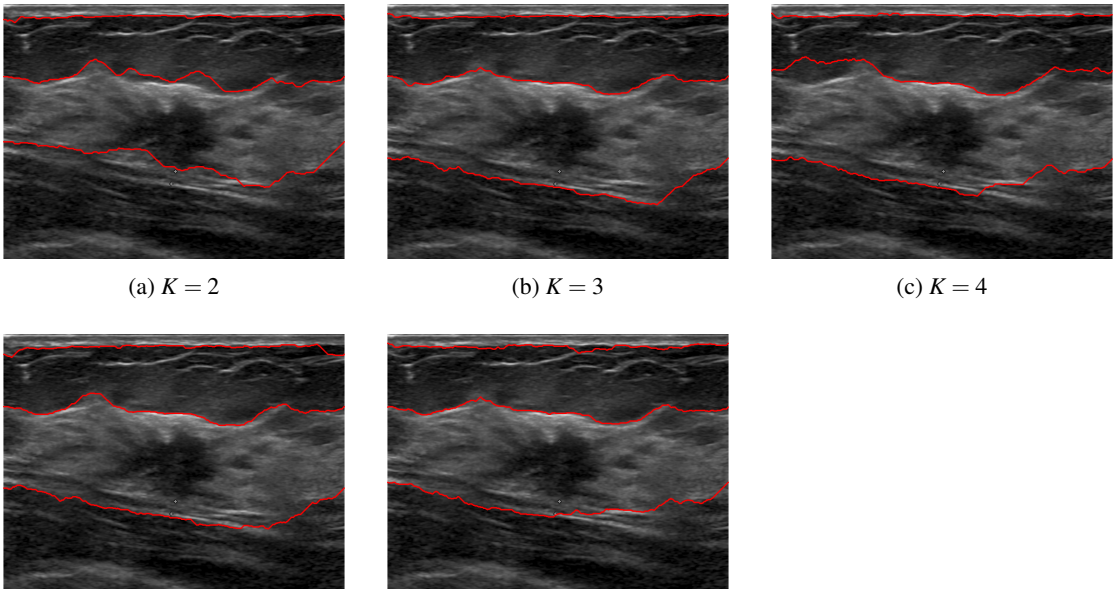

(a) $K = 2$ (b) $K = 3$ (c) $K = 4$

(d) $K = 5$ (e) $K = 6$

Figure 3.28: K-means variation with number of clusters (ADLG with 50 iterations and H-max = 20%)

Figure 3.28 also suggests small variations with the number of clusters with some areas being falsely detected with a small number of clusters, as seen in in the upper bound of the mammary gland in Figure 3.28a and some areas wrongly undetected due to a higher number of clusters, as

depicted in the right lower bound of the mammary gland for $K = 6$ Figure 3.28e compared to $K = 3$ in Figure 3.28b.

The best results, as stated above, resulted from pre-processing the image with the ADLG filter using 50 iterations, $K = 6$ clusters and with a 20% H-max suppression.

3.6.3.2 Mean shift clustering

This method performs Mean shift clustering using the cluster centroid locations from K-means as initial seeds to segment the anatomical structures in the ultrasound image. The parameters used for K-means result from Section 3.6.3.1 experiments and they are $K = 6$ clusters, $H - max = 20\%$ and on the median filtered by a ADLG filter using 50 iterations.

The implementation uses a Mean shift clustering algorithm adaptation of [24] by Co-supervisor João Pedro Fonseca Teixeira which has several parameters apart from the initial seeds such as bandwidth and X,Y position weights relative to image.

However this time the goal is, not to segment a lesion, but to perform segmentation over the anatomical structures present in the image. Therefore, after performing Mean shift clustering, a Minimum Path algorithm created by Supervisor Hélder Filipe Pinto de Oliveira [49] is used to find the shortest paths from one margin to the other of the image.

A grid search was used to test the several parameters:

- **Input image:** Original, ADLG filtered (50, 100, 200, 500, 1000 iterations), Median filtered with 9×9 kernel
- **Bandwidth:** 0.02, 0.05, 0.1
- **Position weights:** 0.0625, 0.125, 0.25 and 1

The complete results for the validation set are present in Appendix A.3. Because of the high number of results for this experiment, only the 8 best combinations for SD and the 2 worst are shown below in Tables 3.15 and 3.16. Due to time constraints, only SD is shown for this method.

Best parameters				
	ADLG 500 iter Bandwidth = 0.1 Weight = 0.125	ADLG 500 iter Bandwidth = 0.1 Weight = 0.0625	Median 9x9 Bandwidth = 0.02 Weight = 0.25	ADLG 500 iter Bandwidth = 0.05 Weight = 0.25
SD	**0.64** (0.16)	0.62 (0.14)	0.62 (0.18)	0.62 (0.21)
	ADLG 200 iter Bandwidth = 0.02 Weight = 0.125	ADLG 200 iter Bandwidth = 0.02 Weight = 1	ADLG 500 iter Bandwidth = 0.02 Weight = 1	ADLG 50 iter Bandwidth = 0.02 Weight = 0.25
SD	0.61 (0.16)	0.60 (0.18)	0.60 (0.20)	0.59 (0.14)
Best parameters				
	Median 9x9 Bandwidth = 0.02 Weight = 0.25	ADLG 500 iter Bandwidth = 0.02 Weight = 1	ADLG 200 iter Bandwidth = 0.05 Weight = 1	ADLG 200 iter Bandwidth = 0.02 Weight = 0.125
AD	**10.8** (12.4)	10.8 (11.4)	11.3 (11.0)	12.3 (14.7)
	ADLG 500 iter Bandwidth = 0.1 Weight = 0.125	ADLG 50 iter Bandwidth = 0.02 Weight = 0.25	ADLG 500 iter Bandwidth = 0.05 Weight = 1	ADLG 100 iter Bandwidth = 0.02 Weight = 0.0625
AD	12.9 (13.4)	12.9 (10.9)	13.0 (10.9)	13.7 (16.4)

Table 3.15: Mean shift clustering (anatomical structures) - Best validation metrics combination (average and standard deviation) for parameters choice using Sørensen–Dice coefficient (SD) and Average Distance (AD)

Worst parameters		
	Original Bandwidth = 0.1 Weight = 0.0625	Original Bandwidth = 0.1 Weight = 0.125
SD	**0.15** (0.27)	0.21 (0.27)
Worst parameters		
	Original Bandwidth = 0.1 Weight = 0.0625	Original Bandwidth = 0.1 Weight = 0.125
AD	**109.8** (50.3)	91.4 (54.0)

Table 3.16: Mean shift clustering (anatomical structures) - Worst validation metrics combination (average and standard deviation) for parameters choice using Sørensen–Dice coefficient (SD) and Average Distance (AD)

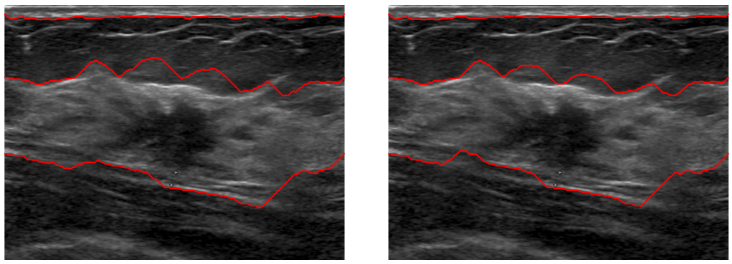

(a) ADLG 500 iterations (b) ADLG 1000 iterations

Figure 3.29: Mean shift variation with pre-processing ($Bandwidth = 0.1$ and $X,Yweights = 0.125$)[1]

The performance of Mean shift clustering increases with the number of iterations used for ADLG filter, as seen in Figures 3.29a and 3.29b. It is worth noting that Mean shift clustering has difficulty finding the shortest path in images pre-processed by ADLG with a low number of iterations as well as with the Median 9x9 filter, as expressed in Footnote 1.

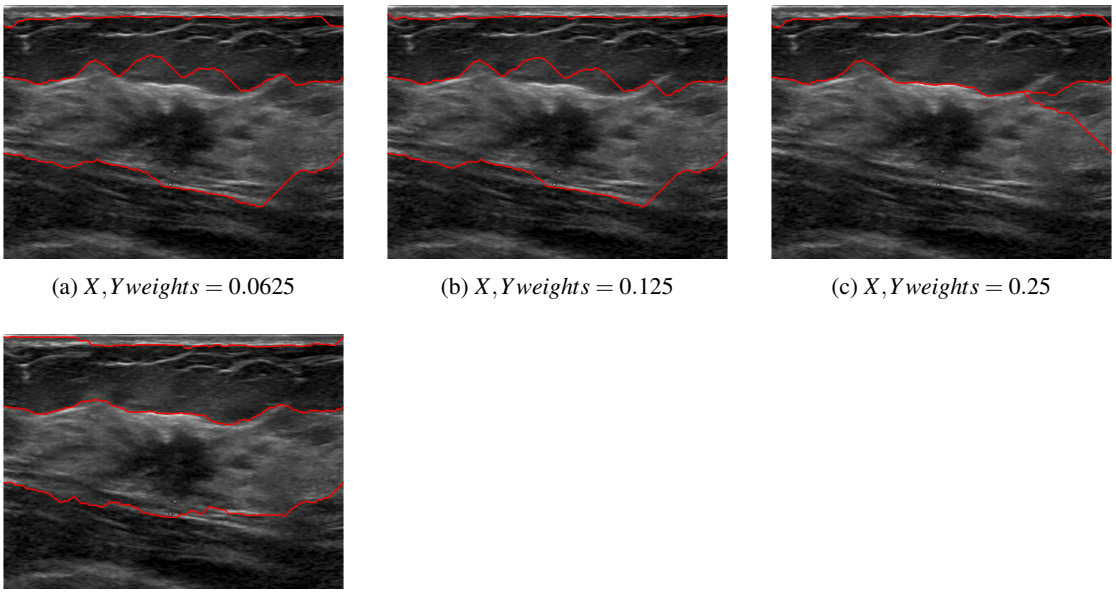

(a) $X,Yweights = 0.0625$ (b) $X,Yweights = 0.125$ (c) $X,Yweights = 0.25$

(d) $X,Yweights = 1$

Figure 3.30: Mean shift variation with $X,Yweights$ (ADLG with 500 iterations and $Bandwidth = 0.1$)

Figure 3.30 suggests that lower weights for positions X,Y improve the quality of the results. In Figures 3.30a and 3.30b all three structures, skin, subcutaneous fat and mammary gland, and consequently, thoracic region, are reasonably segmented. With higher values, however, the segmentation quality decays as illustrated in Figure 3.30c, in which not all structures are segmented.

[1]The results for Original image, ADLG with 50, 100 and 200 iterations and Median filtered 9x9 are not displayed in Figure 3.29 because this method could not find the shortest paths for these variations of pre-processing.

In Figure 3.30d, although the upper and lower boundaries of the mammary gland are visually close to the ground truth for this image in particular, the results for other images were not as satisfactory and it should also be pointed out that in the figure in question, the skin is also poorly segmented compared to the other variants.

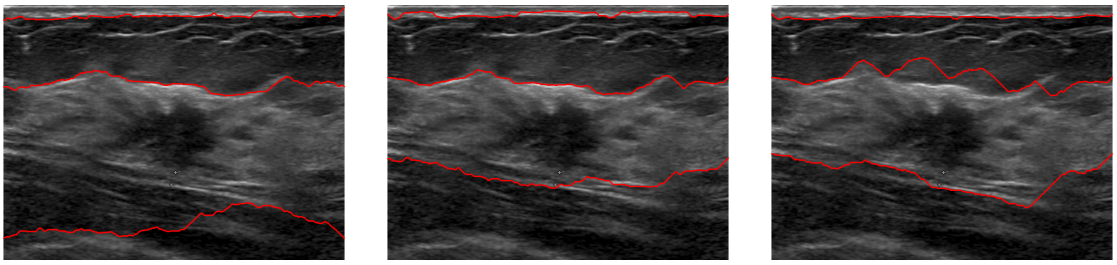

(a) $Bandwidth = 0.02$ (b) $Bandwidth = 0.05$ (c) $Bandwidth = 0.1$

Figure 3.31: Mean shift variation with bandwidth (ADLG with 500 iterations and $X,Yweights = 0.125$)

Finally, Figure 3.31 shows that lower values of bandwidth might be useful to detect other structures as depicted in the lower red line of Figure 3.31a which roughly detects portions of what seems to be the rib. Figure 3.31b and Figure 3.31c show that for higher values of bandwidth this method reasonably segments the expected structures assessed.

The best results, as shown above in Table 3.15, were for ADLG with 500 iterations, Bandwidth = 0.1, and X,Y Weight = 0.125.

3.6.3.3 Watershed

As with all the methods in this pipeline this method is essentially the same as the respective one in Section 3.6.1. However this time the goal is, not to segment a lesion, but to perform segmentation over the anatomical structures present in the image.

Therefore, because we want to detect transitions from brighter to darker areas, Watershed segmentation was performed on the complementary of the image and followed, again, by a Minimum Path algorithm created by Supervisor Hélder Filipe Pinto de Oliveira [49] is used to find the shortest paths from one margin to the other of the image.

A grid search was used to test several parameters:

- **Input image:** Original, ADLG filtered (50, 100, 200, 500, 1000 iterations), Median filtered with 9×9 kernel (As stated above, the complementary of these images was used)
- **H-min suppression:** 0%, 5%, 10%, 20% of image's intensity range

The results for the validation set are displayed below in Tables 3.17 and 3.18 and show that SD is the highest for original image with H-min = 0%, and AD is the lowest for ADLG with 50 iterations and H-min = 10%.

	H-min			
	0%	5%	10%	20%
Original	**0.47** (0.18)	0.32 (0.14)	0.31 (0.16)	0.33 (0.16)
ADLG 50 iter	0.30 (0.17)	0.28 (0.17)	**0.42** (0.18)	**0.42** (0.24)
ADLG 100 iter	0.38 (0.24)	0.23 (0.25)	0.32 (0.20)	0.28 (0.24)
ADLG 200 iter	0.09 (0.07)	**0.36** (0.21)	0.31 (0.25)	0.09 (0.06)
ADLG 500 iter	0.34 (0.21)	0.18 (0.18)	0.09 (0.05)	0.21 (0.17)
ADLG 1000 iter	0.17 (0.21)	0.11 (0.14)	0.15 (0.18)	0.12 (0.15)
Median 9x9	0.11 (0.13)	0.34 (0.18)	0.27 (0.23)	0.09 (0.08)

Table 3.17: Watershed segmentation (anatomical structures) - Validation metrics (average and standard deviation) for parameters choice using Sørensen–Dice coefficient (SD)

	H-min			
	0%	5%	10%	20%
Original	**21.9** (15.0)	24.9 (11.3)	27.5 (16.6)	28.3 (18.2)
ADLG 50 iter	31.4 (18.2)	36.1 (18.6)	**21.5** (12.5)	**24.1** (22.3)
ADLG 100 iter	27.0 (20.0)	50.5 (40.3)	26.2 (16.9)	29.7 (22.5)
ADLG 200 iter	59.7 (23.6)	26.1 (20.8)	30.8 (25.2)	60.1 (23.3)
ADLG 500 iter	27.3 (20.5)	50.0 (33.5)	60.7 (28.8)	44.1 (26.2)
ADLG 1000 iter	54.0 (33.7)	61.5 (30.8)	57.1 (34.2)	59.6 (23.0)
Median 9x9	58.3 (27.2)	**24.2** (16.9)	33.1 (25.9)	58.1 (25.9)

Table 3.18: Watershed segmentation (anatomical structures) - Validation metrics (average and standard deviation) for parameters choice using Average Distance (AD)

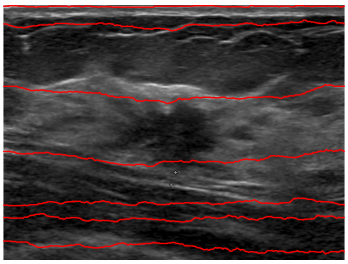

(a) Original

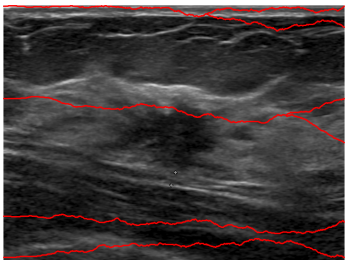

(b) ADLG 50 iterations

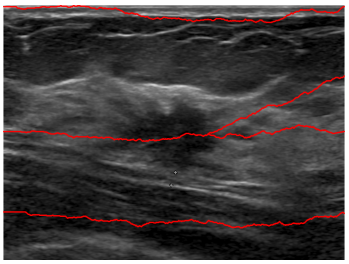

(c) ADLG 100 iterations

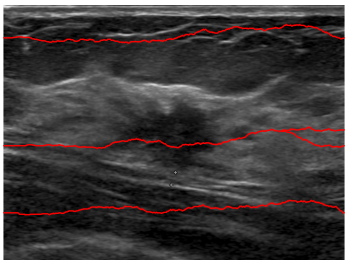

(d) ADLG 200 iterations

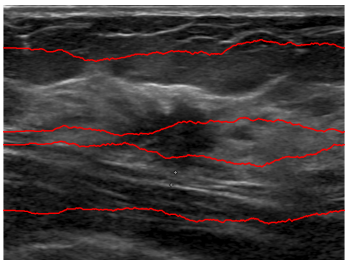

(e) ADLG 500 iterations

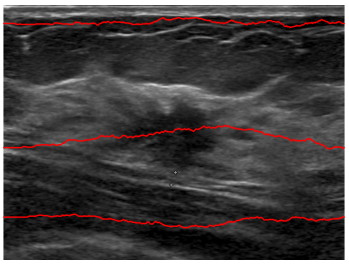

(f) ADLG 1000 iterations

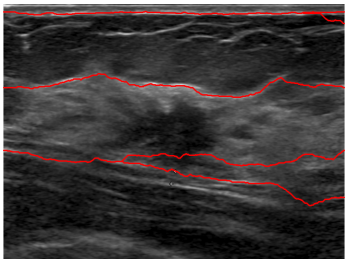

(g) Median 9x9 filter

Figure 3.32: Watershed variation with pre-processing (H-min=0%)

Figure 3.32 shows that Watershed has difficulty finding anatomical structures. As seen in this figure, images pre-processed for speckle noise reduction lead to less structures to be found. This can be explained since over-segmentation occurs because every regional minimum, even if tiny and insignificant, forms its own catchment basin. One solution is to modify the image to remove minima that are too shallow using the H-minima Transform.

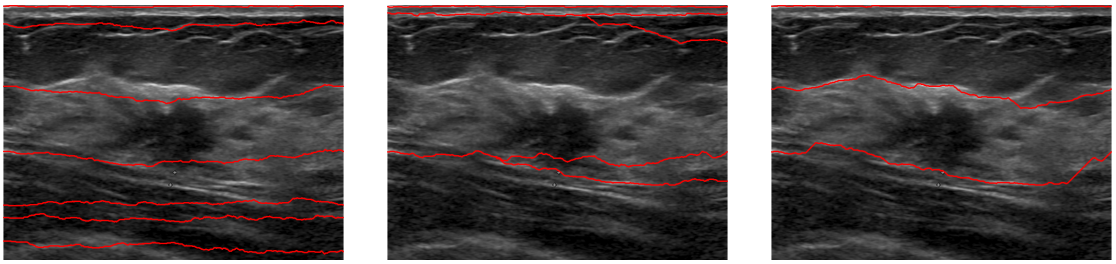

(a) H-min = 0% (b) H-min = 5% (c) H-min = 10%

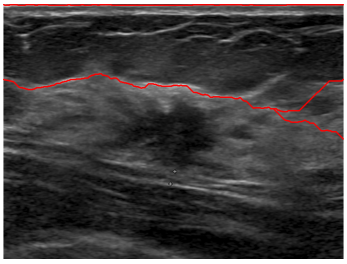

(d) H-min = 20%

Figure 3.33: Watershed variation with H-min (Original image)

Figure 3.33 tries to illustrate exactly this, with the number of margin-to-margin segmentation lines decreasing with an increase in minima suppression. Although this is not apparent in the figures displayed, the best results were found for the original image with a 0% minima suppression (no suppression).

3.7 Breast ultrasound segmentation

After an extensive experimentation with the several parameters on the validation set, the best combinations for each method were applied to the full dataset. Tables 3.19 and 3.20 summarize the resulting metrics for every method tested.

	Pipeline #1			**Pipeline #2**		
	K-means clustering	Watershed segmentation	Mean shift clustering	Active Contour model	Region growing	Polar Minimum path
SD	0.57 (0.33)	0.60 (0.23)	0.55 (0.19)	**0.72** (0.19)	0.60 (0.28)	0.70 (0.26)
AD	12.1 (23.6)	6.3 (9.1)	7.6 (14.1)	**4.3** (6.4)	18.9 (33.8)	6.4 (17.3)

Table 3.19: Pipeline #1 and Pipeline #2 (lesions) - Full dataset metrics results (average and standard deviation) of the best parameter combination for each method using the Sørensen–Dice coefficient (SD) and the Average distance (AD)

		Skin	Subcutaneous Fat	Mammary Gland	Thoracic Region	Average
K-means clustering	SD	**0.61** (0.22)	0.49 (0.29)	**0.49** (0.32)	**0.71** (0.20)	**0.57** (0.28)
	AD	**3.1** (5.5)	17.4 (17.2)	**23.2** (24.8)	**13.1** (17.0)	**13.4** (18.3)
Mean shift clustering	SD	0.48 (0.27)	0.44 (0.29)	0.44 (0.32)	0.64 (0.22)	0.49 (0.28)
	AD	13.8 (24.5)	29.6 (34.2)	38.9 (54.3)	15.0 (13.3)	22.4 (32.0)
Watershed segmentation	SD	0.52 (0.25)	**0.51** (0.26)	0.32 (0.29)	0.66 (0.22)	0.50 (0.28)
	AD	3.4 (5.1)	**17.2** (20.9)	41.4 (37.0)	21.3 (20.3)	20.4 (27.1)

Table 3.20: Pipeline #3 (anatomical structures) - Full dataset metrics results (average and standard deviation) of the best parameter combination for each method using the Sørensen–Dice coefficient (SD) and the Average distance (AD)

For lesion segmentation, the results for the full dataset further confirm the results for the validation set. As seen in Table 3.19, Pipeline #2 methods outperform methods from Pipeline #1 which suggests that region-based and contour-based methods are better suited than clustering-based and watershed-based method for this type of segmentation. Moreover, as with the validation set, Active Contour model is the most successful in lesion segmentation.

On one hand, on K-means, K is chosen manually, and because ultrasounds have low resolution and a good amount of speckle noise , the optimal K often varies from image to image. On the other hand, clustering-based methods are very dependent on initial values and is very difficult to pick the values of the initial centroids. Furthermore, centroids can be dragged by outliers, or outliers might get their own cluster instead of being ignored. In the case of Watershed segmentation, this method usually results in over-segmentation due to its noise sensitivity. One solution to this is to use markers and start flooding from those specific seed points. The fact that lesions may have a homogeneous nature, if they are benign, aids the results for Region growing in which pixels with similar properties are clustered together to form a homogeneous region. Moreover, since lesion boundaries usually have strong edges this gives an advantage to deformable models, like Active contour model, which because of their dynamic and iterative nature can adapt to the shape of the object. Moreover, this property of having strong edges also helps Polar Minimum Path since this method uses the gradient of the image to find the shortest path. Therefore, it is expected for methods from Pipeline #2 to outperform those of Pipeline #1.

In the matters of anatomical structures segmentation, the results for the full dataset diverge from the validation set. As seen in Table 3.20, the average best performing method is still K-means clustering. However, Mean shift clustering, which had comparable results in the validation set, has an inferior performance for the full dataset. Additionally, for the full dataset each structure was evaluated individually as well. K-means clustering is the best performing method for skin, mammary gland and thoracic region segmentation but Watershed has better results for subcutaneous fat segmentation. Nevertheless, K-means clustering achieves similar results for this structure's segmentation.

As stated before, the very nature of Watershed segmentation is very sensitive to noise and, consequently, prone to over-segmentation which can lead to undesirable results and, thus, to unexpected paths from margin-to-margin. Furthermore, in the case of Mean shift clustering, this method has its initial seeds dependent on the results from K-means which means that errors in the latter method are propagated to the former. This might explain the reason this method falls behind K-means in the detection and segmentation of every structure. For these reasons, it is safe to presume K-means clustering results to exceed those of Mean shift clustering and Watershed segmentation for anatomical structures segmentation.

3.8 Summary

In this chapter, several of the segmentation approaches attempted were documented and the experimental results displayed.

The chapter started with a brief introduction of the dataset followed by a detailed description of the pipeline models used. Next, the reader was elucidated on the metrics used for results comparison, although only the Sørensen–Dice coefficient and the Average distance were effectively considered and shown for each method. After that, the pre-processing phase is elaborated and the steps to keep only the acquisition window were shown. Afterwards, the segmentation methods are laid out with the various parameters combinations tested and their respective results for the validation set, both visual and numeric, are shown.

Overall, the region-based and contour-based methods, present in Pipeline #2, were more successful for lesion segmentation compared to clustering-based and watershed-based methods, present in Pipeline #1. On the other hand, clustering-based methods performed better for anatomical structures segmentation than the watershed-based method. The most successful lesion segmentation method was the Active Contour model and the most successful anatomical structure segmentation method was K-means clustering but Mean shift clustering had comparable results as well.

Finally, the best combination of parameters for each method was tested on the full dataset with Pipeline #2 methods outperforming Pipeline #1 methods for lesion segmentation and Active Contour model, again, achieving the best results for this type of segmentation, which further corroborated the hypothesis. With respect to the anatomical structures, Pipeline #3, contrarily to the validation set, Mean shift clustering underperforms in the full dataset. However, K-means clustering was still the best overall segmentation method, having the best results for skin, mammary gland and thoracic region segmentation and Watershed segmentation had the best results for subcutaneous fat segmentation, although K-means clustering had very similar results for this structure.

Chapter 4

Conclusion and future work

This chapter summarizes the research performed throughout this dissertation, its main conclusions, and contributions. Lastly, we list some ideas to improve our work in the future.

4.1 Overview and contributions

Breast cancer is the predominant cause of cancer in women globally. In recent years, the mortality rate has been decreasing not only because of study of the primary causes related with this type of cancer, such as late first full-term pregnancy, late menopause, moderate alcohol intake, and genetics, but also because of the early detection, diagnosis, and treatment improvement of this malignancy. Since ultrasound imaging does not expose the patient to ionizing radiation, it represents a safer, easily accessible and affordable alternative to mammograms for breast cancer detection. Therefore, this medical imaging technique can be of the utmost usefulness for study, evaluation and development of different techniques for anatomical landmark segmentation of the different structures and lesions of the female breast.

Taking this into consideration, it is possible to allow a better communication between the physician and the patients and further empower them by developing a solution for automated segmentation of anatomical structures, such as skin, subcutaneous fat, mammary gland, and thoracic region. This dissertation explores six different methods for lesion segmentation - K-means clustering, Mean shift clustering, Watershed segmentation, Region growing, Active contour model (Snakes) and Polar minimum path; and three for anatomical structures segmentation - K-means clustering, Mean shift clustering and Watershed segmentation, all of them followed by a shortest path algorithm to connect one margin to the other.

Using Pixel-Area and Contour-wise metrics, the results are compared to manually delineated annotations by a professional physician. These results suggest a better lesion segmentation using countour-based and region-based methods in contrast to clustering-based and watershed-based methods. Furthermore, Active contour model (SD = 0.72, AD = 4.3) was the best performing method for this type of segmentation. In contrast, results reveal K-means clustering to be the most effective method for anatomical structures segmentation. Additionally, this method exceeds both

Watershed and Mean shift at skin (SD = 0.61, AD = 3.1), mammary gland (SD = 0.49, AD = 23.2) and thoracic region (SD = 0.71, AD = 13.1) segmentation. Watershed segmentation, however, outperforms the other two at subcutaneous fat (SD = 0.51, AD = 17.2) segmentation.

4.2 Future work

This dissertation shows that although we were able to perform segmentation of lesions and anatomical structures in breast ultrasound images there is still room for furtherance in this field. Below, we list some possible improvements that we propose to implement in the future.

- Development of **machine learning algorithms** for segmentation of structures. In this dissertation only classical methods were tested;
- Acquisition of **more and better annotations**. The annotations used in this dissertation were poorly detailed and the number of annotations for anatomical structures segmentation was very small;
- Develop an automated **detection algorithm** for lesions. Several tests were conducted throughout the development of this dissertation, namely using the Circular Hough Transform. The tests were successful for some lesions (benign). However, due to the nature of malignant lesions (heterogeneous echogenicity and irregular shape), automated detection could not be generalized and, thus, abandoned;
- Extend the **pre-processing study** with other methods;
- Explore **specific parameters for each anatomical structure segmentation**. The methods used were assessed for the overall segmentation of the structures and not for each specific structure.
- Explore other **evaluation metrics** to overcome some contradictions detected by the ones used for this research.

Appendix A

Appendix

A.1 Mean shift clustering (lesions)

	Bandwidth		
	0.02	0.05	0.1
Original	0.15 (0.16)	0.14 (0.16)	0.14 (0.17)
ADLG 50 iter	0.16 (0.13)	0.16 (0.17)	0.15 (0.20)
ADLG 100 iter	0.15 (0.12)	0.17 (0.16)	0.16 (0.20)
ADLG 200 iter	0.16 (0.11)	0.18 (0.17)	0.17 (0.20)
ADLG 500 iter	0.19 (0.14)	0.20 (0.17)	0.17 (0.20)
ADLG 1000 iter	**0.22** (0.14)	0.20 (0.17)	**0.20** (0.23)
Median 9x9	0.16 (0.16)	0.16 (0.17)	0.14 (0.17)

Column *Bandwidth* = 0.05 has several maxima.

However, none of them is the maximum value of the table.

Therefore, no value in that column is shown in bold formatting

Figure A.1: Mean shift segmentation (lesions) - Validation metrics (average and standard deviation) for parameters choice using Sørensen–Dice coefficient (SD) for X,Y position weight = 0.0625

	Bandwidth		
	0.02	0.05	0.1
Original	58.0 (55.5)	100.9 (60.8)	**106.0** (62.3)
ADLG 50 iter	45.2 (48.9)	94.0 (56.5)	111.1 (57.7)
ADLG 100 iter	51.4 (48.2)	92.4 (56.1)	111.1 (58.8)
ADLG 200 iter	50.5 (51.4)	92.6 (58.9)	111.7 (62.4)
ADLG 500 iter	45.0 (46.4)	**83.5** (54.4)	108.1 (61.4)
ADLG 1000 iter	**41.3** (44.9)	84.1 (57.4)	107.9 (63.5)
Median 9x9	48.3 (46.8)	96.3 (56.4)	109.4 (60.9)

Figure A.2: Mean shift segmentation (lesions) - Validation metrics (average and standard deviation) for parameters choice using Average Distance (AD) for X,Y position weight = 0.0625

	Bandwidth		
	0.02	0.05	0.1
Original	0.18 (0.16)	0.18 (0.18)	0.14 (0.17)
ADLG 50 iter	0.22 (0.14)	0.20 (0.18)	0.16 (0.20)
ADLG 100 iter	0.24 (0.14)	0.22 (0.19)	0.17 (0.20)
ADLG 200 iter	0.24 (0.15)	0.22 (0.17)	0.16 (0.21)
ADLG 500 iter	0.28 (0.18)	0.24 (0.19)	0.18 (0.22)
ADLG 1000 iter	**0.31** (0.21)	**0.25** (0.18)	**0.22** (0.23)
Median 9x9	0.20 (0.16)	0.19 (0.18)	0.14 (0.17)

Figure A.3: Mean shift segmentation (lesions) - Validation metrics (average and standard deviation) for parameters choice using Sørensen–Dice coefficient (SD) for X,Y position weight = 0.125

	Bandwidth		
	0.02	0.05	0.1
Original	18.7 (30.8)	71.3 (55.6)	106.1 (62.1)
ADLG 50 iter	11.0 (14.4)	62.6 (45.5)	107.1 (60.5)
ADLG 100 iter	**10.2** (13.3)	62.2 (47.1)	106.2 (60.2)
ADLG 200 iter	13.0 (19.2)	61.4 (49.0)	108.0 (62.5)
ADLG 500 iter	11.0 (13.1)	58.8 (50.6)	106.3 (61.4)
ADLG 1000 iter	11.6 (16.6)	**51.9** (47.1)	**99.0** (61.3)
Median 9x9	14.3 (16.8)	63.7 (48.4)	107.1 (59.5)

Figure A.4: Mean shift segmentation (lesions) - Validation metrics (average and standard deviation) for parameters choice using Average Distance (AD) for X,Y position weight = 0.125

	Bandwidth		
	0.02	0.05	0.1
Original	0.21 (0.18)	0.28 (0.22)	0.16 (0.18)
ADLG 50 iter	0.22 (0.16)	0.34 (0.22)	0.19 (0.21)
ADLG 100 iter	0.22 (0.17)	0.34 (0.21)	0.22 (0.23)
ADLG 200 iter	0.24 (0.18)	0.34 (0.22)	0.22 (0.22)
ADLG 500 iter	0.27 (0.21)	0.39 (0.21)	0.26 (0.25)
ADLG 1000 iter	**0.32** (0.24)	**0.42** (0.23)	**0.29** (0.26)
Median 9x9	0.22 (0.19)	0.30 (0.21)	0.19 (0.20)

Figure A.5: Mean shift segmentation (lesions) - Validation metrics (average and standard deviation) for parameters choice using Sørensen–Dice coefficient (SD) for X,Y position weight = 0.25

	Bandwidth		
	0.02	0.05	0.1
Original	**5.80** (7.2)	35.0 (47.6)	76.7 (52.5)
ADLG 50 iter	7.40 (10.1)	25.0 (35.2)	79.0 (58.0)
ADLG 100 iter	8.90 (11.1)	25.0 (38.6)	75.1 (58.1)
ADLG 200 iter	9.80 (13.3)	26.6 (38.8)	68.9 (54.2)
ADLG 500 iter	10.20 (12.1)	23.1 (35.0)	67.9 (54.3)
ADLG 1000 iter	9.90 (10.7)	**20.9** (31.9)	**66.1** (51.3)
Median 9x9	9.20 (10.9)	29.5 (37.6)	70.9 (51.0)

Figure A.6: Mean shift segmentation (lesions) - Validation metrics (average and standard deviation) for parameters choice using Average Distance (AD) for X,Y position weight = 0.25

	Bandwidth		
	0.02	0.05	0.1
Original	0.05 (0.08)	0.33 (0.25)	0.47 (0.25)
ADLG 50 iter	0.09 (0.10)	0.30 (0.23)	0.51 (0.24)
ADLG 100 iter	0.10 (0.11)	0.32 (0.24)	0.51 (0.22)
ADLG 200 iter	0.11 (0.11)	0.32 (0.23)	0.52 (0.22)
ADLG 500 iter	0.14 (0.15)	0.36 (0.25)	0.55 (0.21)
ADLG 1000 iter	0.14 (0.16)	**0.38** (0.24)	**0.57** (0.22)
Median 9x9	0.07 (0.09)	0.30 (0.23)	0.50 (0.23)

Column $Bandwidth = 0.02$ has several maxima.

However, none of them is the maximum value of the table.

Therefore, no value in that column is shown in bold formatting

Figure A.7: Mean shift segmentation (lesions) - Validation metrics (average and standard deviation) for parameters choice using Sørensen–Dice coefficient (SD) for X,Y position weight = 1

	Bandwidth		
	0.02	0.05	0.1
Original	26.0 (21.3)	**7.7** (9.6)	7.1 (10.7)
ADLG 50 iter	24.7 (19.7)	12.3 (13.6)	7.7 (10.6)
ADLG 100 iter	24.3 (20.5)	12.7 (15.3)	7.8 (12.1)
ADLG 200 iter	23.3 (19.1)	12.8 (14.5)	7.3 (9.2)
ADLG 500 iter	23.2 (19.4)	12.3 (12.8)	6.7 (8.5)
ADLG 1000 iter	**22.9** (19.7)	11.5 (10.9)	**6.6** (8.2)
Median 9x9	26.7 (21.0)	12.1 (12.4)	7.1 (8.3)

Figure A.8: Mean shift segmentation (lesions) - Validation metrics (average and standard deviation) for parameters choice using Average Distance (AD) for X,Y position weight = 1

A.2 Active Contour

	Iterations				
	50	100	200	500	1000
Original	0.33 (0.23)	0.55 (0.25)	0.66 (0.21)	0.67 (0.24)	0.65 (0.24)
ADLG 50 iter	0.38 (0.24)	0.59 (0.25)	0.69 (0.20)	0.68 (0.24)	0.65 (0.26)
ADLG 100 iter	0.38 (0.24)	0.60 (0.24)	0.69 (0.20)	0.68 (0.24)	0.65 (0.26)
ADLG 200 iter	0.39 (0.24)	0.60 (0.24)	0.69 (0.20)	0.69 (0.24)	0.65 (0.26)
ADLG 500 iter	0.40 (0.24)	0.60 (0.23)	0.69 (0.20)	0.69 (0.24)	0.65 (0.25)
ADLG 1000 iter	0.41 (0.24)	0.60 (0.23)	0.68 (0.21)	0.69 (0.24)	0.65 (0.26)
Median 9x9	0.38 (0.25)	0.60 (0.25)	0.69 (0.20)	0.67 (0.24)	0.63 (0.26)

Figure A.9: Active contour segmentation (lesions) - Validation metrics (average and standard deviation) for parameters choice using Sørensen–Dice coefficient (SD), SmoothFactor = 0, ContractionBias = 0

	Iterations				
	50	100	200	500	1000
Original	13.7 (15.1)	6.5 (9.8)	3.4 (6.2)	5.1 (10.2)	8.1 (16.1)
ADLG 50 iter	12.7 (15.1)	6.0 (8.8)	3.3 (5.3)	7.2 (14.3)	13.5 (25.9)
ADLG 100 iter	12.6 (15.0)	5.9 (8.7)	3.3 (5.0)	7.2 (14.2)	13.5 (26.0)
ADLG 200 iter	12.3 (14.8)	5.9 (8.7)	3.4 (5.0)	7.2 (14.3)	13.4 (25.9)
ADLG 500 iter	11.9 (14.8)	5.9 (9.0)	3.7 (5.2)	7.0 (14.0)	13.3 (25.7)
ADLG 1000 iter	11.6 (15.0)	5.7 (8.6)	3.9 (5.6)	6.8 (13.5)	12.2 (22.5)
Median 9x9	12.7 (15.0)	5.8 (8.6)	3.5 (5.4)	8.0 (14.7)	14.8 (27.8)

Figure A.10: Active contour segmentation (lesions) - Validation metrics (average and standard deviation) for parameters choice using Average Distance (AD), SmoothFactor = 0, ContractionBias = 0

	Iterations				
	50	100	200	500	1000
Original	0.33 (0.23)	0.55 (0.25)	0.66 (0.21)	0.67 (0.24)	0.65 (0.25)
ADLG 50 iter	0.37 (0.24)	0.59 (0.25)	0.69 (0.20)	0.68 (0.24)	0.65 (0.26)
ADLG 100 iter	0.38 (0.24)	0.59 (0.24)	0.69 (0.20)	0.69 (0.24)	0.65 (0.26)
ADLG 200 iter	0.38 (0.24)	0.59 (0.24)	0.69 (0.20)	0.69 (0.24)	0.65 (0.26)
ADLG 500 iter	0.39 (0.24)	0.59 (0.23)	0.69 (0.20)	0.69 (0.24)	0.65 (0.25)
ADLG 1000 iter	0.41 (0.24)	0.60 (0.23)	0.68 (0.21)	0.69 (0.24)	0.65 (0.26)
Median 9x9	0.38 (0.24)	0.60 (0.25)	0.69 (0.20)	0.67 (0.24)	0.63 (0.26)

Figure A.11: Active contour segmentation (lesions) - Validation metrics (average and standard deviation) for parameters choice using Sørensen–Dice coefficient (SD), SmoothFactor = 0.01, ContractionBias = 0

	Iterations				
	50	100	200	500	1000
Original	13.8 (15.1)	6.6 (9.8)	3.5 (6.3)	5.1 (9.9)	8.3 (16.4)
ADLG 50 iter	12.8 (15.2)	6.0 (8.9)	3.4 (5.2)	7.0 (14.1)	13.4 (25.6)
ADLG 100 iter	12.7 (15.1)	6.0 (8.8)	3.3 (4.9)	7.1 (14.0)	13.4 (25.9)
ADLG 200 iter	12.5 (14.9)	6.0 (8.9)	3.5 (5.0)	7.2 (14.2)	13.4 (25.8)
ADLG 500 iter	12.1 (14.9)	6.0 (9.1)	3.7 (5.1)	7.0 (13.9)	13.1 (25.3)
ADLG 1000 iter	11.7 (15.1)	5.8 (8.8)	3.9 (5.5)	6.7 (13.2)	12.1 (22.3)
Median 9x9	12.8 (15.1)	5.9 (8.7)	3.5 (5.3)	7.9 (14.6)	14.7 (27.6)

Figure A.12: Active contour segmentation (lesions) - Validation metrics (average and standard deviation) for parameters choice using Average Distance (AD), SmoothFactor = 0.01, ContractionBias = 0

	Iterations				
	50	100	200	500	1000
Original	0.31 (0.23)	0.53 (0.25)	0.66 (0.21)	0.68 (0.24)	0.66 (0.25)
ADLG 50 iter	0.37 (0.24)	0.58 (0.25)	0.69 (0.20)	0.69 (0.24)	0.65 (0.26)
ADLG 100 iter	0.37 (0.24)	0.59 (0.24)	0.69 (0.20)	0.69 (0.24)	0.65 (0.26)
ADLG 200 iter	0.37 (0.24)	0.59 (0.24)	0.69 (0.20)	0.69 (0.24)	0.65 (0.26)
ADLG 500 iter	0.38 (0.24)	0.59 (0.23)	0.68 (0.20)	0.69 (0.24)	0.66 (0.25)
ADLG 1000 iter	0.40 (0.24)	0.59 (0.23)	0.68 (0.21)	0.69 (0.24)	0.65 (0.26)
Median 9x9	0.37 (0.24)	0.59 (0.25)	0.68 (0.20)	0.67 (0.24)	0.64 (0.26)

Figure A.13: Active contour segmentation (lesions) - Validation metrics (average and standard deviation) for parameters choice using Sørensen–Dice coefficient (SD), SmoothFactor = 0.04, ContractionBias = 0

	Iterations				
	50	100	200	500	1000
Original	14.7 (15.7)	7.1 (10.2)	3.7 (6.5)	4.6 (9.1)	7.0 (14.4)
ADLG 50 iter	13.2 (15.5)	6.2 (9.1)	3.4 (5.2)	6.8 (13.7)	13.2 (25.3)
ADLG 100 iter	13.2 (15.3)	6.3 (9.1)	3.4 (5.0)	6.8 (13.6)	13.2 (25.3)
ADLG 200 iter	13.0 (15.2)	6.2 (9.2)	3.5 (5.0)	7.0 (13.9)	13.1 (25.2)
ADLG 500 iter	12.5 (15.2)	6.2 (9.4)	3.7 (5.1)	6.9 (13.7)	12.8 (24.6)
ADLG 1000 iter	12.2 (15.4)	6.0 (9.1)	4.0 (5.4)	6.6 (13.0)	11.7 (21.4)
Median 9x9	13.4 (15.3)	6.4 (9.1)	3.7 (5.5)	7.7 (14.4)	14.4 (27.1)

Figure A.14: Active contour segmentation (lesions) - Validation metrics (average and standard deviation) for parameters choice using Average Distance (AD), SmoothFactor = 0.04, ContractionBias = 0

	Iterations				
	50	100	200	500	1000
Original	0.29 (0.22)	0.50 (0.26)	0.64 (0.24)	0.67 (0.25)	0.66 (0.25)
ADLG 50 iter	0.34 (0.24)	0.55 (0.28)	0.66 (0.26)	0.65 (0.29)	0.62 (0.29)
ADLG 100 iter	0.35 (0.24)	0.56 (0.26)	0.66 (0.24)	0.66 (0.27)	0.63 (0.28)
ADLG 200 iter	0.35 (0.24)	0.55 (0.26)	0.66 (0.24)	0.67 (0.27)	0.63 (0.28)
ADLG 500 iter	0.36 (0.24)	0.57 (0.25)	0.67 (0.22)	0.68 (0.26)	0.65 (0.27)
ADLG 1000 iter	0.36 (0.25)	0.55 (0.26)	0.63 (0.26)	0.65 (0.29)	0.62 (0.29)
Median 9x9	0.34 (0.24)	0.56 (0.27)	0.67 (0.22)	0.66 (0.25)	0.62 (0.27)

Figure A.15: Active contour segmentation (lesions) - Validation metrics (average and standard deviation) for parameters choice using Sørensen–Dice coefficient (SD), SmoothFactor = 0.1, ContractionBias = 0

	Iterations				
	50	100	200	500	1000
Original	16.2 (17.2)	8.6 (13.6)	5.4 (11.6)	5.8 (12.2)	7.8 (16.3)
ADLG 50 iter	15.7 (17.8)	9.0 (13.9)	6.1 (12.0)	9.2 (16.3)	13.7 (23.2)
ADLG 100 iter	15.1 (17.8)	8.4 (14.0)	5.7 (12.1)	8.5 (16.5)	13.9 (25.0)
ADLG 200 iter	14.7 (16.2)	7.8 (11.2)	4.8 (8.0)	7.9 (14.3)	13.9 (24.0)
ADLG 500 iter	13.8 (16.1)	7.3 (11.0)	4.4 (7.1)	7.3 (13.9)	12.8 (22.8)
ADLG 1000 iter	14.3 (17.1)	8.3 (13.0)	6.1 (10.7)	8.3 (15.2)	12.4 (20.7)
Median 9x9	14.7 (15.9)	7.4 (9.9)	4.3 (6.3)	7.8 (14.1)	14.4 (26.0)

Figure A.16: Active contour segmentation (lesions) - Validation metrics (average and standard deviation) for parameters choice using Average Distance (AD), SmoothFactor = 0.1, Contraction-Bias = 0

	Iterations				
	50	100	200	500	1000
Original	0.09 (0.16)	0.18 (0.27)	0.24 (0.33)	0.26 (0.36)	0.26 (0.35)
ADLG 50 iter	0.04 (0.12)	0.08 (0.19)	0.10 (0.23)	0.11 (0.27)	0.10 (0.25)
ADLG 100 iter	0.05 (0.13)	0.08 (0.21)	0.11 (0.26)	0.13 (0.30)	0.13 (0.29)
ADLG 200 iter	0.03 (0.10)	0.04 (0.15)	0.05 (0.17)	0.04 (0.17)	0.04 (0.16)
ADLG 500 iter	0.02 (0.10)	0.04 (0.16)	0.05 (0.18)	0.05 (0.18)	0.05 (0.18)
ADLG 1000 iter	0.01 (0.01)	0.01 (0.01)	0.01 (0.02)	0.01 (0.04)	0.01 (0.04)
Median 9x9	0.04 (0.12)	0.08 (0.20)	0.11 (0.24)	0.11 (0.26)	0.10 (0.24)

Figure A.17: Active contour segmentation (lesions) - Validation metrics (average and standard deviation) for parameters choice using Sørensen–Dice coefficient (SD), SmoothFactor = 0.2, ContractionBias = 0

	Iterations				
	50	100	200	500	1000
Original	29.9 (22.6)	26.3 (23.6)	24.3 (24.1)	24.0 (24.0)	25.4 (24.5)
ADLG 50 iter	33.2 (21.0)	31.4 (20.9)	29.9 (21.6)	30.2 (21.5)	31.8 (22.5)
ADLG 100 iter	33.3 (21.1)	31.4 (21.0)	29.8 (21.8)	29.1 (22.4)	29.5 (21.9)
ADLG 200 iter	35.5 (22.4)	34.8 (22.8)	34.4 (22.9)	34.4 (22.8)	34.6 (22.6)
ADLG 500 iter	35.6 (22.5)	34.9 (22.9)	34.5 (22.9)	34.4 (22.9)	34.4 (22.9)
ADLG 1000 iter	36.7 (21.9)	36.4 (21.7)	35.9 (21.7)	35.8 (21.9)	35.8 (21.9)
Median 9x9	33.3 (21.4)	31.5 (21.6)	30.2 (22.3)	30.7 (22.0)	33.6 (23.6)

Figure A.18: Active contour segmentation (lesions) - Validation metrics (average and standard deviation) for parameters choice using Average Distance (AD), SmoothFactor = 0.2, Contraction-Bias = 0

	Iterations				
	50	100	200	500	1000
Original	0 (0.01)	0.01 (0.04)	0.02 (0.08)	0.02 (0.07)	0.02 (0.07)
ADLG 50 iter	0.01 (0.04)	0.03 (0.11)	0.05 (0.17)	0.05 (0.18)	0.04 (0.17)
ADLG 100 iter	0 (0.01)	0.01 (0.02)	0.01 (0.07)	0.02 (0.12)	0.02 (0.11)
ADLG 200 iter	0.01 (0.05)	0.03 (0.11)	0.04 (0.18)	0.05 (0.21)	0.05 (0.19)
ADLG 500 iter	0 (0.02)	0.01 (0.05)	0.01 (0.05)	0 (0.02)	0 (0.01)
ADLG 1000 iter	0 (0)	0 (0)	0 (0)	0 (0)	0 (0)
Median 9x9	0.01 (0.02)	0.01 (0.07)	0.01 (0.08)	0.01 (0.06)	0.01 (0.04)

Figure A.19: Active contour segmentation (lesions) - Validation metrics (average and standard deviation) for parameters choice using Sørensen–Dice coefficient (SD), SmoothFactor = 0.5, ContractionBias = 0

	Iterations				
	50	100	200	500	1000
Original	36.9 (21.2)	36.4 (20.9)	36.1 (21.1)	36.1 (20.7)	36.4 (20.8)
ADLG 50 iter	36.4 (21.4)	35.2 (21.7)	34.4 (22.2)	34.7 (21.9)	35.9 (21.7)
ADLG 100 iter	37.5 (21.1)	37.0 (20.7)	36.4 (20.9)	36.1 (21.2)	36.2 (21.1)
ADLG 200 iter	36.6 (21.5)	35.8 (21.3)	35.1 (21.7)	34.8 (22.1)	35.2 (21.6)
ADLG 500 iter	37.7 (22.4)	37.6 (22.6)	37.5 (22.8)	37.6 (22.6)	37.6 (22.6)
ADLG 1000 iter	38.1 (22.2)	38.1 (22.2)	38.1 (22.2)	38.1 (22.2)	38.1 (22.2)
Median 9x9	37.5 (22.3)	37.2 (22.6)	37.2 (22.6)	37.6 (22.2)	38.1 (22.2)

Figure A.20: Active contour segmentation (lesions) - Validation metrics (average and standard deviation) for parameters choice using Average Distance (AD), SmoothFactor = 0.5, ContractionBias = 0

	Iterations				
	50	100	200	500	1000
Original	0.34 (0.23)	0.56 (0.25)	0.66 (0.22)	0.66 (0.24)	0.64 (0.25)
ADLG 50 iter	0.39 (0.24)	0.60 (0.25)	0.70 (0.20)	0.68 (0.24)	0.65 (0.26)
ADLG 100 iter	0.39 (0.24)	0.60 (0.24)	0.70 (0.20)	0.69 (0.24)	0.65 (0.26)
ADLG 200 iter	0.40 (0.24)	0.60 (0.24)	0.69 (0.20)	0.69 (0.24)	0.65 (0.26)
ADLG 500 iter	0.41 (0.24)	0.60 (0.23)	0.69 (0.20)	0.69 (0.24)	0.65 (0.26)
ADLG 1000 iter	0.42 (0.24)	0.61 (0.23)	0.69 (0.21)	0.69 (0.24)	0.65 (0.26)
Median 9x9	0.39 (0.25)	0.61 (0.24)	0.69 (0.20)	0.67 (0.24)	0.63 (0.26)

Figure A.21: Active contour segmentation (lesions) - Validation metrics (average and standard deviation) for parameters choice using Sørensen–Dice coefficient (SD), SmoothFactor = 0, ContractionBias = -0.01

	Iterations				
	50	100	200	500	1000
Original	13.3 (14.8)	6.4 (9.8)	3.6 (7.0)	6.0 (11.8)	9.8 (19.6)
ADLG 50 iter	12.4 (14.9)	5.8 (8.6)	3.3 (5.2)	7.5 (14.7)	13.9 (26.5)
ADLG 100 iter	12.3 (14.8)	5.7 (8.5)	3.3 (5.0)	7.5 (14.6)	13.7 (26.5)
ADLG 200 iter	12.1 (14.6)	5.7 (8.5)	3.4 (5.1)	7.4 (14.5)	13.7 (26.5)
ADLG 500 iter	11.7 (14.6)	5.7 (8.6)	3.6 (5.3)	7.2 (14.4)	13.8 (26.7)
ADLG 1000 iter	11.3 (14.7)	5.6 (8.4)	3.9 (5.7)	7.0 (13.6)	12.8 (23.5)
Median 9x9	12.3 (14.8)	5.5 (8.3)	3.5 (5.4)	8.2 (15.0)	15.0 (28.1)

Figure A.22: Active contour segmentation (lesions) - Validation metrics (average and standard deviation) for parameters choice using Average Distance (AD), SmoothFactor = 0, ContractionBias = -0.01

	Iterations				
	50	100	200	500	1000
Original	0.34 (0.23)	0.55 (0.25)	0.67 (0.21)	0.67 (0.24)	0.64 (0.25)
ADLG 50 iter	0.38 (0.24)	0.60 (0.25)	0.70 (0.20)	0.68 (0.24)	0.65 (0.26)
ADLG 100 iter	0.39 (0.24)	0.60 (0.24)	0.70 (0.20)	0.69 (0.24)	0.65 (0.26)
ADLG 200 iter	0.39 (0.24)	0.60 (0.24)	0.69 (0.20)	0.69 (0.24)	0.65 (0.26)
ADLG 500 iter	0.40 (0.24)	0.60 (0.23)	0.69 (0.20)	0.69 (0.24)	0.65 (0.25)
ADLG 1000 iter	0.41 (0.24)	0.60 (0.23)	0.69 (0.21)	0.69 (0.24)	0.65 (0.26)
Median 9x9	0.39 (0.25)	0.60 (0.25)	0.69 (0.20)	0.67 (0.24)	0.63 (0.26)

Figure A.23: Active contour segmentation (lesions) - Validation metrics (average and standard deviation) for parameters choice using Sørensen–Dice coefficient (SD), SmoothFactor = 0.01, ContractionBias = -0.01

	Iterations				
	50	100	200	500	1000
Original	13.5 (15.0)	6.6 (9.9)	3.5 (6.4)	5.8 (11.4)	9.5 (18.7)
ADLG 50 iter	12.6 (14.9)	5.9 (8.6)	3.3 (5.3)	7.4 (14.6)	13.6 (26.1)
ADLG 100 iter	12.5 (14.9)	5.8 (8.6)	3.3 (5.0)	7.4 (14.5)	13.6 (26.2)
ADLG 200 iter	12.2 (14.8)	5.8 (8.7)	3.4 (5.0)	7.4 (14.4)	13.7 (26.3)
ADLG 500 iter	11.9 (14.7)	5.8 (8.8)	3.7 (5.3)	7.1 (14.3)	13.6 (26.5)
ADLG 1000 iter	11.5 (14.9)	5.6 (8.5)	3.9 (5.6)	6.9 (13.5)	12.6 (23.4)
Median 9x9	12.6 (14.9)	5.7 (8.4)	3.5 (5.4)	8.2 (14.9)	14.9 (27.9)

Figure A.24: Active contour segmentation (lesions) - Validation metrics (average and standard deviation) for parameters choice using Average Distance (AD), SmoothFactor = 0.01, ContractionBias = -0.01

	Iterations				
	50	100	200	500	1000
Original	0.32 (0.23)	0.54 (0.25)	0.67 (0.21)	0.68 (0.24)	0.66 (0.24)
ADLG 50 iter	0.37 (0.24)	0.59 (0.25)	0.70 (0.20)	0.69 (0.24)	0.65 (0.26)
ADLG 100 iter	0.38 (0.24)	0.59 (0.25)	0.69 (0.20)	0.69 (0.24)	0.65 (0.26)
ADLG 200 iter	0.38 (0.24)	0.59 (0.24)	0.69 (0.20)	0.69 (0.24)	0.65 (0.26)
ADLG 500 iter	0.39 (0.24)	0.59 (0.23)	0.69 (0.20)	0.69 (0.24)	0.65 (0.25)
ADLG 1000 iter	0.40 (0.24)	0.60 (0.23)	0.68 (0.21)	0.69 (0.24)	0.65 (0.26)
Median 9x9	0.38 (0.24)	0.60 (0.25)	0.69 (0.20)	0.67 (0.24)	0.64 (0.26)

Figure A.25: Active contour segmentation (lesions) - Validation metrics (average and standard deviation) for parameters choice using Sørensen–Dice coefficient (SD), SmoothFactor = 0.04, ContractionBias = -0.01

	Iterations				
	50	100	200	500	1000
Original	14.2 (15.3)	6.9 (10.2)	3.7 (6.6)	5.0 (9.9)	7.1 (14.6)
ADLG 50 iter	13.0 (15.3)	6.0 (9.0)	3.3 (5.2)	7.1 (14.2)	13.5 (25.8)
ADLG 100 iter	12.9 (15.2)	6.1 (8.9)	3.4 (5.0)	7.1 (14.1)	13.4 (25.8)
ADLG 200 iter	12.7 (15.0)	6.1 (9.0)	3.5 (5.0)	7.2 (14.2)	13.4 (25.7)
ADLG 500 iter	12.3 (15.0)	6.1 (9.1)	3.7 (5.1)	7.0 (13.9)	13.3 (25.6)
ADLG 1000 iter	11.9 (15.1)	5.8 (8.8)	3.9 (5.5)	6.8 (13.2)	12.3 (22.6)
Median 9x9	13.2 (15.1)	6.2 (8.9)	3.7 (5.5)	8.0 (14.7)	14.6 (27.4)

Figure A.26: Active contour segmentation (lesions) - Validation metrics (average and standard deviation) for parameters choice using Average Distance (AD), SmoothFactor = 0.04, ContractionBias = -0.01

	Iterations				
	50	100	200	500	1000
Original	0.30 (0.22)	0.52 (0.25)	0.66 (0.22)	0.69 (0.22)	0.68 (0.23)
ADLG 50 iter	0.35 (0.24)	0.57 (0.27)	0.67 (0.24)	0.67 (0.27)	0.63 (0.29)
ADLG 100 iter	0.35 (0.24)	0.56 (0.28)	0.65 (0.26)	0.65 (0.30)	0.61 (0.31)
ADLG 200 iter	0.36 (0.24)	0.57 (0.26)	0.67 (0.24)	0.66 (0.27)	0.63 (0.28)
ADLG 500 iter	0.37 (0.25)	0.56 (0.27)	0.65 (0.26)	0.65 (0.29)	0.62 (0.29)
ADLG 1000 iter	0.38 (0.25)	0.57 (0.25)	0.65 (0.24)	0.66 (0.27)	0.63 (0.28)
Median 9x9	0.36 (0.24)	0.58 (0.25)	0.69 (0.20)	0.68 (0.24)	0.64 (0.26)

Figure A.27: Active contour segmentation (lesions) - Validation metrics (average and standard deviation) for parameters choice using Sørensen–Dice coefficient (SD), SmoothFactor = 0.1, ContractionBias = -0.01

	Iterations				
	50	100	200	500	1000
Original	15.5 (16.2)	7.7 (10.9)	4.0 (7.0)	4.4 (8.7)	6.4 (13.9)
ADLG 50 iter	14.8 (17.1)	8.1 (12.8)	5.4 (10.8)	8.5 (16.0)	13.8 (25.0)
ADLG 100 iter	15.6 (19.2)	9.5 (16.9)	7.3 (16.1)	10.7 (19.7)	16.1 (27.2)
ADLG 200 iter	14.5 (17.0)	7.9 (12.8)	5.2 (10.4)	8.6 (16.0)	14.7 (25.3)
ADLG 500 iter	14.5 (17.9)	8.7 (14.8)	6.4 (12.8)	9.5 (17.3)	14.7 (25.2)
ADLG 1000 iter	13.7 (17.1)	7.8 (12.8)	5.8 (10.6)	8.1 (15.3)	12.6 (21.8)
Median 9x9	14.0 (15.6)	6.7 (9.4)	3.8 (5.5)	7.5 (14.2)	14.1 (26.4)

Figure A.28: Active contour segmentation (lesions) - Validation metrics (average and standard deviation) for parameters choice using Average Distance (AD), SmoothFactor = 0.1, Contraction-Bias = -0.01

	Iterations				
	50	100	200	500	1000
Original	0.10 (0.17)	0.52 (0.28)	0.66 (0.34)	0.69 (0.36)	0.68 (0.36)
ADLG 50 iter	0.06 (0.14)	0.57 (0.22)	0.67 (0.26)	0.67 (0.30)	0.63 (0.29)
ADLG 100 iter	0.05 (0.13)	0.56 (0.21)	0.65 (0.27)	0.65 (0.30)	0.61 (0.29)
ADLG 200 iter	0.03 (0.12)	0.57 (0.19)	0.67 (0.21)	0.66 (0.20)	0.63 (0.19)
ADLG 500 iter	0.02 (0.10)	0.56 (0.15)	0.65 (0.18)	0.65 (0.18)	0.62 (0.18)
ADLG 1000 iter	0.01 (0.01)	0.57 (0.01)	0.65 (0.02)	0.66 (0.04)	0.63 (0.04)
Median 9x9	0.05 (0.13)	0.58 (0.21)	0.69 (0.24)	0.68 (0.25)	0.64 (0.24)

Figure A.29: Active contour segmentation (lesions) - Validation metrics (average and standard deviation) for parameters choice using Sørensen–Dice coefficient (SD), SmoothFactor = 0.2, ContractionBias = -0.01

	Iterations				
	50	100	200	500	1000
Original	29.5 (22.8)	25.8 (23.8)	24.0 (24.4)	23.7 (24.2)	25.0 (24.7)
ADLG 50 iter	32.4 (21.1)	30.2 (21.0)	28.6 (21.7)	28.9 (21.8)	30.5 (23.0)
ADLG 100 iter	33.3 (21.0)	31.3 (21.1)	29.8 (21.8)	29.1 (22.3)	29.5 (21.9)
ADLG 200 iter	35.2 (22.8)	34.5 (23.2)	34.1 (23.2)	34.1 (23.1)	34.3 (22.9)
ADLG 500 iter	36.0 (22.3)	35.4 (22.5)	35.0 (22.5)	34.8 (22.6)	34.8 (22.6)
ADLG 1000 iter	36.7 (21.9)	36.4 (21.7)	35.9 (21.7)	35.8 (21.9)	35.7 (21.9)
Median 9x9	33.3 (21.4)	31.4 (21.7)	30.2 (22.3)	30.7 (22.0)	33.7 (23.7)

Figure A.30: Active contour segmentation (lesions) - Validation metrics (average and standard deviation) for parameters choice using Average Distance (AD), SmoothFactor = 0.2, Contraction-Bias = -0.01

	Iterations				
	50	100	200	500	1000
Original	0.02 (0.06)	0.05 (0.16)	0.08 (0.21)	0.09 (0.25)	0.09 (0.24)
ADLG 50 iter	0.01 (0.04)	0.04 (0.12)	0.06 (0.18)	0.05 (0.18)	0.05 (0.16)
ADLG 100 iter	0.02 (0.07)	0.06 (0.17)	0.08 (0.23)	0.08 (0.24)	0.07 (0.22)
ADLG 200 iter	0.02 (0.08)	0.04 (0.14)	0.06 (0.20)	0.07 (0.23)	0.06 (0.21)
ADLG 500 iter	0.01 (0.06)	0.02 (0.12)	0.02 (0.12)	0.02 (0.12)	0.02 (0.12)
ADLG 1000 iter	0 (0)	0 (0)	0 (0)	0 (0)	0 (0)
Median 9x9	0.01 (0.06)	0.03 (0.13)	0.04 (0.16)	0.05 (0.18)	0.04 (0.17)

Figure A.31: Active contour segmentation (lesions) - Validation metrics (average and standard deviation) for parameters choice using Sørensen–Dice coefficient (SD), SmoothFactor = 0.5, ContractionBias = -0.01

	Iterations				
	50	100	200	500	1000
Original	35.4 (21.5)	33.9 (21.8)	33.0 (22.4)	32.4 (22.6)	33.3 (22.3)
ADLG 50 iter	35.8 (21.5)	34.5 (21.9)	33.5 (22.6)	34.1 (22.0)	35.3 (21.8)
ADLG 100 iter	35.5 (22.2)	34.2 (22.5)	33.4 (23.0)	33.8 (22.6)	35.3 (22.2)
ADLG 200 iter	36.2 (21.5)	35.4 (21.4)	34.7 (21.8)	34.4 (22.1)	34.8 (21.6)
ADLG 500 iter	37.2 (22.4)	37.1 (22.6)	37.1 (22.6)	37.1 (22.6)	37.1 (22.6)
ADLG 1000 iter	37.5 (22.1)	37.5 (22.1)	37.5 (22.1)	37.5 (22.1)	37.5 (22.1)
Median 9x9	36.3 (21.4)	35.3 (21.5)	34.4 (22.0)	34.4 (22.0)	35.2 (21.9)

Figure A.32: Active contour segmentation (lesions) - Validation metrics (average and standard deviation) for parameters choice using Average Distance (AD), SmoothFactor = 0.5, ContractionBias = -0.01

	Iterations				
	50	100	200	500	1000
Original	0.37 (0.24)	0.58 (0.24)	0.68 (0.21)	0.67 (0.24)	0.64 (0.25)
ADLG 50 iter	0.42 (0.25)	0.62 (0.24)	0.71 (0.20)	0.68 (0.24)	0.63 (0.26)
ADLG 100 iter	0.42 (0.25)	0.62 (0.23)	0.71 (0.20)	0.68 (0.24)	0.64 (0.26)
ADLG 200 iter	0.42 (0.25)	0.62 (0.23)	0.71 (0.20)	0.69 (0.24)	0.64 (0.26)
ADLG 500 iter	0.43 (0.25)	0.62 (0.23)	0.70 (0.21)	0.69 (0.24)	0.65 (0.26)
ADLG 1000 iter	0.44 (0.25)	0.62 (0.22)	0.70 (0.22)	0.69 (0.24)	0.64 (0.27)
Median 9x9	0.42 (0.25)	0.62 (0.24)	0.70 (0.20)	0.67 (0.24)	0.63 (0.26)

Figure A.33: Active contour segmentation (lesions) - Validation metrics (average and standard deviation) for parameters choice using Sørensen–Dice coefficient (SD), SmoothFactor = 0, ContractionBias = -0.04

	Iterations				
	50	100	200	500	1000
Original	12.1 (14.0)	5.7 (9.3)	3.4 (6.5)	6.9 (13.8)	10.6 (21.4)
ADLG 50 iter	11.1 (13.7)	4.9 (7.4)	3.2 (5.4)	8.3 (15.7)	14.5 (26.9)
ADLG 100 iter	11.0 (13.7)	4.9 (7.4)	3.2 (5.4)	8.3 (15.6)	14.7 (27.0)
ADLG 200 iter	10.8 (13.5)	4.9 (7.4)	3.4 (5.7)	8.2 (15.2)	14.7 (27.1)
ADLG 500 iter	10.5 (13.6)	5.0 (7.5)	3.6 (5.7)	7.9 (15.0)	15.1 (28.7)
ADLG 1000 iter	10.0 (13.8)	4.9 (7.2)	3.8 (6.0)	7.8 (14.6)	14.5 (26.0)
Median 9x9	11.2 (13.7)	4.8 (7.1)	3.4 (5.6)	9.1 (16.0)	15.4 (28.4)

Figure A.34: Active contour segmentation (lesions) - Validation metrics (average and standard deviation) for parameters choice using Average Distance (AD), SmoothFactor = 0, ContractionBias = -0.04

	Iterations				
	50	100	200	500	1000
Original	0.37 (0.24)	0.58 (0.25)	0.68 (0.21)	0.67 (0.24)	0.64 (0.25)
ADLG 50 iter	0.41 (0.25)	0.62 (0.24)	0.71 (0.20)	0.68 (0.24)	0.64 (0.26)
ADLG 100 iter	0.42 (0.25)	0.62 (0.24)	0.71 (0.20)	0.68 (0.24)	0.64 (0.26)
ADLG 200 iter	0.42 (0.25)	0.62 (0.23)	0.70 (0.20)	0.69 (0.24)	0.64 (0.26)
ADLG 500 iter	0.43 (0.24)	0.62 (0.23)	0.70 (0.21)	0.69 (0.24)	0.65 (0.26)
ADLG 1000 iter	0.44 (0.25)	0.62 (0.23)	0.70 (0.21)	0.69 (0.24)	0.64 (0.27)
Median 9x9	0.41 (0.25)	0.62 (0.24)	0.70 (0.20)	0.67 (0.24)	0.63 (0.26)

Figure A.35: Active contour segmentation (lesions) - Validation metrics (average and standard deviation) for parameters choice using Sørensen–Dice coefficient (SD), SmoothFactor = 0.01, ContractionBias = -0.04

	Iterations				
	50	100	200	500	1000
Original	12.3 (14.1)	5.8 (9.4)	3.3 (6.2)	6.7 (13.5)	10.6 (21.5)
ADLG 50 iter	11.3 (13.9)	5.0 (7.6)	3.2 (5.3)	8.2 (15.6)	14.4 (26.7)
ADLG 100 iter	11.3 (13.8)	5.0 (7.5)	3.3 (5.3)	8.2 (15.4)	14.6 (27.0)
ADLG 200 iter	11.1 (13.7)	5.0 (7.5)	3.4 (5.5)	8.1 (15.2)	14.7 (27.3)
ADLG 500 iter	10.7 (13.8)	5.1 (7.7)	3.6 (5.6)	7.8 (14.9)	15.0 (28.7)
ADLG 1000 iter	10.3 (13.9)	5.0 (7.4)	3.8 (6.0)	7.6 (14.6)	14.3 (25.6)
Median 9x9	11.3 (13.8)	4.9 (7.4)	3.4 (5.6)	8.9 (15.8)	15.3 (28.3)

Figure A.36: Active contour segmentation (lesions) - Validation metrics (average and standard deviation) for parameters choice using Average Distance (AD), SmoothFactor = 0.01, ContractionBias = -0.04

	Iterations				
	50	100	200	500	1000
Original	0.35 (0.23)	0.57 (0.25)	0.68 (0.21)	0.68 (0.24)	0.65 (0.25)
ADLG 50 iter	0.40 (0.25)	0.61 (0.24)	0.70 (0.20)	0.69 (0.24)	0.64 (0.26)
ADLG 100 iter	0.40 (0.25)	0.62 (0.24)	0.71 (0.20)	0.69 (0.24)	0.64 (0.26)
ADLG 200 iter	0.41 (0.24)	0.61 (0.23)	0.70 (0.20)	0.69 (0.24)	0.64 (0.26)
ADLG 500 iter	0.42 (0.24)	0.61 (0.23)	0.70 (0.21)	0.69 (0.24)	0.65 (0.26)
ADLG 1000 iter	0.43 (0.25)	0.62 (0.23)	0.70 (0.21)	0.69 (0.24)	0.64 (0.27)
Median 9x9	0.40 (0.25)	0.62 (0.24)	0.70 (0.20)	0.67 (0.24)	0.63 (0.26)

Figure A.37: Active contour segmentation (lesions) - Validation metrics (average and standard deviation) for parameters choice using Sørensen–Dice coefficient (SD), SmoothFactor = 0.04, ContractionBias = -0.04

	Iterations				
	50	100	200	500	1000
Original	13.0 (14.5)	6.3 (9.9)	3.4 (6.4)	6.3 (12.7)	10.6 (21.4)
ADLG 50 iter	12.0 (14.4)	5.3 (7.9)	3.2 (5.1)	8.0 (15.2)	14.1 (26.2)
ADLG 100 iter	11.9 (14.3)	5.3 (7.8)	3.2 (5.0)	8.0 (15.2)	14.4 (26.8)
ADLG 200 iter	11.7 (14.1)	5.3 (8.0)	3.4 (5.2)	7.9 (14.9)	14.4 (26.8)
ADLG 500 iter	11.3 (14.2)	5.4 (8.1)	3.6 (5.4)	7.7 (14.8)	14.7 (28.1)
ADLG 1000 iter	11.0 (14.5)	5.3 (7.9)	3.8 (5.8)	7.4 (14.2)	14.0 (25.0)
Median 9x9	11.8 (14.1)	5.2 (7.7)	3.5 (5.5)	8.7 (15.5)	15.1 (28.1)

Figure A.38: Active contour segmentation (lesions) - Validation metrics (average and standard deviation) for parameters choice using Average Distance (AD), SmoothFactor = 0.04, ContractionBias = -0.04

	Iterations				
	50	100	200	500	1000
Original	0.33 (0.23)	0.55 (0.25)	0.67 (0.21)	0.68 (0.24)	0.66 (0.25)
ADLG 50 iter	0.38 (0.24)	0.60 (0.25)	0.70 (0.19)	0.69 (0.24)	0.64 (0.26)
ADLG 100 iter	0.38 (0.24)	0.60 (0.25)	0.70 (0.20)	0.69 (0.24)	0.64 (0.26)
ADLG 200 iter	0.39 (0.24)	0.60 (0.24)	0.70 (0.20)	0.69 (0.24)	0.65 (0.26)
ADLG 500 iter	0.40 (0.24)	0.60 (0.23)	0.70 (0.20)	0.70 (0.24)	0.65 (0.26)
ADLG 1000 iter	0.41 (0.24)	0.61 (0.23)	0.69 (0.21)	0.70 (0.24)	0.65 (0.26)
Median 9x9	0.38 (0.25)	0.60 (0.25)	0.69 (0.20)	0.67 (0.24)	0.63 (0.26)

Figure A.39: Active contour segmentation (lesions) - Validation metrics (average and standard deviation) for parameters choice using Sørensen–Dice coefficient (SD), SmoothFactor = 0.1, ContractionBias = -0.04

	Iterations				
	50	100	200	500	1000
Original	14.5 (15.7)	7.0 (10.4)	3.7 (7.0)	5.8 (11.4)	8.6 (17.7)
ADLG 50 iter	13.0 (15.2)	5.9 (8.9)	3.2 (5.1)	7.5 (14.6)	13.7 (25.3)
ADLG 100 iter	13.0 (15.2)	5.9 (8.8)	3.3 (4.9)	7.5 (14.6)	13.8 (25.7)
ADLG 200 iter	12.7 (15.0)	5.9 (8.8)	3.4 (4.9)	7.4 (14.4)	13.8 (25.8)
ADLG 500 iter	12.3 (15.1)	5.9 (8.9)	3.6 (5.2)	7.2 (14.2)	14.1 (26.6)
ADLG 1000 iter	11.9 (15.2)	5.7 (8.8)	3.8 (5.5)	7.0 (13.5)	13.2 (23.7)
Median 9x9	13.0 (14.9)	5.9 (8.4)	3.6 (5.5)	8.3 (14.9)	14.8 (27.4)

Figure A.40: Active contour segmentation (lesions) - Validation metrics (average and standard deviation) for parameters choice using Average Distance (AD), SmoothFactor = 0.1, Contraction-Bias = -0.04

	Iterations				
	50	100	200	500	1000
Original	0.08 (0.16)	0.16 (0.26)	0.21 (0.33)	0.23 (0.35)	0.22 (0.34)
ADLG 50 iter	0.06 (0.15)	0.10 (0.22)	0.12 (0.26)	0.12 (0.28)	0.11 (0.27)
ADLG 100 iter	0.05 (0.14)	0.09 (0.22)	0.12 (0.27)	0.13 (0.30)	0.12 (0.29)
ADLG 200 iter	0.02 (0.10)	0.03 (0.13)	0.03 (0.13)	0.02 (0.12)	0.02 (0.12)
ADLG 500 iter	0.02 (0.11)	0.04 (0.16)	0.04 (0.18)	0.04 (0.18)	0.04 (0.18)
ADLG 1000 iter	0 (0.01)	0.01 (0.01)	0.01 (0.03)	0.01 (0.04)	0.01 (0.04)
Median 9x9	0.05 (0.14)	0.08 (0.21)	0.09 (0.23)	0.08 (0.21)	0.07 (0.21)

Figure A.41: Active contour segmentation (lesions) - Validation metrics (average and standard deviation) for parameters choice using Sørensen–Dice coefficient (SD), SmoothFactor = 0.2, ContractionBias = -0.04

	Iterations				
	50	100	200	500	1000
Original	31.4 (23.1)	28.0 (24.3)	26.5 (25.1)	26.4 (25.0)	28.0 (25.2)
ADLG 50 iter	33.3 (21.9)	31.6 (22.3)	30.6 (22.9)	31.5 (22.6)	33.5 (23.9)
ADLG 100 iter	33.5 (21.7)	31.8 (22.1)	30.6 (22.9)	30.4 (23.2)	30.8 (22.7)
ADLG 200 iter	36.4 (22.9)	36.3 (23.1)	36.3 (23.1)	36.3 (23.0)	36.4 (23.0)
ADLG 500 iter	35.9 (22.3)	35.4 (22.5)	34.9 (22.5)	34.8 (22.6)	34.8 (22.6)
ADLG 1000 iter	36.8 (21.7)	36.5 (21.5)	36.1 (21.5)	36.0 (21.6)	36.0 (21.6)
Median 9x9	34.3 (23.3)	33.3 (23.8)	33.0 (23.8)	33.7 (23.5)	35.8 (25.8)

Figure A.42: Active contour segmentation (lesions) - Validation metrics (average and standard deviation) for parameters choice using Average Distance (AD), SmoothFactor = 0.2, Contraction-Bias = -0.04

	Iterations				
	50	100	200	500	1000
Original	0.05 (0.11)	0.11 (0.22)	0.16 (0.29)	0.18 (0.32)	0.18 (0.32)
ADLG 50 iter	0.01 (0.03)	0.02 (0.08)	0.04 (0.13)	0.05 (0.18)	0.04 (0.17)
ADLG 100 iter	0.02 (0.09)	0.04 (0.15)	0.07 (0.20)	0.08 (0.24)	0.07 (0.23)
ADLG 200 iter	0.01 (0.03)	0.01 (0.07)	0.02 (0.12)	0.02 (0.12)	0.02 (0.10)
ADLG 500 iter	0.02 (0.07)	0.03 (0.13)	0.03 (0.13)	0.02 (0.12)	0.02 (0.12)
ADLG 1000 iter	0 (0.01)	0 (0.01)	0.01 (0.02)	0.01 (0.04)	0.01 (0.04)
Median 9x9	0.03 (0.08)	0.06 (0.17)	0.09 (0.23)	0.10 (0.26)	0.09 (0.24)

Figure A.43: Active contour segmentation (lesions) - Validation metrics (average and standard deviation) for parameters choice using Sørensen–Dice coefficient (SD), SmoothFactor = 0.5, ContractionBias = -0.04

	Iterations				
	50	100	200	500	1000
Original	33.3 (22.1)	30.9 (22.8)	29.1 (23.4)	28.3 (23.4)	28.9 (23.5)
ADLG 50 iter	35.9 (21.0)	34.9 (20.8)	34.0 (21.2)	34.0 (21.5)	34.6 (21.5)
ADLG 100 iter	35.6 (21.2)	34.6 (21.0)	33.5 (21.5)	33.4 (21.7)	34.2 (21.6)
ADLG 200 iter	36.8 (22.3)	36.6 (22.6)	36.4 (22.7)	36.5 (22.6)	36.8 (22.3)
ADLG 500 iter	36.5 (22.7)	36.3 (23.0)	36.2 (23.1)	36.4 (23.0)	36.4 (22.9)
ADLG 1000 iter	37.0 (21.8)	36.8 (21.5)	36.3 (21.4)	36.0 (21.6)	36.0 (21.6)
Median 9x9	35.2 (21.5)	33.6 (21.7)	32.1 (22.6)	32.0 (22.9)	33.6 (22.4)

Figure A.44: Active contour segmentation (lesions) - Validation metrics (average and standard deviation) for parameters choice using Average Distance (AD), SmoothFactor = 0.5, ContractionBias = -0.04

	Iterations				
	50	100	200	500	1000
Original	0.42 (0.25)	0.63 (0.23)	0.70 (0.21)	0.66(0.23)	0.59 (0.26)
ADLG 50 iter	0.46 (0.25)	0.66 (0.22)	0.72 (0.21)	0.66(0.24)	0.60 (0.27)
ADLG 100 iter	0.46 (0.25)	0.66 (0.22)	0.72 (0.21)	0.66(0.24)	0.61 (0.27)
ADLG 200 iter	0.46 (0.25)	0.66 (0.22)	0.72 (0.21)	0.66(0.24)	0.60 (0.28)
ADLG 500 iter	0.47 (0.25)	0.66 (0.22)	0.73 (0.21)	0.67(0.25)	0.61 (0.28)
ADLG 1000 iter	0.48 (0.25)	0.66 (0.21)	0.73 (0.21)	0.67(0.26)	0.61 (0.28)
Median 9x9	0.45 (0.26)	0.66 (0.22)	0.71 (0.20)	0.65(0.25)	0.60 (0.27)

Figure A.45: Active contour segmentation (lesions) - Validation metrics (average and standard deviation) for parameters choice using Sørensen–Dice coefficient (SD), SmoothFactor = 0, ContractionBias = -0.1

	Iterations				
	50	100	200	500	1000
Original	10.6 (13.5)	4.70 (8.1)	3.7 (6.3)	8.3 (16.2)	13.6 (22.4)
ADLG 50 iter	9.6 (12.9)	4.10 (6.2)	3.6 (6.8)	10.3 (17.7)	17.0 (29.0)
ADLG 100 iter	9.5 (12.9)	4.00 (6.1)	3.6 (6.9)	10.4 (17.8)	17.3 (29.4)
ADLG 200 iter	9.3 (12.8)	4.00 (6.0)	3.6 (7.0)	10.3 (17.6)	18.6 (30.1)
ADLG 500 iter	9.1 (13.0)	4.00 (5.9)	3.7 (7.3)	10.8 (17.6)	18.7 (30.5)
ADLG 1000 iter	8.7 (13.0)	3.80 (5.5)	3.9 (7.4)	10.6 (16.8)	18.9 (29.6)
Median 9x9	9.6 (12.8)	3.90 (5.9)	3.6 (6.7)	11.1 (18.3)	17.3 (28.1)

Figure A.46: Active contour segmentation (lesions) - Validation metrics (average and standard deviation) for parameters choice using Average Distance (AD), SmoothFactor = 0, ContractionBias = -0.1

	Iterations				
	50	100	200	500	1000
Original	0.42 (0.25)	0.63 (0.23)	0.70 (0.21)	0.66(0.23)	0.59 (0.26)
ADLG 50 iter	0.45 (0.25)	0.65 (0.22)	0.72 (0.21)	0.66(0.24)	0.60 (0.27)
ADLG 100 iter	0.46 (0.26)	0.66 (0.22)	0.72 (0.21)	0.66(0.24)	0.61 (0.27)
ADLG 200 iter	0.46 (0.25)	0.66 (0.22)	0.72 (0.21)	0.66(0.24)	0.60 (0.27)
ADLG 500 iter	0.47 (0.25)	0.66 (0.22)	0.73 (0.21)	0.67(0.25)	0.61 (0.28)
ADLG 1000 iter	0.48 (0.25)	0.66 (0.21)	0.73 (0.21)	0.67(0.25)	0.61 (0.28)
Median 9x9	0.45 (0.26)	0.65 (0.22)	0.71 (0.20)	0.65(0.25)	0.60 (0.27)

Figure A.47: Active contour segmentation (lesions) - Validation metrics (average and standard deviation) for parameters choice using Sørensen–Dice coefficient (SD), SmoothFactor = 0.01, ContractionBias = -0.1

	Iterations				
	50	100	200	500	1000
Original	10.8 (13.6)	4.8 (8.3)	3.7 (6.3)	8.2 (16.1)	13.5 (22.6)
ADLG 50 iter	9.7 (13.0)	4.2 (6.3)	3.5 (6.7)	10.2 (17.6)	16.9 (28.9)
ADLG 100 iter	9.6 (12.9)	4.1 (6.2)	3.6 (6.8)	10.3 (17.6)	17.2 (29.4)
ADLG 200 iter	9.5 (12.9)	4.0 (6.0)	3.6 (6.9)	10.2 (17.6)	17.9 (29.6)
ADLG 500 iter	9.2 (13.2)	4.1 (6.1)	3.7 (7.3)	10.7 (17.5)	18.8 (30.8)
ADLG 1000 iter	8.7 (13.0)	3.9 (5.6)	3.9 (7.4)	10.4 (16.6)	18.7 (29.5)
Median 9x9	9.6 (12.9)	4.0 (6.0)	3.7 (6.7)	11.0 (18.2)	17.2 (28.1)

Figure A.48: Active contour segmentation (lesions) - Validation metrics (average and standard deviation) for parameters choice using Average Distance (AD), SmoothFactor = 0.01, ContractionBias = -0.1

	Iterations				
	50	100	200	500	1000
Original	0.40 (0.25)	0.62 (0.23)	0.70 (0.21)	0.66(0.23)	0.60 (0.26)
ADLG 50 iter	0.44 (0.25)	0.65 (0.22)	0.72 (0.21)	0.66(0.24)	0.61 (0.26)
ADLG 100 iter	0.45 (0.25)	0.65 (0.22)	0.72 (0.21)	0.67(0.24)	0.61 (0.27)
ADLG 200 iter	0.45 (0.25)	0.65 (0.22)	0.72 (0.21)	0.67(0.24)	0.62 (0.27)
ADLG 500 iter	0.46 (0.25)	0.65 (0.22)	0.73 (0.21)	0.67(0.25)	0.61 (0.28)
ADLG 1000 iter	0.47 (0.25)	0.65 (0.21)	0.73 (0.21)	0.67(0.25)	0.61 (0.28)
Median 9x9	0.44 (0.26)	0.65 (0.22)	0.71 (0.20)	0.65(0.24)	0.61 (0.27)

Figure A.49: Active contour segmentation (lesions) - Validation metrics (average and standard deviation) for parameters choice using Sørensen–Dice coefficient (SD), SmoothFactor = 0.04, ContractionBias = -0.1

	Iterations				
	50	100	200	500	1000
Original	11.2 (13.7)	5.1 (8.7)	3.7 (6.5)	7.9 (15.6)	13.4 (22.9)
ADLG 50 iter	10.0 (13.1)	4.3 (6.5)	3.5 (6.6)	9.9 (17.3)	16.4 (28.6)
ADLG 100 iter	9.9 (13.1)	4.3 (6.4)	3.5 (6.6)	9.9 (17.3)	16.5 (29.0)
ADLG 200 iter	9.8 (13.1)	4.3 (6.4)	3.5 (6.5)	9.8 (17.1)	16.7 (29.4)
ADLG 500 iter	9.5 (13.3)	4.3 (6.4)	3.7 (6.9)	10.4 (17.2)	18.5 (30.6)
ADLG 1000 iter	9.0 (13.1)	4.1 (6.0)	3.8 (7.0)	10.1 (16.3)	18.2 (28.9)
Median 9x9	9.9 (13.0)	4.1 (6.2)	3.6 (6.4)	10.5 (17.6)	16.9 (28.4)

Figure A.50: Active contour segmentation (lesions) - Validation metrics (average and standard deviation) for parameters choice using Average Distance (AD), SmoothFactor = 0.04, ContractionBias = -0.1

	Iterations				
	50	100	200	500	1000
Original	0.38 (0.24)	0.60 (0.24)	0.70 (0.20)	0.67(0.23)	0.62 (0.26)
ADLG 50 iter	0.43 (0.25)	0.64 (0.23)	0.72 (0.20)	0.67(0.24)	0.62 (0.26)
ADLG 100 iter	0.43 (0.25)	0.64 (0.23)	0.72 (0.20)	0.67(0.24)	0.62 (0.26)
ADLG 200 iter	0.44 (0.25)	0.64 (0.23)	0.72 (0.21)	0.68(0.24)	0.62 (0.27)
ADLG 500 iter	0.45 (0.25)	0.64 (0.22)	0.72 (0.21)	0.68(0.25)	0.62 (0.28)
ADLG 1000 iter	0.46 (0.25)	0.64 (0.22)	0.72 (0.21)	0.69(0.24)	0.62 (0.28)
Median 9x9	0.43 (0.25)	0.64 (0.23)	0.71 (0.20)	0.66(0.24)	0.62 (0.27)

Figure A.51: Active contour segmentation (lesions) - Validation metrics (average and standard deviation) for parameters choice using Sørensen–Dice coefficient (SD), SmoothFactor = 0.1, ContractionBias = -0.1

	Iterations				
	50	100	200	500	1000
Original	12.1 (14.2)	5.7 (9.3)	3.5 (6.2)	7.6 (14.8)	12.7 (22.6)
ADLG 50 iter	10.7 (13.6)	4.6 (6.9)	3.3 (5.9)	9.4 (16.8)	15.9 (28.1)
ADLG 100 iter	10.6 (13.4)	4.6 (6.9)	3.4 (6.1)	9.4 (16.7)	15.9 (28.3)
ADLG 200 iter	10.4 (13.4)	4.6 (7.0)	3.4 (6.0)	9.3 (16.3)	16.1 (28.7)
ADLG 500 iter	10.1 (13.5)	4.6 (7.0)	3.6 (6.2)	9.9 (16.6)	17.5 (29.8)
ADLG 1000 iter	9.6 (13.5)	4.5 (6.8)	3.7 (6.5)	9.0 (15.5)	17.4 (27.9)
Median 9x9	10.7 (13.5)	4.5 (6.7)	3.5 (6.1)	9.7 (17.1)	15.9 (28.2)

Figure A.52: Active contour segmentation (lesions) - Validation metrics (average and standard deviation) for parameters choice using Average Distance (AD), SmoothFactor = 0.1, Contraction-Bias = -0.1

	Iterations				
	50	100	200	500	1000
Original	0.34 (0.24)	0.57 (0.25)	0.69 (0.20)	0.69(0.23)	0.63 (0.26)
ADLG 50 iter	0.39 (0.26)	0.60 (0.26)	0.69 (0.24)	0.65(0.27)	0.60 (0.29)
ADLG 100 iter	0.40 (0.25)	0.62 (0.25)	0.70 (0.22)	0.67(0.25)	0.63 (0.28)
ADLG 200 iter	0.40 (0.25)	0.61 (0.26)	0.69 (0.25)	0.66(0.27)	0.61 (0.29)
ADLG 500 iter	0.42 (0.25)	0.62 (0.24)	0.70 (0.23)	0.68(0.26)	0.62 (0.29)
ADLG 1000 iter	0.42 (0.26)	0.60 (0.25)	0.68 (0.25)	0.67(0.27)	0.61 (0.30)
Median 9x9	0.40 (0.25)	0.62 (0.24)	0.71 (0.19)	0.67(0.24)	0.63 (0.26)

Figure A.53: Active contour segmentation (lesions) - Validation metrics (average and standard deviation) for parameters choice using Sørensen–Dice coefficient (SD), SmoothFactor = 0.2, ContractionBias = -0.1

	Iterations				
	50	100	200	500	1000
Original	14.0 (15.3)	6.7 (10.4)	3.6 (6.6)	6.5 (12.8)	11.3 (20.9)
ADLG 50 iter	13.2 (16.2)	6.7 (11.8)	5.1 (10.7)	10.5 (17.6)	16.7 (27.1)
ADLG 100 iter	12.5 (15.7)	6.1 (10.9)	4.4 (9.4)	9.4 (17.0)	15.0 (26.7)
ADLG 200 iter	12.8 (16.0)	6.8 (12.0)	5.2 (10.8)	10.0 (17.3)	15.8 (27.3)
ADLG 500 iter	12.0 (15.6)	6.2 (11.1)	4.6 (9.6)	9.6 (16.7)	16.6 (28.4)
ADLG 1000 iter	12.1 (16.2)	6.8 (12.0)	5.5 (10.9)	9.8 (16.5)	16.0 (25.9)
Median 9x9	12.1 (14.3)	5.4 (7.7)	3.6 (5.7)	8.9 (15.8)	15.1 (27.8)

Figure A.54: Active contour segmentation (lesions) - Validation metrics (average and standard deviation) for parameters choice using Average Distance (AD), SmoothFactor = 0.2, Contraction-Bias = -0.1

	Iterations				
	50	100	200	500	1000
Original	0.03 (0.08)	0.07 (0.18)	0.11 (0.24)	0.12(0.26)	0.11 (0.24)
ADLG 50 iter	0.04 (0.12)	0.08 (0.21)	0.11 (0.25)	0.10(0.26)	0.10 (0.25)
ADLG 100 iter	0.03 (0.11)	0.06 (0.19)	0.07 (0.22)	0.07(0.23)	0.07 (0.22)
ADLG 200 iter	0.01 (0.08)	0.02 (0.12)	0.02 (0.12)	0.02(0.12)	0.02 (0.12)
ADLG 500 iter	0.02 (0.08)	0.02 (0.12)	0.02 (0.12)	0.02(0.12)	0.02 (0.12)
ADLG 1000 iter	0 (0.01)	0 (0.01)	0 (0.01)	0(0.01)	0 (0.01)
Median 9x9	0.02 (0.08)	0.05 (0.16)	0.06 (0.20)	0.06(0.18)	0.05 (0.18)

Figure A.55: Active contour segmentation (lesions) - Validation metrics (average and standard deviation) for parameters choice using Sørensen–Dice coefficient (SD), SmoothFactor = 0.5, ContractionBias = -0.1

	Iterations				
	50	100	200	500	1000
Original	34.6 (23.2)	32.9 (24.4)	31.8 (25.3)	32.0 (25.1)	33.4 (24.7)
ADLG 50 iter	34.2 (22.2)	32.7 (22.5)	31.7 (23.0)	32.5 (22.6)	34.1 (23.0)
ADLG 100 iter	35.5 (23.1)	35.0 (23.3)	34.5 (23.7)	34.5 (23.8)	34.6 (23.6)
ADLG 200 iter	36.8 (22.6)	36.8 (22.7)	36.8 (22.7)	36.8 (22.7)	36.8 (22.7)
ADLG 500 iter	36.8 (22.6)	36.8 (22.7)	36.8 (22.7)	36.8 (22.7)	36.8 (22.7)
ADLG 1000 iter	37.2 (22.2)	37.2 (22.2)	37.2 (22.2)	37.2 (22.2)	37.2 (22.2)
Median 9x9	35.5 (22.6)	34.5 (23.2)	34.2 (23.2)	34.8 (22.6)	36.6 (23.9)

Figure A.56: Active contour segmentation (lesions) - Validation metrics (average and standard deviation) for parameters choice using Average Distance (AD), SmoothFactor = 0.5, ContractionBias = -0.1

	Iterations				
	50	100	200	500	1000
Original	0.49 (0.25)	0.68 (0.19)	0.70 (0.21)	0.54(0.28)	0.41 (0.32)
ADLG 50 iter	0.51 (0.25)	0.70 (0.19)	0.70 (0.22)	0.56(0.29)	0.47 (0.33)
ADLG 100 iter	0.51 (0.25)	0.70 (0.19)	0.70 (0.22)	0.56(0.29)	0.48 (0.33)
ADLG 200 iter	0.51 (0.25)	0.70 (0.19)	0.70 (0.23)	0.57(0.30)	0.48 (0.33)
ADLG 500 iter	0.52 (0.25)	0.70 (0.19)	0.69 (0.23)	0.56(0.30)	0.47 (0.33)
ADLG 1000 iter	0.53 (0.25)	0.70 (0.19)	0.69 (0.24)	0.55(0.29)	0.46 (0.33)
Median 9x9	0.51 (0.25)	0.69 (0.19)	0.69 (0.22)	0.57(0.28)	0.51 (0.31)

Figure A.57: Active contour segmentation (lesions) - Validation metrics (average and standard deviation) for parameters choice using Sørensen–Dice coefficient (SD), SmoothFactor = 0, ContractionBias = -0.2

	Iterations				
	50	100	200	500	1000
Original	8.2 (12.0)	2.9 (4.4)	4.9 (7.7)	17.0 (22.7)	32.9 (34.1)
ADLG 50 iter	7.8 (12.2)	2.9 (4.2)	5.8 (8.9)	19.9 (26.2)	35.7 (44.3)
ADLG 100 iter	7.8 (12.2)	3.0 (4.1)	6.1 (9.2)	20.6 (26.9)	36.6 (45.1)
ADLG 200 iter	7.7 (12.1)	3.0 (4.0)	6.2 (9.5)	20.8 (27.6)	36.9 (45.5)
ADLG 500 iter	7.5 (12.3)	3.1 (4.3)	6.8 (9.7)	21.1 (26.5)	39.1 (46.8)
ADLG 1000 iter	7.3 (12.3)	3.1 (4.4)	7.0 (10.0)	20.5 (24.3)	37.8 (39.8)
Median 9x9	7.7 (12.1)	3.0 (4.2)	5.9 (9.0)	18.7 (26.2)	31.5 (42.1)

Figure A.58: Active contour segmentation (lesions) - Validation metrics (average and standard deviation) for parameters choice using Average Distance (AD), SmoothFactor = 0, ContractionBias = -0.2

	Iterations				
	50	100	200	500	1000
Original	0.49 (0.25)	0.68 (0.19)	0.70 (0.21)	0.54(0.28)	0.41 (0.31)
ADLG 50 iter	0.50 (0.25)	0.69 (0.19)	0.70 (0.22)	0.58(0.28)	0.49 (0.32)
ADLG 100 iter	0.51 (0.25)	0.69 (0.20)	0.70 (0.22)	0.56(0.29)	0.48 (0.33)
ADLG 200 iter	0.51 (0.25)	0.70 (0.19)	0.70 (0.23)	0.57(0.30)	0.49 (0.33)
ADLG 500 iter	0.52 (0.25)	0.70 (0.19)	0.70 (0.23)	0.57(0.30)	0.48 (0.33)
ADLG 1000 iter	0.53 (0.25)	0.70 (0.19)	0.69 (0.23)	0.56(0.29)	0.46 (0.33)
Median 9x9	0.51 (0.25)	0.69 (0.19)	0.69 (0.22)	0.58(0.27)	0.51 (0.31)

Figure A.59: Active contour segmentation (lesions) - Validation metrics (average and standard deviation) for parameters choice using Sørensen–Dice coefficient (SD), SmoothFactor = 0.01, ContractionBias = -0.2

	Iterations				
	50	100	200	500	1000
Original	8.3 (12.1)	3.0 (4.5)	4.7 (7.6)	17.0 (22.7)	33.2 (35.2)
ADLG 50 iter	7.9 (12.2)	2.9 (4.3)	5.7 (8.8)	18.3 (24.9)	33.0 (42.3)
ADLG 100 iter	7.8 (12.2)	3.0 (4.2)	5.9 (9.0)	20.2 (26.6)	36.4 (45.2)
ADLG 200 iter	7.7 (12.1)	3.0 (4.1)	6.1 (9.3)	20.3 (27.0)	36.2 (44.6)
ADLG 500 iter	7.6 (12.4)	3.1 (4.4)	6.5 (9.7)	19.9 (26.0)	35.8 (43.8)
ADLG 1000 iter	7.4 (12.3)	3.2 (4.4)	6.8 (9.9)	20.2 (24.3)	37.6 (39.6)
Median 9x9	7.8 (12.1)	3.0 (4.2)	5.9 (8.9)	18.1 (25.8)	30.6 (41.3)

Figure A.60: Active contour segmentation (lesions) - Validation metrics (average and standard deviation) for parameters choice using Average Distance (AD), SmoothFactor = 0.01, ContractionBias = -0.2

	Iterations				
	50	100	200	500	1000
Original	0.48 (0.25)	0.68 (0.19)	0.70 (0.20)	0.55(0.28)	0.42 (0.31)
ADLG 50 iter	0.50 (0.25)	0.69 (0.19)	0.70 (0.22)	0.59(0.28)	0.51 (0.32)
ADLG 100 iter	0.50 (0.25)	0.69 (0.20)	0.71 (0.22)	0.58(0.28)	0.49 (0.33)
ADLG 200 iter	0.50 (0.25)	0.69 (0.20)	0.71 (0.22)	0.59(0.29)	0.51 (0.33)
ADLG 500 iter	0.52 (0.25)	0.69 (0.19)	0.70 (0.23)	0.58(0.30)	0.49 (0.33)
ADLG 1000 iter	0.52 (0.25)	0.70 (0.19)	0.70 (0.23)	0.57(0.29)	0.47 (0.33)
Median 9x9	0.50 (0.26)	0.69 (0.19)	0.70 (0.22)	0.59(0.27)	0.53 (0.31)

Figure A.61: Active contour segmentation (lesions) - Validation metrics (average and standard deviation) for parameters choice using Sørensen–Dice coefficient (SD), SmoothFactor = 0.04, ContractionBias = -0.2

	Iterations				
	50	100	200	500	1000
Original	8.6 (12.2)	3.1 (4.7)	4.6 (7.5)	16.2 (22.0)	32.3 (36.2)
ADLG 50 iter	8.1 (12.2)	3.1 (4.5)	5.4 (8.5)	17.2 (24.2)	31.7 (42.7)
ADLG 100 iter	8.1 (12.3)	3.1 (4.4)	5.5 (8.7)	17.6 (24.4)	33.3 (42.9)
ADLG 200 iter	7.9 (12.3)	3.1 (4.3)	5.7 (9.0)	17.7 (24.4)	32.3 (42.6)
ADLG 500 iter	7.7 (12.5)	3.2 (4.5)	6.1 (9.4)	19.0 (25.0)	35.2 (43.4)
ADLG 1000 iter	7.5 (12.4)	3.1 (4.5)	6.5 (9.6)	19.2 (23.9)	35.3 (39.2)
Median 9x9	8.1 (12.2)	3.0 (4.4)	5.6 (8.7)	16.7 (23.6)	25.8 (36.0)

Figure A.62: Active contour segmentation (lesions) - Validation metrics (average and standard deviation) for parameters choice using Average Distance (AD), SmoothFactor = 0.04, ContractionBias = -0.2

	Iterations				
	50	100	200	500	1000
Original	0.46 (0.26)	0.67 (0.21)	0.71 (0.20)	0.59(0.27)	0.47 (0.29)
ADLG 50 iter	0.48 (0.26)	0.69 (0.20)	0.71 (0.21)	0.60(0.27)	0.52 (0.32)
ADLG 100 iter	0.49 (0.25)	0.68 (0.20)	0.71 (0.22)	0.60(0.28)	0.52 (0.32)
ADLG 200 iter	0.49 (0.25)	0.69 (0.20)	0.71 (0.22)	0.60(0.28)	0.52 (0.32)
ADLG 500 iter	0.50 (0.25)	0.69 (0.20)	0.72 (0.22)	0.60(0.29)	0.50 (0.33)
ADLG 1000 iter	0.51 (0.25)	0.69 (0.20)	0.72 (0.22)	0.60(0.29)	0.51 (0.32)
Median 9x9	0.49 (0.26)	0.69 (0.20)	0.70 (0.21)	0.60(0.27)	0.54 (0.30)

Figure A.63: Active contour segmentation (lesions) - Validation metrics (average and standard deviation) for parameters choice using Sørensen–Dice coefficient (SD), SmoothFactor = 0.1, ContractionBias = -0.2

	Iterations				
	50	100	200	500	1000
Original	9.4 (12.8)	3.8 (6.9)	4.4 (6.9)	13.2 (19.5)	26.3 (32.2)
ADLG 50 iter	8.6 (12.4)	3.3 (4.9)	4.9 (8.4)	15.5 (21.7)	27.9 (36.5)
ADLG 100 iter	8.5 (12.4)	3.3 (4.8)	5.1 (8.6)	16.2 (21.9)	28.7 (37.0)
ADLG 200 iter	8.3 (12.3)	3.3 (4.7)	5.2 (8.8)	16.0 (21.9)	29.0 (37.2)
ADLG 500 iter	8.1 (12.6)	3.3 (4.9)	5.4 (9.0)	17.3 (22.5)	33.1 (39.8)
ADLG 1000 iter	7.8 (12.6)	3.1 (4.7)	5.4 (8.9)	16.4 (21.8)	31.0 (37.4)
Median 9x9	8.6 (12.4)	3.2 (4.8)	5.3 (8.5)	16.2 (23.2)	24.6 (34.3)

Figure A.64: Active contour segmentation (lesions) - Validation metrics (average and standard deviation) for parameters choice using Average Distance (AD), SmoothFactor = 0.1, Contraction-Bias = -0.2

	Iterations				
	50	100	200	500	1000
Original	0.43 (0.26)	0.65 (0.22)	0.71 (0.20)	0.61(0.26)	0.51 (0.29)
ADLG 50 iter	0.46 (0.26)	0.67 (0.21)	0.73 (0.20)	0.62(0.26)	0.53 (0.30)
ADLG 100 iter	0.47 (0.26)	0.67 (0.21)	0.73 (0.20)	0.62(0.27)	0.53 (0.31)
ADLG 200 iter	0.47 (0.25)	0.67 (0.21)	0.73 (0.20)	0.64(0.26)	0.54 (0.31)
ADLG 500 iter	0.48 (0.25)	0.68 (0.21)	0.73 (0.20)	0.64(0.27)	0.54 (0.31)
ADLG 1000 iter	0.49 (0.25)	0.68 (0.20)	0.73 (0.21)	0.62(0.28)	0.53 (0.31)
Median 9x9	0.46 (0.26)	0.67 (0.21)	0.72 (0.20)	0.63(0.26)	0.56 (0.29)

Figure A.65: Active contour segmentation (lesions) - Validation metrics (average and standard deviation) for parameters choice using Sørensen–Dice coefficient (SD), SmoothFactor = 0.2, ContractionBias = -0.2

	Iterations				
	50	100	200	500	1000
Original	10.8 (13.5)	4.6 (7.8)	3.9 (6.0)	11.8 (18.8)	23.4 (30.7)
ADLG 50 iter	9.5 (12.9)	3.7 (5.6)	3.9 (7.1)	13.7 (20.4)	25.0 (32.6)
ADLG 100 iter	9.4 (12.8)	3.8 (5.6)	4.1 (7.4)	14.3 (20.5)	26.7 (34.5)
ADLG 200 iter	9.2 (12.8)	3.7 (5.6)	4.0 (7.6)	13.1 (19.1)	25.6 (34.7)
ADLG 500 iter	8.9 (13.0)	3.6 (5.6)	4.2 (7.7)	13.1 (18.9)	25.5 (32.9)
ADLG 1000 iter	8.5 (12.8)	3.5 (5.4)	4.6 (8.2)	14.4 (19.6)	28.0 (34.7)
Median 9x9	9.3 (12.8)	3.7 (5.5)	4.0 (6.9)	13.4 (20.1)	21.8 (31.8)

Figure A.66: Active contour segmentation (lesions) - Validation metrics (average and standard deviation) for parameters choice using Average Distance (AD), SmoothFactor = 0.2, Contraction-Bias = -0.2

	Iterations				
	50	100	200	500	1000
Original	0.21 (0.25)	0.36 (0.33)	0.45 (0.37)	0.43(0.37)	0.38 (0.36)
ADLG 50 iter	0.20 (0.26)	0.33 (0.35)	0.39 (0.38)	0.36(0.38)	0.32 (0.36)
ADLG 100 iter	0.20 (0.26)	0.34 (0.35)	0.38 (0.39)	0.35(0.38)	0.31 (0.36)
ADLG 200 iter	0.17 (0.23)	0.28 (0.33)	0.34 (0.38)	0.32(0.37)	0.29 (0.36)
ADLG 500 iter	0.23 (0.29)	0.33 (0.36)	0.36 (0.38)	0.33(0.38)	0.29 (0.36)
ADLG 1000 iter	0.22 (0.27)	0.32 (0.34)	0.36 (0.37)	0.34(0.37)	0.28 (0.34)
Median 9x9	0.20 (0.26)	0.34 (0.34)	0.42 (0.39)	0.40(0.39)	0.38 (0.38)

Figure A.67: Active contour segmentation (lesions) - Validation metrics (average and standard deviation) for parameters choice using Sørensen–Dice coefficient (SD), SmoothFactor = 0.5, ContractionBias = -0.2

	Iterations				
	50	100	200	500	1000
Original	25.0 (23.3)	20.1 (24.0)	17.8 (24.3)	20.5 (25.4)	24.6 (26.2)
ADLG 50 iter	25.3 (23.3)	21.1 (24.0)	19.5 (24.4)	22.2 (23.9)	26.9 (27.7)
ADLG 100 iter	25.2 (24.2)	21.4 (25.2)	20.8 (25.4)	23.9 (25.5)	28.1 (26.5)
ADLG 200 iter	26.2 (23.0)	22.6 (23.6)	21.3 (24.0)	24.7 (23.9)	29.2 (26.1)
ADLG 500 iter	26.4 (25.9)	23.7 (26.8)	23.4 (26.5)	27.0 (26.4)	31.4 (27.7)
ADLG 1000 iter	24.9 (24.3)	22.0 (24.8)	21.5 (24.6)	24.8 (24.7)	31.1 (26.6)
Median 9x9	24.4 (21.8)	19.2 (22.1)	17.5 (22.7)	19.9 (23.5)	23.4 (27.9)

Figure A.68: Active contour segmentation (lesions) - Validation metrics (average and standard deviation) for parameters choice using Average Distance (AD), SmoothFactor = 0.5, ContractionBias = -0.2

	Iterations				
	50	100	200	500	1000
Original	0.52 (0.24)	0.54 (0.21)	0.33 (0.24)	0.12(0.12)	0.11 (0.11)
ADLG 50 iter	0.52 (0.24)	0.55 (0.21)	0.33 (0.24)	0.12(0.12)	0.11 (0.10)
ADLG 100 iter	0.52 (0.24)	0.55 (0.21)	0.34 (0.24)	0.12(0.12)	0.11 (0.10)
ADLG 200 iter	0.52 (0.24)	0.55 (0.21)	0.34 (0.24)	0.12(0.12)	0.11 (0.10)
ADLG 500 iter	0.52 (0.24)	0.55 (0.21)	0.34 (0.24)	0.12(0.12)	0.11 (0.10)
ADLG 1000 iter	0.52 (0.24)	0.55 (0.21)	0.34 (0.24)	0.12(0.12)	0.11 (0.11)
Median 9x9	0.52 (0.24)	0.55 (0.21)	0.34 (0.24)	0.12(0.12)	0.11 (0.10)

Figure A.69: Active contour segmentation (lesions) - Validation metrics (average and standard deviation) for parameters choice using Sørensen–Dice coefficient (SD), SmoothFactor = 0, ContractionBias = -0.5

	Iterations				
	50	100	200	500	1000
Original	7.2 (10.9)	8.5 (7.8)	33.2 (20.2)	96.3 (40.2)	122.3 (53.3)
ADLG 50 iter	7.2 (10.9)	8.4 (7.8)	32.2 (20.1)	94.3 (41.1)	121.0 (54.4)
ADLG 100 iter	7.3 (10.9)	8.4 (7.7)	31.8 (19.8)	92.8 (41.4)	119.6 (54.4)
ADLG 200 iter	7.3 (10.9)	8.4 (7.7)	31.7 (19.7)	92.1 (41.8)	119.2 (54.9)
ADLG 500 iter	7.3 (10.9)	8.3 (7.6)	31.5 (19.4)	90.7 (41.7)	118.0 (55.3)
ADLG 1000 iter	7.2 (10.9)	8.5 (7.7)	31.5 (19.5)	91.0 (41.4)	118.1 (55.4)
Median 9x9	7.2 (10.9)	8.4 (7.8)	32.1 (20.2)	92.5 (41.9)	119.2 (55.6)

Figure A.70: Active contour segmentation (lesions) - Validation metrics (average and standard deviation) for parameters choice using Average Distance (AD), SmoothFactor = 0, ContractionBias = -0.5

	Iterations				
	50	100	200	500	1000
Original	0.52 (0.24)	0.55 (0.21)	0.33 (0.24)	0.12(0.12)	0.11 (0.11)
ADLG 50 iter	0.52 (0.24)	0.55 (0.21)	0.34 (0.24)	0.12(0.12)	0.11 (0.10)
ADLG 100 iter	0.52 (0.24)	0.55 (0.21)	0.34 (0.24)	0.12(0.12)	0.11 (0.10)
ADLG 200 iter	0.52 (0.24)	0.55 (0.21)	0.34 (0.24)	0.12(0.12)	0.11 (0.10)
ADLG 500 iter	0.52 (0.24)	0.55 (0.21)	0.34 (0.24)	0.12(0.12)	0.11 (0.10)
ADLG 1000 iter	0.52 (0.24)	0.55 (0.21)	0.34 (0.24)	0.12(0.12)	0.11 (0.11)
Median 9x9	0.52 (0.24)	0.55 (0.21)	0.34 (0.24)	0.12(0.12)	0.11 (0.10)

Figure A.71: Active contour segmentation (lesions) - Validation metrics (average and standard deviation) for parameters choice using Sørensen–Dice coefficient (SD), SmoothFactor = 0.01, ContractionBias = -0.5

	Iterations				
	50	100	200	500	1000
Original	7.2 (10.9)	8.5 (7.8)	33.0 (20.1)	96.0 (39.5)	122.6 (53.0)
ADLG 50 iter	7.2 (10.9)	8.4 (7.8)	32.2 (20.1)	94.1 (41.1)	120.6 (53.8)
ADLG 100 iter	7.2 (10.9)	8.4 (7.7)	31.7 (19.7)	92.9 (41.5)	119.7 (54.4)
ADLG 200 iter	7.3 (10.9)	8.4 (7.7)	31.7 (19.7)	92.2 (41.8)	119.3 (54.9)
ADLG 500 iter	7.3 (10.9)	8.3 (7.7)	31.3 (19.3)	90.5 (41.5)	117.7 (55.2)
ADLG 1000 iter	7.2 (10.9)	8.4 (7.7)	31.5 (19.5)	90.9 (41.3)	117.8 (55.1)
Median 9x9	7.2 (10.9)	8.4 (7.8)	32.0 (20.0)	92.4 (41.9)	119.2 (55.7)

Figure A.72: Active contour segmentation (lesions) - Validation metrics (average and standard deviation) for parameters choice using Average Distance (AD), SmoothFactor = 0.01, ContractionBias = -0.5

	Iterations				
	50	100	200	500	1000
Original	0.52 (0.24)	0.55 (0.21)	0.33 (0.24)	0.12(0.12)	0.11 (0.11)
ADLG 50 iter	0.52 (0.24)	0.55 (0.21)	0.34 (0.24)	0.12(0.12)	0.11 (0.10)
ADLG 100 iter	0.52 (0.24)	0.55 (0.21)	0.34 (0.24)	0.12(0.12)	0.11 (0.10)
ADLG 200 iter	0.52 (0.24)	0.55 (0.21)	0.34 (0.24)	0.12(0.12)	0.11 (0.10)
ADLG 500 iter	0.52 (0.24)	0.55 (0.21)	0.34 (0.24)	0.12(0.12)	0.11 (0.10)
ADLG 1000 iter	0.52 (0.24)	0.55 (0.21)	0.34 (0.24)	0.13(0.12)	0.11 (0.11)
Median 9x9	0.52 (0.24)	0.55 (0.21)	0.34 (0.24)	0.12(0.12)	0.11 (0.10)

Figure A.73: Active contour segmentation (lesions) - Validation metrics (average and standard deviation) for parameters choice using Sørensen–Dice coefficient (SD), SmoothFactor = 0.04, ContractionBias = -0.5

	Iterations				
	50	100	200	500	1000
Original	7.2 (10.9)	8.5 (7.8)	32.7 (20.1)	95.5 (40.8)	121.5 (52.8)
ADLG 50 iter	7.2 (10.9)	8.3 (7.7)	31.6 (19.5)	91.7 (42.0)	119.8 (54.7)
ADLG 100 iter	7.2 (10.9)	8.3 (7.6)	31.6 (19.5)	91.1 (41.6)	119.3 (54.5)
ADLG 200 iter	7.2 (10.9)	8.2 (7.6)	31.3 (19.3)	90.0 (41.0)	118.3 (54.1)
ADLG 500 iter	7.3 (11.0)	8.3 (7.6)	31.1 (19.2)	90.9 (42.0)	118.3 (56.0)
ADLG 1000 iter	7.3 (10.9)	8.3 (7.5)	31.1 (19.3)	90.0 (41.7)	117.4 (55.1)
Median 9x9	7.2 (10.9)	8.3 (7.7)	31.5 (19.4)	90.8 (42.7)	118.5 (56.4)

Figure A.74: Active contour segmentation (lesions) - Validation metrics (average and standard deviation) for parameters choice using Average Distance (AD), SmoothFactor = 0.04, ContractionBias = -0.5

	Iterations				
	50	100	200	500	1000
Original	0.52 (0.24)	0.55 (0.21)	0.34 (0.24)	0.12(0.12)	0.11 (0.11)
ADLG 50 iter	0.52 (0.24)	0.55 (0.21)	0.34 (0.24)	0.13(0.12)	0.11 (0.10)
ADLG 100 iter	0.52 (0.24)	0.55 (0.21)	0.34 (0.24)	0.13(0.12)	0.11 (0.10)
ADLG 200 iter	0.52 (0.24)	0.55 (0.21)	0.35 (0.24)	0.13(0.12)	0.11 (0.10)
ADLG 500 iter	0.52 (0.24)	0.56 (0.21)	0.35 (0.24)	0.13(0.12)	0.11 (0.10)
ADLG 1000 iter	0.52 (0.24)	0.56 (0.21)	0.35 (0.24)	0.13(0.12)	0.11 (0.11)
Median 9x9	0.52 (0.24)	0.56 (0.21)	0.35 (0.24)	0.13(0.12)	0.11 (0.10)

Figure A.75: Active contour segmentation (lesions) - Validation metrics (average and standard deviation) for parameters choice using Sørensen–Dice coefficient (SD), SmoothFactor = 0.1, ContractionBias = -0.5

	Iterations				
	50	100	200	500	1000
Original	7.2 (10.9)	8.2 (7.6)	31.8 (19.3)	92.4 (41.8)	119.7 (53.2)
ADLG 50 iter	7.2 (10.9)	8.1 (7.6)	30.2 (18.2)	89.3 (41.4)	119.6 (54.2)
ADLG 100 iter	7.3 (11.0)	8.1 (7.5)	30.1 (18.2)	89.3 (41.2)	119.2 (54.2)
ADLG 200 iter	7.3 (10.9)	8.1 (7.5)	30.0 (18.3)	89.8 (41.9)	118.6 (54.6)
ADLG 500 iter	7.3 (11.0)	8.0 (7.4)	29.5 (18.3)	87.2 (41.2)	117.0 (54.8)
ADLG 1000 iter	7.2 (11.0)	8.0 (7.3)	29.3 (18.5)	86.0 (40.8)	115.9 (54.9)
Median 9x9	7.2 (11.0)	7.9 (7.5)	29.8 (18.3)	86.7 (41.0)	117.7 (56.8)

Figure A.76: Active contour segmentation (lesions) - Validation metrics (average and standard deviation) for parameters choice using Average Distance (AD), SmoothFactor = 0.1, Contraction-Bias = -0.5

	Iterations				
	50	100	200	500	1000
Original	0.52 (0.23)	0.56 (0.20)	0.35 (0.23)	0.13(0.12)	0.11 (0.10)
ADLG 50 iter	0.52 (0.23)	0.57 (0.20)	0.36 (0.23)	0.13(0.12)	0.11 (0.10)
ADLG 100 iter	0.52 (0.23)	0.57 (0.20)	0.36 (0.23)	0.13(0.12)	0.11 (0.10)
ADLG 200 iter	0.52 (0.24)	0.57 (0.20)	0.36 (0.23)	0.13(0.12)	0.11 (0.10)
ADLG 500 iter	0.52 (0.24)	0.56 (0.20)	0.36 (0.23)	0.13(0.12)	0.11 (0.10)
ADLG 1000 iter	0.52 (0.24)	0.57 (0.20)	0.36 (0.24)	0.13(0.12)	0.11 (0.10)
Median 9x9	0.52 (0.23)	0.57 (0.20)	0.36 (0.23)	0.13(0.12)	0.11 (0.10)

Figure A.77: Active contour segmentation (lesions) - Validation metrics (average and standard deviation) for parameters choice using Sørensen–Dice coefficient (SD), SmoothFactor = 0.2, Con-tractionBias = -0.5

	Iterations				
	50	100	200	500	1000
Original	7.2 (11.1)	7.3 (6.6)	27.6 (15.7)	85.0 (40.7)	117.2 (54.1)
ADLG 50 iter	7.2 (11.0)	7.1 (6.4)	26.3 (15.7)	82.4 (39.1)	115.9 (52.5)
ADLG 100 iter	7.3 (11.1)	7.4 (6.9)	26.5 (16.3)	82.9 (40.4)	116.0 (53.4)
ADLG 200 iter	7.3 (11.1)	7.5 (6.9)	26.4 (16.3)	82.6 (40.1)	115.3 (53.5)
ADLG 500 iter	7.3 (11.1)	7.5 (7.0)	26.1 (16.4)	80.4 (38.7)	113.9 (53.8)
ADLG 1000 iter	7.3 (11.1)	7.4 (6.8)	26.5 (16.8)	80.2 (37.7)	114.1 (54.6)
Median 9x9	7.1 (11.1)	6.9 (6.1)	25.8 (15.2)	79.4 (37.6)	113.6 (54.5)

Figure A.78: Active contour segmentation (lesions) - Validation metrics (average and standard deviation) for parameters choice using Average Distance (AD), SmoothFactor = 0.2, Contraction-Bias = -0.5

	Iterations				
	50	100	200	500	1000
Original	0.51 (0.24)	0.64 (0.17)	0.49 (0.23)	0.21(0.20)	0.14 (0.18)
ADLG 50 iter	0.52 (0.24)	0.64 (0.17)	0.50 (0.24)	0.23(0.21)	0.15 (0.18)
ADLG 100 iter	0.52 (0.24)	0.64 (0.17)	0.50 (0.24)	0.22(0.19)	0.13 (0.15)
ADLG 200 iter	0.52 (0.24)	0.64 (0.17)	0.50 (0.23)	0.21(0.18)	0.13 (0.15)
ADLG 500 iter	0.53 (0.24)	0.64 (0.17)	0.49 (0.23)	0.20(0.16)	0.12 (0.12)
ADLG 1000 iter	0.53 (0.24)	0.62 (0.17)	0.47 (0.22)	0.20(0.16)	0.13 (0.13)
Median 9x9	0.52 (0.24)	0.65 (0.17)	0.52 (0.23)	0.24(0.20)	0.16 (0.18)

Figure A.79: Active contour segmentation (lesions) - Validation metrics (average and standard deviation) for parameters choice using Sørensen–Dice coefficient (SD), SmoothFactor = 0.5, ContractionBias = -0.5

	Iterations				
	50	100	200	500	1000
Original	7.8 (11.8)	4.4 (4.3)	14.1 (10.0)	53.2 (27.1)	97.3 (48.8)
ADLG 50 iter	7.4 (11.6)	4.6 (4.3)	15.0 (11.3)	53.1 (30.4)	92.5 (51.0)
ADLG 100 iter	7.4 (11.7)	4.7 (4.4)	15.1 (11.3)	53.8 (30.5)	94.6 (49.0)
ADLG 200 iter	7.3 (11.6)	4.7 (4.4)	15.1 (11.1)	55.3 (29.5)	95.5 (50.3)
ADLG 500 iter	7.2 (11.7)	4.8 (4.4)	15.8 (11.1)	57.3 (28.4)	95.8 (49.0)
ADLG 1000 iter	7.1 (11.8)	5.1 (4.4)	16.6 (11.5)	57.4 (27.3)	94.2 (47.2)
Median 9x9	7.4 (11.6)	4.4 (4.1)	14.2 (10.7)	49.2 (27.3)	86.2 (51.7)

Figure A.80: Active contour segmentation (lesions) - Validation metrics (average and standard deviation) for parameters choice using Average Distance (AD), SmoothFactor = 0.5, Contraction-Bias = -0.5

A.3 Mean shift clustering (anatomical structures)

	Bandwidth		
	0.02	0.05	0.1
Original	0.50 (0.18)	0.48 (0.25)	0.15 (0.27)
ADLG 50 iter	0.56 (0.19)	0.57 (0.17)	0.42 (0.00)
ADLG 100 iter	0.53 (0.20)	0.50 (0.25)	0.51 (0.00)
ADLG 200 iter	0.48 (0.19)	0.49 (0.25)	0.51 (0.15)
ADLG 500 iter	0.47 (0.25)	0.53 (0.26)	0.62 (0.14)
ADLG 1000 iter	0.50 (0.26)	0.51 (0.26)	0.53 (0.26)
Median 9x9	0.55 (0.16)	0.55 (0.21)	0.47 (0.10)

Figure A.81: Mean shift segmentation (anatomical structures) - Validation metrics (average and standard deviation) for parameters choice using Sørensen–Dice coefficient (SD) for X,Y position weight = 0.0625

	Bandwidth		
	0.02	0.05	0.1
Original	20.9 (22.0)	30.2 (33.7)	109.8 (50.3)
ADLG 50 iter	17.8 (20.3)	20.7 (17.0)	38.4 (0.0)
ADLG 100 iter	13.7 (16.4)	28.7 (29.2)	33.8 (0.0)
ADLG 200 iter	24.2 (27.0)	27.8 (29.5)	22.6 (14.3)
ADLG 500 iter	24.7 (21.6)	19.5 (21.0)	16.2 (12.7)
ADLG 1000 iter	23.8 (23.8)	22.4 (23.8)	28.9 (31.6)
Median 9x9	17.2 (20.0)	20.2 (17.9)	23.4 (8.9)

Figure A.82: Mean shift segmentation (anatomical structures) - Validation metrics (average and standard deviation) for parameters choice using Average Distance (AD) for X,Y position weight = 0.0625

	Bandwidth		
	0.02	0.05	0.1
Original	0.52 (0.14)	0.44 (0.21)	0.21 (0.27)
ADLG 50 iter	0.55 (0.15)	0.47 (0.23)	0.48 (0.11)
ADLG 100 iter	0.50 (0.18)	0.53 (0.23)	0.38 (0.03)
ADLG 200 iter	0.61 (0.16)	0.53 (0.22)	0.42 (0.07)
ADLG 500 iter	0.55 (0.21)	0.58 (0.18)	0.64 (0.16)
ADLG 1000 iter	0.52 (0.23)	0.54 (0.24)	0.53 (0.25)
Median 9x9	0.54 (0.15)	0.52 (0.24)	0.42 (0.10)

Figure A.83: Mean shift segmentation (anatomical structures) - Validation metrics (average and standard deviation) for parameters choice using Sørensen–Dice coefficient (SD) for X,Y position weight = 0.125

	Bandwidth		
	0.02	0.05	0.1
Original	17.9 (15.4)	29.3 (28.5)	91.4 (54.0)
ADLG 50 iter	17.6 (16.1)	26.8 (29.4)	31.9 (2.5)
ADLG 100 iter	24.6 (22.2)	25.2 (26.8)	40.3 (9.8)
ADLG 200 iter	12.3 (14.7)	19.6 (19.0)	26.9 (16.2)
ADLG 500 iter	14.0 (13.1)	15.3 (16.9)	12.9 (13.4)
ADLG 1000 iter	17.5 (22.6)	16.7 (20.4)	26.2 (31.5)
Median 9x9	15.9 (13.2)	26.0 (30.2)	38.8 (7.4)

Figure A.84: Mean shift segmentation (anatomical structures) - Validation metrics (average and standard deviation) for parameters choice using Average Distance (AD) for X,Y position weight = 0.125

	Bandwidth		
	0.02	0.05	0.1
Original	0.54 (0.19)	0.37 (0.20)	0.37 (0.29)
ADLG 50 iter	0.59 (0.14)	0.45 (0.22)	0.44 (0.22)
ADLG 100 iter	0.57 (0.20)	0.50 (0.19)	0.40 (0.21)
ADLG 200 iter	0.56 (0.18)	0.52 (0.21)	0.47 (0.21)
ADLG 500 iter	0.51 (0.25)	0.62 (0.21)	0.45 (0.26)
ADLG 1000 iter	0.50 (0.25)	0.47 (0.24)	0.53 (0.24)
Median 9x9	0.62 (0.18)	0.53 (0.18)	0.43 (0.22)

Figure A.85: Mean shift segmentation (anatomical structures) - Validation metrics (average and standard deviation) for parameters choice using Sørensen–Dice coefficient (SD) for X,Y position weight = 0.25

	Bandwidth		
	0.02	0.05	0.1
Original	19.8 (19.2)	27.0 (22.4)	44.3 (48.8)
ADLG 50 iter	12.9 (10.9)	20.2 (18.8)	28.9 (29.3)
ADLG 100 iter	13.9 (15.3)	18.8 (17.1)	32.0 (29.7)
ADLG 200 iter	16.2 (14.5)	22.0 (20.4)	26.0 (21.8)
ADLG 500 iter	17.4 (19.2)	14.4 (20.9)	33.3 (36.8)
ADLG 1000 iter	19.8 (19.1)	25.5 (19.7)	18.9 (28.9)
Median 9x9	10.8 (12.5)	18.6 (23.0)	32.5 (34.6)

Figure A.86: Mean shift segmentation (anatomical structures) - Validation metrics (average and standard deviation) for parameters choice using Average Distance (AD) for X,Y position weight = 0.25

	Bandwidth		
	0.02	0.05	0.1
Original	0.50 (0.17)	0.51 (0.20)	0.41 (0.29)
ADLG 50 iter	0.53 (0.17)	0.56 (0.19)	0.46 (0.26)
ADLG 100 iter	0.53 (0.21)	0.58 (0.15)	0.46 (0.20)
ADLG 200 iter	0.60 (0.18)	0.59 (0.18)	0.53 (0.23)
ADLG 500 iter	0.60 (0.20)	0.57 (0.17)	0.52 (0.24)
ADLG 1000 iter	0.31 (0.23)	0.50 (0.25)	0.46 (0.22)
Median 9x9	0.58 (0.19)	0.56 (0.21)	0.51 (0.21)

Figure A.87: Mean shift segmentation (anatomical structures) - Validation metrics (average and standard deviation) for parameters choice using Sørensen–Dice coefficient (SD) for X,Y position weight = 1

	Bandwidth		
	0.02	0.05	0.1
Original	18.0 (18.3)	17.8 (17.3)	36.2 (34.2)
ADLG 50 iter	16.7 (16.1)	15.6 (15.9)	26.8 (26.1)
ADLG 100 iter	18.7 (16.2)	14.8 (13.3)	23.2 (19.8)
ADLG 200 iter	14.6 (17.5)	11.3 (11.0)	20.5 (26.3)
ADLG 500 iter	10.8 (11.4)	13.0 (10.9)	22.5 (27.3)
ADLG 1000 iter	30.0 (22.4)	21.1 (21.5)	25.5 (25.1)
Median 9x9	14.2 (14.5)	17.5 (19.0)	19.1 (19.2)

Figure A.88: Mean shift segmentation (anatomical structures) - Validation metrics (average and standard deviation) for parameters choice using Average Distance (AD) for X,Y position weight = 1

References

[1] S. Ahmad, M. Bolic, H. Dajani, V. Groza, I. Batkin, and S. Rajan. Measurement of heart rate variability using an oscillometric blood pressure monitor. *IEEE Transactions on Instrumentation and Measurement*, 59(10):2575–2590, oct 2010. URL: https://doi.org/10.1109/tim.2010.2057571.

[2] B. Aiazzi, L. Alparone, and S. Baronti. Multiresolution local-statistics speckle filtering based on a ratio laplacian pyramid. *IEEE Transactions on Geoscience and Remote Sensing*, 36(5):1466–1476, 1998. URL: https://doi.org/10.1109/36.718850.

[3] The American Cancer Society. Breast Ultrasound | Ultrasound for Breast Cancer, 2017. URL: https://www.cancer.org/cancer/breast-cancer/screening-tests-and-early-detection/breast-ultrasound.html.

[4] G. Andria, F. Attivissimo, G. Cavone, N. Giaquinto, and A.M.L. Lanzolla. Linear filtering of 2-d wavelet coefficients for denoising ultrasound medical images. *Measurement*, 45(7):1792–1800, aug 2012. URL: https://doi.org/10.1016/j.measurement.2012.04.005.

[5] D. Arthur and S. Vassilvitskii. k-means++: The advantages of careful seeding. In *Proceedings of the eighteenth annual ACM-SIAM symposium on Discrete algorithms*, pages 1027–1035. Society for Industrial and Applied Mathematics, 2007.

[6] S. Balocco, C. Gatta, O. Pujol, J. Mauri, and P. Radeva. SRBF: Speckle reducing bilateral filtering. *Ultrasound in Medicine & Biology*, 36(8):1353–1363, aug 2010. URL: https://doi.org/10.1016/j.ultrasmedbio.2010.05.007.

[7] J. Bezdek. *Pattern Recognition with Fuzzy Objective Function Algorithms*. Springer US, 1981. URL: https://doi.org/10.1007/978-1-4757-0450-1, doi:10.1007/978-1-4757-0450-1.

[8] D. Boukerroui, A. Baskurt, J. A. Noble, and O. Basset. Segmentation of ultrasound images—multiresolution 2d and 3d algorithm based on global and local statistics. *Pattern Recognition Letters*, 24(4-5):779–790, feb 2003. URL: https://doi.org/10.1016/s0167-8655(02)00181-2.

[9] R. Braz, A. M. G. Pinheiro, J. Moutinho, M. M. Freire, and M. Pereira. Breast ultrasound images gland segmentation. In *2012 IEEE International Workshop on Machine Learning for Signal Processing*. IEEE, sep 2012. URL: https://doi.org/10.1109/mlsp.2012.6349748.

[10] Cancer.Net. Breast Cancer - Statistics, 2018. URL: https://www.cancer.net/cancer-types/breast-cancer/statistics/2015.

[11] F. M. Cardoso, M. M. S. Matsumoto, and S. S. Furuie. Edge-Preserving Speckle Texture Removal by Interference-Based Speckle Filtering Followed by Anisotropic Diffusion. *Ultrasound in Medicine & Biology*, 38(8):1414 – 1428, 2012. URL: https://doi.org/10.1016/j.ultrasmedbio.2012.03.014.

[12] J. S. Cardoso, I. Domingues, I. Amaral, I. Moreira, P. Passarinho, J. Santa Comba, R. Correia, and M. J. Cardoso. Pectoral muscle detection in mammograms based on polar coordinates and the shortest path. In *2010 Annual International Conference of the IEEE Engineering in Medicine and Biology*. IEEE, August 2010. URL: https://doi.org/10.1109/iembs.2010.5626634.

[13] J. S. Cardoso, I. Domingues, and H. P. Oliveira. Closed shortest path in the original coordinates with an application to breast cancer. *International Journal of Pattern Recognition and Artificial Intelligence*, 29(01):1555002, January 2015. URL: https://doi.org/10.1142/s0218001415550022.

[14] J. Z. Cheng, Y. H. Chou, C. S. Huang, Y. C. Chang, C. M. Tiu, F. C. Yeh, K. W. Chen, C. H. Tsou, and C. M. Chen. ACCOMP: Augmented cell competition algorithm for breast lesion demarcation in sonography. *Medical Physics*, 37(12):6240–6252, nov 2010. URL: https://doi.org/10.1118/1.3512799.

[15] K. S. Cheng, J. S. Lin, and C. W. Mao. The application of competitive hopfield neural network to medical image segmentation. *IEEE Transactions on Medical Imaging*, 15(4):560–567, 1996. URL: https://doi.org/10.1109/42.511759.

[16] P. Coupe, P. Hellier, C. Kervrann, and C. Barillot. Bayesian non local means-based speckle filtering. In *2008 5th IEEE International Symposium on Biomedical Imaging: From Nano to Macro*. IEEE, may 2008. URL: https://doi.org/10.1109/isbi.2008.4541240.

[17] X. Deng and Y. Ma. PCNN automatic parameters determination in image segmentation based on the analysis of neuron firing time. In *Advances in Intelligent and Soft Computing*, pages 85–91. Springer Berlin Heidelberg, 2011. URL: https://doi.org/10.1007/978-3-642-25664-6_11.

[18] N. J. Dhinagar and M. Celenk. Ultrasound medical image enhancement and segmentation using adaptive homomorphic filtering and histogram thresholding. In *2012 IEEE-EMBS Conference on Biomedical Engineering and Sciences*. IEEE, dec 2012. URL: https://doi.org/10.1109/iecbes.2012.6498021.

[19] L. R. Dice. Measures of the amount of ecologic association between species. *Ecology*, 26(3):297–302, July 1945. URL: https://doi.org/10.2307/1932409.

[20] R. O. Duda and P. E. Hart. Use of the hough transformation to detect lines and curves in pictures. *Communications of the ACM*, 15(1):11–15, January 1972. URL: https://doi.org/10.1145/361237.361242.

[21] J. C. Dunn. A fuzzy relative of the ISODATA process and its use in detecting compact well-separated clusters. *Journal of Cybernetics*, 3(3):32–57, jan 1973. URL: https://doi.org/10.1080/01969727308546046.

[22] M. Elter, C. Held, and T. Wittenberg. Contour tracing for segmentation of mammographic masses. *Physics in Medicine and Biology*, 55(18):5299–5315, August 2010. URL: https://doi.org/10.1088/0031-9155/55/18/004.

[23] W. G. Flores, W. C. A. Pereira, and A. F. C. Infantosi. Breast ultrasound despeckling using anisotropic diffusion guided by texture descriptors. *Ultrasound in Medicine & Biology*, 40(11):2609–2621, nov 2014. URL: https://doi.org/10.1016/j.ultrasmedbio.2014.06.005.

[24] K. Fukunaga and L. Hostetler. The estimation of the gradient of a density function, with applications in pattern recognition. *IEEE Transactions on Information Theory*, 21(1):32–40, January 1975. URL: https://doi.org/10.1109/tit.1975.1055330.

[25] W. Gómez, L. Leija, A. V. Alvarenga, A. F. C. Infantosi, and W. C. A. Pereira. Computerized lesion segmentation of breast ultrasound based on marker-controlled watershed transformation. *Medical Physics*, 37(1):82–95, dec 2009. URL: https://doi.org/10.1118/1.3265959.

[26] H. Gray. The muscles connecting the upper extremity to the anterior and lateral thoracic walls. URL: https://www.bartleby.com/107/122.html.

[27] H. Gray. *Anatomy of the human body*. Bounty, London, England, 2012.

[28] Y. Guo, H. D. Cheng, and Y. Zhang. Breast ultrasound image segmentation based on particle swarm optimization and the characteristics of breast tissue. *New Mathematics and Natural Computation*, 07(01):135–154, March 2011. URL: https://doi.org/10.1142/s1793005711001846.

[29] Y. Guo and A. Sengur. NCM: Neutrosophic c-means clustering algorithm. *Pattern Recognition*, 48(8):2710–2724, aug 2015. URL: https://doi.org/10.1016/j.patcog.2015.02.018.

[30] Y. Guo, Y. Wang, and T. Hou. Speckle filtering of ultrasonic images using a modified non local-based algorithm. *Biomedical Signal Processing and Control*, 6(2):129–138, apr 2011. URL: https://doi.org/10.1016/j.bspc.2010.10.004.

[31] J. E. Hall. *Guyton and Hall textbook of medical physiology*. Elsevier, Philadelphia, PA, 13th edition edition, 2016.

[32] M. Hassan, A. Chaudhry, A. Khan, M. A. Iftikhar, and J. Y. Kim. Medical image segmentation employing information gain and fuzzy c-means algorithm. In *2013 International Conference on Open Source Systems and Technologies*. IEEE, dec 2013. URL: https://doi.org/10.1109/icosst.2013.6720602.

[33] A. E. Hassanien and T. H. Kim. Breast cancer MRI diagnosis approach using support vector machine and pulse coupled neural networks. *Journal of Applied Logic*, 10(4):277–284, dec 2012. URL: https://doi.org/10.1016/j.jal.2012.07.003.

[34] K. Horsch, M. L. Alparone, L. A. Venta, and C. J. Vyborny. Automatic segmentation of breast lesions on ultrasound. *Medical Physics*, 28(8):1652–1659, aug 2001. URL: https://doi.org/10.1118/1.1386426.

[35] T. Huang, G. Yang, and G. Tang. A fast two-dimensional median filtering algorithm. *IEEE Transactions on Acoustics, Speech, and Signal Processing*, 27(1):13–18, feb 1979. URL: https://doi.org/10.1109/tassp.1979.1163188.

[36] Y. L. Huang. Computer-aided diagnosis using neural networks and support vector machines for breast ultrasonography. *Journal of Medical Ultrasound*, 17(1):17–24, 2009. URL: https://doi.org/10.1016/s0929-6441(09)60011-4.

[37] Y. L. Huang and D. R. Chen. Watershed segmentation for breast tumor in 2-d sonography. *Ultrasound in Medicine & Biology*, 30(5):625–632, may 2004. URL: https://doi.org/10.1016/j.ultrasmedbio.2003.12.001.

[38] Y. L. Huang, Y. R. Jiang, D. R. Chen, and W. Kyung. Level set contouring for breast tumor in sonography. *Journal of Digital Imaging*, 20(3):238–247, jan 2007. URL: https://doi.org/10.1007/s10278-006-1041-6.

[39] D. P. Huttenlocher, W. J. Rucklidge, and G. A. Klanderman. Comparing images using the hausdorff distance under translation. In *Proceedings 1992 IEEE Computer Society Conference on Computer Vision and Pattern Recognition*, pages 654–656, June 1992. URL: https://doi.org/10.1109/CVPR.1992.223209.

[40] J. L. Jameson, D. L. Kasper, A. S. Fauci, S. L. Hauser, D. L. Longo, J. Loscalzo, and T. R. Harrison. *Harrison's principles of internal medicine.* McGraw-Hill Education / Medical, 2018. OCLC: 990065894. URL: http://accessmedicine.mhmedical.com/book.aspx?bookid=2129.

[41] A. K. Jumaat, W. E. Z. W. A. Rahman, A. Ibrahim, and R. Mahmud. Segmentation of masses from breast ultrasound images using parametric active contour algorithm. *Procedia - Social and Behavioral Sciences*, 8:640–647, 2010. URL: https://doi.org/10.1016/j.sbspro.2010.12.089.

[42] M. Kass, A. Witkin, and D. Terzopoulos. Snakes: Active contour models. *International Journal of Computer Vision*, 1(4):321–331, jan 1988. URL: https://doi.org/10.1007/bf00133570.

[43] S. Z. Li. Markov random field models in computer vision. In *Computer Vision — ECCV '94*, pages 361–370. Springer-Verlag, 1994. URL: https://doi.org/10.1007/bfb0028368.

[44] J. S. Lim. *Two-dimensional Signal and Image Processing*. Prentice-Hall, Inc., Upper Saddle River, NJ, USA, 1990.

[45] A. Madabhushi and D. N. Metaxas. Combining low-, high-level and empirical domain knowledge for automated segmentation of ultrasonic breast lesions. *IEEE Transactions on Medical Imaging*, 22(2):155–169, feb 2003. URL: https://doi.org/10.1109/tmi.2002.808364.

[46] H. Madjar and J. Jellins. *The practice of breast ultrasound : techniques, findings, differential diagnosis ; 73 tables*. Thieme, Stuttgart, 2000.

[47] K. D. Marcomini and H. Schiabel. Nodules segmentation in breast ultrasound using the artificial neural network self-organizing map. In *Proceedings of the World Congress on engineering*, volume 2, pages 4–7, 2012.

[48] F. Meyer. Topographic distance and watershed lines. *Signal Processing*, 38(1):113–125, July 1994. URL: https://doi.org/10.1016/0165-1684(94)90060-4.

[49] H. P. Oliveira, J. S. Cardoso, A. T. Magalhães, and M. J. Cardoso. A 3d low-cost solution for the aesthetic evaluation of breast cancer conservative treatment. *Computer Methods in Biomechanics and Biomedical Engineering: Imaging & Visualization*, 2(2):90–106, December 2013. URL: https://doi.org/10.1080/21681163.2013.858403.

[50] N. Otsu. A threshold selection method from gray-level histograms. *IEEE Transactions on Systems, Man, and Cybernetics*, 9(1):62–66, jan 1979. URL: https://doi.org/10.1109/tsmc.1979.4310076.

[51] P. Perona and J. Malik. Scale-space and edge detection using anisotropic diffusion. *IEEE Transactions on Pattern Analysis and Machine Intelligence*, 12(7):629–639, July 1990. URL: https://doi.org/10.1109/34.56205.

[52] S. Poonguzhali and G. Ravindran. A complete automatic region growing method for segmentation of masses on ultrasound images. In *2006 International Conference on Biomedical and Pharmaceutical Engineering*, pages 88–92, Dec 2006.

[53] A. Rodtook and S. S. Makhanov. Multi-feature gradient vector flow snakes for adaptive segmentation of the ultrasound images of breast cancer. *Journal of Visual Communication and Image Representation*, 24(8):1414–1430, 2013.

[54] A. Sarti, C. Corsi, E. Mazzini, and C. Lamberti. Maximum likelihood segmentation of ultrasound images with rayleigh distribution. *IEEE Transactions on Ultrasonics, Ferroelectrics, and Frequency Control*, 52(6):947–960, June 2005. URL: https://doi.org/10.1109/TUFFC.2005.1504017.

[55] J. Shan, H. D. Cheng, and Y. Wang. A novel automatic seed point selection algorithm for breast ultrasound images. In *2008 19th International Conference on Pattern Recognition*, pages 1–4, Dec 2008. URL: https://doi.org/10.1109/icpr.2008.4761336.

[56] J. Shan, H. D. Cheng, and Y. Wang. A completely automatic segmentation method for breast ultrasound images using region growing. In *11th Joint International Conference on Information Sciences*. Atlantis Press, 2008/12. URL: https://doi.org/10.2991/jcis.2008.57.

[57] J. Shan, H. D. Cheng, and Y. Wang. Completely automated segmentation approach for breast ultrasound images using multiple-domain features. *Ultrasound in Medicine & Biology*, 38(2):262–275, feb 2012. URL: https://doi.org/10.1016/j.ultrasmedbio.2011.10.022.

[58] J. Shan, H. D. Cheng, and Y. Wang. A novel segmentation method for breast ultrasound images based on neutrosophic l-means clustering. *Medical Physics*, 39(9):5669–5682, aug 2012. URL: https://doi.org/10.1118/1.4747271.

[59] K. Singh, S. K. Ranade, and C. Singh. A hybrid algorithm for speckle noise reduction of ultrasound images. *Computer Methods and Programs in Biomedicine*, 148:55–69, sep 2017. URL: https://doi.org/10.1016/j.cmpb.2017.06.009.

[60] T. J. Sørensen. A method of establishing groups of equal amplitude in plant sociology based on similarity of species content and its application to analyses of the vegetation on danish commons. *Biol. Skar.*, 5:1–34, 1948.

[61] E. A. Stephen. Hard and soft clustering explained, November 2016. URL: http://arnoldit.com/wordpress/2016/11/17/hard-and-soft-clustering-explained/.

[62] P. Suetens. *Fundamentals of medical imaging*. Cambridge University Press, 2017.

[63] R. Suganya, S. Rajaram, and A. S. Abdullah. *Big Data in Medical Image Processing*. CRC Press, 2018.

[64] C. Tomasi and R. Manduchi. Bilateral filtering for gray and color images. In *Sixth International Conference on Computer Vision (IEEE Cat. No.98CH36271)*, pages 839–846, Jan 1998. URL: https://doi.org/10.1109/ICCV.1998.710815.

[65] R. T. Whitaker. A level-set approach to 3d reconstruction from range data. *International journal of computer vision*, 29(3):203–231, 1998.

[66] Wikipedia contributors. Euclidean distance — Wikipedia, the free encyclopedia, 2019. [Online; accessed 14-July-2019]. URL: https://en.wikipedia.org/w/index.php?title=Euclidean_distance&oldid=902224259.

[67] Wikipedia contributors. Hausdorff distance — Wikipedia, the free encyclopedia, 2019. [Online; accessed 14-July-2019]. URL: https://en.wikipedia.org/w/index.php?title=Hausdorff_distance&oldid=877749743.

[68] WHO World Health Organization. WHO — Breast Cancer, september 2018. https://www.who.int/cancer/prevention/diagnosis-screening/breast-cancer/en/.

[69] M. Xian, J. Huang, Y. Zhang, and X. Tang. Multiple-domain knowledge based mrf model for tumor segmentation in breast ultrasound images. In *2012 19th IEEE International Conference on Image Processing*, pages 2021–2024, Sep. 2012. URL: https://doi.org/10.1109/ICIP.2012.6467286.

[70] M. Xian, Y. Zhang, and H. D. Cheng. Fully automatic segmentation of breast ultrasound images based on breast characteristics in space and frequency domains. *Pattern Recognition*, 48(2):485–497, feb 2015. URL: https://doi.org/10.1016/j.patcog.2014.07.026.

[71] C. Xu and J. L. Prince. Snakes, shapes, and gradient vector flow. *IEEE Transactions on Image Processing*, 7(3):359–369, March 1998. URL: https://doi.org/10.1109/83.661186.

[72] J. Zhang, G. Lin, L. Wu, and Y. Cheng. Speckle filtering of medical ultrasonic images using wavelet and guided filter. *Ultrasonics*, 65:177–193, feb 2016. URL: https://doi.org/10.1016/j.ultras.2015.10.005.

[73] Q. Zhu, G. Song, and J. Shi. Untangling cycles for contour grouping. In *2007 IEEE 11th International Conference on Computer Vision*, pages 1–8, Oct 2007. URL: https://doi.org/10.1109/ICCV.2007.4408929.